DEPARTMENT OF INORGANIC CHEMISTRY AND CHEMICAL ENGINEERING, UNIVERSITY OF CÓRDOBA, SPAIN.

"DEVELOPMENT OF NANOPARTICULATE FORMS OF TIN-BASED ALLOY MATERIALS FOR HIGH ENERGY DENSITY ANODES IN LITHIUM-ION BATTERIES"

DOCTORAL THESIS

Done at the University of Córdoba (Spain)

by

Uche Godswill Nwokeke

B. Sc (Ind. Chem.), M. Sc (Mat. for Energy Storage and Conversion)

2012

TÍTULO: Ö^ç^∣[ ] { ^} o∣ -Á æ) [ ] æ‹cæ&˘ ∣æ‹^Á∣ ¦{ •Á -Áæ ̈äæ‹^åÁæ∣[ˆÁ æ‹^¦ãæ•Á[¦Á

@t @Á}^¦*ˆÁ‹^}•ãˆÁæ)[å^•Áæ¦äc@t { ̈æ¦}Áæ‹æ‹^¦ã‹•Á

AUTOR: W&@ÁÕ[å• ̧ä∣Á ̧[\^\^

TÍTULO DE LA TESIS: Development of nanoparticulate forms of tin-based alloy materials for high energy density anodes in lithium-ion batteries

DOCTORANDO: Uche Godswill NWOKEKE

INFORME RAZONADO DE LOS DIRECTORES DE LA TESIS
(se hará mención a la evolución y desarrollo de la tesis, así como a trabajos y publicaciones derivados de la misma)

El doctorando fue alumno de los directores de esta tesis en varias asignaturas del máster europeo "Materiales para almacenamiento y conversión de la energía", estudios que concluyó exitosamente. Su trabajo fin de máster estuvo centrado en el estudio de compuestos intermetálicos basados en el estaño y, basándonos en los buenos resultados obtenidos, se obtuvo una beca del consorcio europeo Alistore-ERI en competición con otras solicitudes. Esta beca ha permitido la continuación de su trabajo de investigación y la realización de la tesis doctoral en el Departamento de Química Inorgánica e Ingeniería Química (Área de Química Inorgánica) y en el programa de doctorado Materiales y Energía. La calidad y originalidad del trabajo realizado están garantizadas por la publicación de varios artículos en revistas tales como *Chemistry of Materials*, *Journal of Power Sources* y *Journal of Alloys and Compounds*, así como por la realización de varias comunicaciones a congresos internacionales. En varias de estas publicaciones indexadas, el doctorando es el primer autor. La tesis doctoral desarrolla el estudio de compuestos intermetálicos del tipo MSn_2, donde M es Fe, Co o una mezcla de Fe y Co. Se han estudiado varios métodos para controlar el tamaño y la morfología de las partículas, incluyendo primero el método del poliol, después el método sonoquímico y, al final del trabajo, la encapsulación en una matriz orgánica. Las técnicas de caracterización de materiales usadas incluyen XRD, HRTEM, DTA, Mössbauer, SEM, EPR y EIS. Se logró dilucidar ciertos efectos de la nanoestructuración en propiedades físicas, químicas y electroquímicas. Por todo lo expuesto anteriormente, informamos favorablemente para la presentación y defensa de la tesis doctoral.

Por todo ello, se autoriza la presentación de la tesis doctoral.

Córdoba, _14_ de __Marzo__ de 2012_

Firma de los directores

Fdo.:__José Luis Tirado Coello_____   Fdo.: _Ricardo Alcántara Román____

ii

CONTENTS

        Annex I.   CV.

1.   INTRODUCTION

1.1.   World energy demand and consumption

Energy is one of the most important challenges of the 21st century [1, 2]. Consequently, energy consumption is now seen as a measure of a country´s economic growth and development. Electricity is the world´s fastest-growing form of end use energy consumption as it has been for the past several decades. Net electricity generation worldwide is expected to rise by 2.3% per year on average from 2007 to 2035 (Fig. 1.1), while total world energy demand will grow by 1.4% per year [3].

In the 20th century, the rapid advancement of science and technology became the engine for great industrial and economic growth [4]. Over the years, the world´s supply of energy has been from fossil fuels (coal, petroleum and natural gas), in addition to supplies from nuclear and hydroelectrical sources. However, the proven reserves of fossil fuels are progressively decreasing (Hubbert´s theory of peak oil), and their continued use produces harmful effects such as pollution that threatens human health and greenhouse gases associated with global warming. Currently, the world´s growing thirst for oil amounts to almost 1000 barrels a second, which means about 2 litres a day per each person living on the earth. The current global consumption is equivalent to 13 terawatts (TW), that is, a steady 12 trillion watts of power demand [1]. The magnitude of economically recoverable reserves of oil and natural gas remains a matter of discussion and debate [2]. The maximum production of oil per person occurred in 1979. More probably, an oil peak will occur between 2000 and 2020. If the rapid surge in energy consumption driven by both worldwide population growth and economic expansion continues at its present pace, mankind will surely use up all the petroleum and natural gas resources. It will then have no choice but to switch to coal, a fossil fuel with a high output of greenhouse gases [4]. In general, increasing and continued use of fossil fuels have corresponding increases in the emission of CO_2 [2].
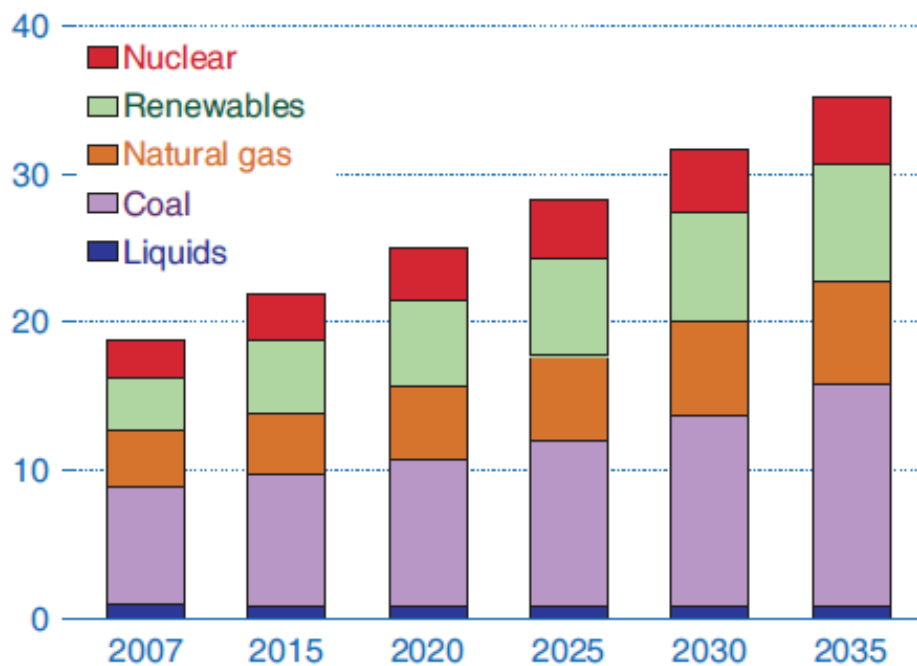
Figure 1.1. History and projections of world net electricity generation by source, 2007-2035 (trillion kilowatt-hours) [3].

Other sources of energy have their shortcomings. Nuclear energy has serious safety, health and wastes concerns; solar energy sources are limited by high cost and low conversion efficiency; wind energy sources are limited by natural variability of winds and aesthetic and ecological objections; hydrothermal sources has led to flooding and displacement with attendant social and economic problems, while storage problems limit the use of hydrogen [1].

Limitations on fossil resources and the environmental hazards that become apparent in the 21st century will force society to utilize energy resources efficiently and to adopt widespread recycling [4]. Although the use of coal (which accounted for 42% of total generation in 2007) is expected to remain largely unchanged, liquids, natural gas and nuclear power will all lose market share of world generation and will be displaced by strong growth projected for renewable sources of energy [3].

Rapid development of new technologies such as portable consumer electronics and electric vehicles has generated need for batteries that provide both higher energy density and higher power capability. Rechargeable lithium batteries have revolutionized portable electronic devices. They have become the dominant power source for cell phones, digital cameras, laptops etc., because of their superior energy density (capability to store 2-3 times the energy per unit weight and volume compared with conventional rechargeable batteries). Also, energy consumption in the transport sector is increasing globally. This in turn is aggravated by rapid urbanization and changing lifestyles in highly populated and economically emerging countries in Asia (mainly China and India) and the South American country of Brazil. There are an estimated 600 million or so cars in the world today. If vehicular energy efficiency can be improved and a shift can be made from fossil fuels to alternative energy sources, consumption of fossil fuels will be greatly reduced.

1.2. Batteries and voltage piles

The worldwide market for rechargeable lithium batteries is now valued at 10 billion dollars per annum and growing [5]. They are the technology of choice for future hybrid electric vehicles. Since electric cars are zero emission vehicles, they are seen as a solution to localized environmental pollution problems.

From the above concerns, it is therefore expected that rechargeable batteries will in all likelihood make a great contribution to overcoming the world´s environmental and energy problems. However, there are some issues that have to be resolved if we must achieve the goal of reduction of the energy derived from fossil fuels vis a vis the use of batteries:

- Reduction of the amount of energy required for manufacture and disposal.

- Shift from the use of disposable (primary) batteries to rechargeable (secondary) batteries.

- Improvement of the charging/discharging efficiency of batteries.

- Development of recycling technologies.

9

Also, large rechargeable batteries for energy storage and energy management should be developed, directly or indirectly linked to the electric power systems. This way, we will reduce the need for fossil fuels for power generation, and promote the diversification of electricity sources.

In general, the batteries we need to develop are batteries for electric vehicles that will help us to use fossil fuels more economically while coping with power burdens, batteries for hybrid electric vehicles which have both batteries and gasoline to use fossil fuels more efficiently, and batteries for decentralized energy storage systems to enable load levelling, peak cutting and to stabilize the supply of electricity from renewable energy sources such as wind power generators and solar cells [4].

A battery is defined as an electrochemical device that stores chemical energy and releases it in the form of electrical energy when needed. All batteries are composed of two electrodes connected by an ionically conductive material called an electrolyte. The two electrodes have different chemical potentials, dictated by the chemistry that occurs at each. When the electrodes are connected by means of an external device, electrons spontaneously flow from the more negative to the more positive potential. Ions are transported through the electrolyte, maintaining the charge balance and electrical energy can be tapped by the external circuit. Depending on the reversibility of the electrochemical processes involved, batteries can be classified as primary or non-rechargeable (voltage piles) and secondary or rechargeable. While the reaction in a secondary battery is reversible, that in the primary battery is irreversible [6].

1.2-1. Primary batteries

The first true battery (primary battery) was invented by Alessandro Volta in 1800 (the Voltaic Pile) which comprised of copper and zinc disc electrodes, and brine as the electrolyte, soaked in a layer of cloth which was the separator. Various systems such as the Daniel cell, Grove cell, Leclanché and zinc-carbon cell were then developed by the end of the 19th century. Practically, lithium manganese dioxide battery, alkaline battery, lithium primary battery and zinc air battery have been designed and commercialized over the years [6, 7].

1.2.1-1.   Li-primary battery

The first primary lithium battery appeared in early 1970's. The motivation for using a battery technology based on Li metal as anode relied initially on the fact the lithium is a highly reducing element (-3.04 vs. standard hydrogen electrode) as well as the lightest (equivalent weight M = 6.94 gmol^{-1}, and specific density ρ=0.53 gcm^{-3}) metal, thus facilitating the design of storage systems with high energy density. The advantage in using Li metal was first demonstrated in the 1970´s with the assembly of primary Li cells [8, 9]. The primary cell consisted of lithium as the anode, an electrolyte made of lithium salts dissolved in aprotic solvents and various forms of cathode materials including solids that are sparingly soluble in electrolytes (e.g. CuO, $(CF_x)n$, MnO_2, FeS, Ag_2WO_4, Ag_2MoO_4, $CuWO_4$ and $CuMoO_4$) and cathodes soluble in electrolytes (e.g. SO_2, $SOCl_2$ and SO_2Cl_2). Some of the reactions occurring in Li-primary batteries include:

$$2\ Li + 2SO_2 \rightarrow Li_2S_2O_4$$

$$4\ Li + SOCl_2 \rightarrow 4LiCl + SO_2 + S$$

$$2\ Li + CuO \rightarrow Li_2O + Cu$$

$$nxLi + (CF_x)n \rightarrow nC + nxLiF$$

$$2Li + Ag_2CrO_4 \rightarrow 2Ag + Li_2CrO_4$$
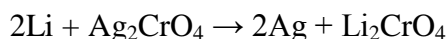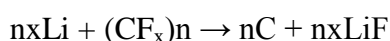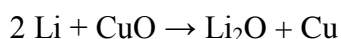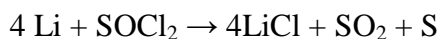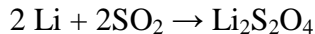
Other advantages of using Li as anode in Li-primary batteries included flat discharge, minimal self-discharge due to the passivation of lithium and wide operational temperature range. Owing to their high capacity and variable discharge rate, they rapidly found applications as power sources for watches, calculators or for implantable medical devices. As in all primary batteries, the anode, Li-metal, is the limiting electrode. Hence, the cell cannot be used as soon as the lithium is used up thereby limiting the long-term usability of the cell.

1.2-2. Rechargeable batteries

The first rechargeable (secondary) battery, the lead-acid battery was developed by the French Physicist Gaston Planté in 1859. The so-called lead-acid battery finds application in almost every vehicle for engine start-up due to its high power ability, but normalized to its weight and volume, the energy density is relatively low. Other secondary systems that followed include nickel-cadmium, nickel-iron, nickel-zinc, silver-zinc, silver-cadmium, nickel-metal-hydride, and lately, the lithium-ion battery (Table 1.1). Although the nickel-metal hydride and lithium-ion batteries are both excellent in terms of their volume energy density, the lithium-ion battery is superior in weight energy density as it provides 1.5 times much energy as the nickel metal hydride battery (Fig.1.2).
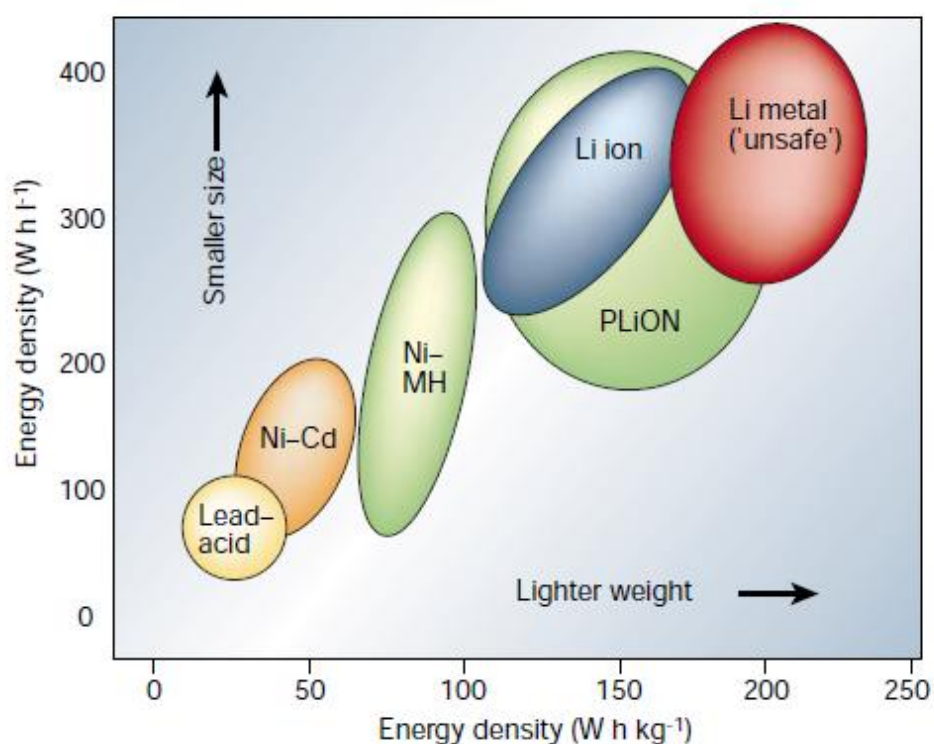
Figure 1.2. Comparison of the different battery technologies in terms of volumetric and gravimetric energy density [9].

Table 1.1. Some secondary batteries and their characteristics.

Battery System	Cathode	Anode	Electrolyte	Overall Cell Reaction	Nominal Voltage (V)
Lead Acid	PbO_2	Pb	H_2SO_4 aqueous solution	$PbO_2 + 2H_2SO_4 + Pb \leftrightarrow 2PbSO_4 + 2H_2O$	2
Ni-Cd	NiOOH	Cd	KOH aqueous solution	$2NiOOH + Cd + 2H_2O \leftrightarrow 2Ni(OH)_2 + Cd(OH)_2$	1.2
Ni-MH	NiOOH	Hydrogen-adsorbed alloy(MH)	KOH aqueous solution	$NiOOH + MH \leftrightarrow M + Ni(OH)_2$	1.2
Lithium ion	$LiCoO_2$	C	Organic solvent + salt of Li	$LiCoO_2 + C_6 \leftrightarrow Li_{1-x}CoO_2 + Li_xC_6$	3.7

1.2.2-1.   Metallic lithium rechargeable batteries

The discovery of materials which were later identified as intercalation compounds was crucial in the development of high-energy rechargeable Li-systems. Like most innovations, development of the technology resulted from several contributions. By 1972, the concept of electrochemical intercalation and its potential use were clearly defined. Attempts to develop rechargeable lithium batteries followed in the 1980's (by Exxon) but failed due to safety problems [9]. Li metal was used as the negative electrode and lithium perchlorate in dioxolane as the electrolyte. TiS_2, which

was the best intercalation compound at the time having a favourable layered-type structure, was used as the positive electrode. But in spite of the impeccable operation of the positive electrode, the system was not viable. It soon encountered the shortcomings of a Li-metal/liquid electrolyte combination-uneven (dendritic) Li growth as the metal was replated during each subsequent discharge-charge cycle which led to explosion hazards [9].

1.2.2-2.   The lithium-ion battery

Consequent upon the inherent instability of lithium metal, especially during charging, research shifted to a non-metallic lithium battery. It has been replaced by another intercalation material with an energy level close to that of metallic lithium, i.e. LiC_6 (~ 0.1 V vs. Li). Although lower in energy density than lithium metal, lithium ion battery is safe, provided certain precautions are met when charging and discharging. In 1991, the Sony Corporation commercialized the first lithium-ion battery [8-10].

When the lithium ion battery is charged, the lithium ions in the positive electrode material migrate through the solution to the negative electrode material with the flow of charging current to the external circuit. In the opposite direction, the lithium ions in the anode migrate through the separator to the cathode material with the flow of discharging current through the external circuit as shown in Figure 1.3.
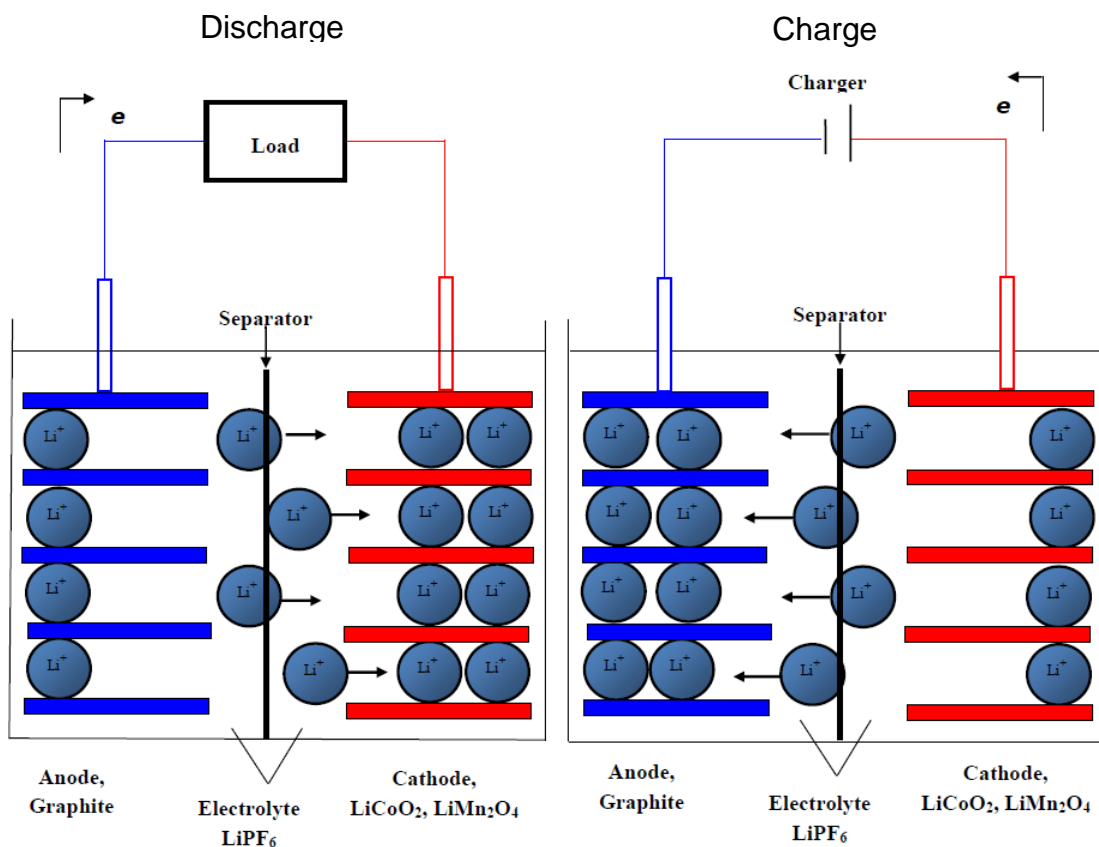
Figure 1.3. Schematic representation of lithium-ion battery during the discharge-charge process.

The reactions that take place in a typical lithium-ion battery are shown below, with $LiCoO_2$ and carbon as cathode and anode, respectively:

Cathode half reaction: $\mathbf{LiCoO_2 = Li_{1-x}CoO_2 + xLi^+ + xe^-}$

Anode half reaction: $$xLi^+ + xe^- + 6C = Li_xC_6$$

Battery as a whole: $$LiCoO_2 + 6C = Li_{1-x}CoO_2 + Li_xC_6$$

It is important to note that lithium ions themselves are not being oxidized, rather in a lithium-ion battery the lithium ions are transported to and from the cathode or anode, with the transition metal being oxidized from Co^{3+} to Co^{4+} during charging, and reduced from Co^{4+} to Co^{3+} during discharge [8]. The amount of lithium which can be intercalated reversibly determines the capacity of the battery. Based on this principle, the lithium-ion rechargeable battery is also known as the *swing battery* or *rocking chair battery* since two-way movement of lithium ions between anode and cathode through the electrolyte occurs during the charge and discharge process.

The distinguishing features of today´s commercial Li-ion batteries are: [11].

- High operating voltage: a single cell has an average operating potential of approximately 3.6 V, three times the operating voltage of both Ni-Cd and Ni-MH batteries and about twice that of sealed Pb-acid batteries.

- Compact, lightweight and high energy density: the energy density is about 1.5 times and specific energy is about twice that of high-capacity Ni-Cd batteries.

- Fast charging potential: batteries can be charged to about 80-90% of full capacity in one hour.

- High coulombic and energy efficiency.

- Wide range of operating temperature: from -20 to 60°C.

- Superior cycle life: service life of a battery exceeds 500 cycles.

- Excellent safety.

- Low self-discharge: only 8-12% per month.

- Long shelf-life: no reconditioning required up to approximately 5 years (Ni-Cd: 3 months; Ni-MH: 1 month).

- No memory-effect: can be recharged at any time.

- Non-polluting: does not use toxic heavy metals such as Pb, Cd or Hg.

Generally, in order to achieve these superior performances in lithium-ion cells, the cell components have to satisfy the following requirements: [7, 8, 12].

- Cathode and anode should support a high degree of lithium insertion/ de-insertion to maximize energy density.
- Cathode materials should have a high lithium chemical potential and anode materials should have a low lithium chemical potential in order to maximize the cell voltage and thus the energy density.
- Voltage change in the cathode and anode materials during charge-discharge process should be small.
- Minimal changes in the host network to ensure good reversibility.
- Good electronic and ionic conductivity to provide high rate capability.
- Lithium diffusion coefficient should be large for high rate charge-discharge performance.
- Electrolyte, cathode and anode materials should be inexpensive and preferably environmentally friendly.

1.3.   Positive electrode materials for lithium-ion batteries

1.3-1. LiCoO$_2$ and LiNiO$_2$

Layered LiCoO$_2$ is the earliest found lithium metal oxide used as cathode material [13]. It is widely used in most commercial lithium ion batteries due to its good cyclability, reasonable capacity and easy synthesis [14-16]. LiCoO$_2$ has a trigonal unit cell consisting of a cubic close packed oxygen lattice with Li and Co ions occupying two sets of octahedral interstitial sites respectively (space group 166, O 6c sites, Li 3a sites, Co 3b sites). The layered structure provides an ideal two-dimensional pathway for lithium diffusion in and out of the lattice during charge-discharge cycling [17-19].

The major drawback of LiCoO$_2$ is the cost and toxicity of cobalt which has long motivated the search for alternative intercalation compounds. It also has a relatively low

capacity of about 120 mAh/g [7, 17, 20]. There are several permutations of this lithium cobalt oxide such as nickel-manganese-cobalt, but the key ingredient is cobalt, which makes for the highest energy storage in the battery.

$LiNiO_2$ is another layered oxide potentially used as cathode in Li-ion batteries. It is more attractive than $LiCoO_2$ because of its lower cost and the possibility of higher discharge capacity. $LiNiO_2$ is isostructural with $LiCoO_2$. However, this compound can show structural and compositional changes depending on its preparation conditions [21-25].

1.3-2. $LiMn_2O_4$

The spinel $LiMn_2O_4$, although possessing $\approx 10\ \%$ less capacity than $LiCoO_2$, has an advantage in terms of cost and is perceived as being "green" (that is, non-toxic and from abundant material source) [9]. Consequently, there is a huge interest in this material from the research point of view. $LiMn_2O_4$ is a three-dimensional host. In the $LiMn_2O_4$ spinel-type structure (space-group: Fd3m) a cubic close-packed (ccp) array of oxygen ions occupy the 32e position, Mn ions are located in the octahedral 16d site, and Li in tetrahedral 8a site. The Mn ions have an octahedral coordination to the oxygens, and the MnO_6 octahedra share edges in a three-dimensional host for the Li guest ions [26]. Each of the 8a-tetrahedron faces is shared with an adjacent, vacant 16c site. This combination of structural features in the stoichiometric spinel compound is the most stable from of manganese oxide used in cathodes of rechargeable batteries.

$LiMn_2O_4$ was a candidate to replace $LiCoO_2$. However, a major drawback of $LiMn_2O_4$ cathodes is the increased rate of capacity fade observed both during storage and charge-discharge cycling which is severe at elevated temperatures [7, 27]. In general, the performance of $LiMn_2O_4$ in contrast to $LiCoO_2$ is very sensitive to the preparative conditions [17, 28-29].

1.3-3. Olivine-type phosphates

The olivine-related $LiFePO_4$ [9] is a viable alternative to some of the transition metal oxide cathode materials used in commercial lithium ion products for power tools

and HEVs [9, 30-33]. It has a very stable tunnel structure with the lithium diffusion pathway along the (001) direction. In general, $LiMO_4$, olivine-related phosphates show poor electrochemical performance due to their low intrinsic electronic conductivity. Lithium deinsertion/insertion into $LiFePO_4$ takes place through a two-phase reaction mechanism between $Li_{1-\delta}FePO_4$ and $Li_{\delta}FePO_4$. Recent results indicate that for nanostructured materials, the growth reaction is considerably faster than its nucleation, explained by the existence of structural constraints occurring just at the reaction interface. Anyway, by modifying the particle size and ion ordering (the presence of defects and cation vacancies) in the material, the two-phased mechanism described at room temperature can be modified resulting in a single-phase mechanism [27]. Carbon coatings and doping enhance electrochemical reaction.

1.4. Negative electrode materials for lithium-ion batteries

1.4-1. Carbon

At present, mostly carbons are used as the negative electrode of commercial rechargeable lithium ion batteries: (i) because they exhibit higher specific charges and more negative redox potentials than most metal oxides, chalcogenides and polymers; and (ii) due to their dimensional stability as they show better cycling performance than lithium alloys. Carbons that are capable of reversible lithium intercalation can roughly be classified as graphitic and non-graphitic (disordered) carbons [27].

Graphitic carbons are carbonaceous materials with a layered structure but typically with a few numbers of structural defects. From a crystallographic point of view, the term "graphite" is only applicable to carbons having a layered lattice structure with a perfect stacking order of graphene layers, either the prevalent AB (hexagonal graphite, Fig.1.4a), or the less common ABC (rhombohedral graphite) [34]. Graphite is the most thermodynamically stable form of carbon structure, commonly referred to as the standard state where carbon atoms are held together by strong covalent bonding in a hexagonal lattice structure forming expansive sheets or layers loosely coupled together by much weaker van der Waal´s bonding between layers [6]. The most common lithium ion anode material used today is carbon in its highly ordered graphite form, with a maximum theoretical capacity of 372 mAh/g by the formation of LiC_6.

Non-graphitic carbonaceous materials consist of carbon atoms that are mainly arranged in a planar hexagonal network but without far-reaching crystallographic order on the *c*-direction (Fig. 1.4b). The structure is characterized by amorphous areas embedding and crosslinking more graphitic ones. The number and the size of the areas vary, and depend on both the precursor material and the manufacturing temperature [34].

The interlayer spacing provided by the weakly bonded graphene is highly accommodating to insertion and extraction of Li cations. The graphene layers also have excellent electronic conductivity through the tightly bonded carbon planes providing low resistance electron pathways to facilitate easy electron pairing with lithium cations throughout the material. Thus, graphite is a semimetal. The structure is also mechanically stable and it provides high cyclability undergoing very small volume change of only about 10% from fully lithiated to fully de-lithiated and can provide 1000´s of cycles without appreciable loss of capacity. In 1995, Herold first synthesized Graphite Intercalation Compound (GIC) with a stage structure; since then the charge transfer phenomena of the Li-GIC compounds, which have the composition of Li_xC_6, have been extensively studied as anode materials [6, 14]. Disordered carbon can uptake more lithium than x = 1 in Li_xC_6 [22].

(a)

basal plane surface

A

B

A

prismatic surface

layer plane spacing $(\frac{C}{2} = 0.3354$ nm$)$

0.246 nm

0.142 nm

outline of unit cell
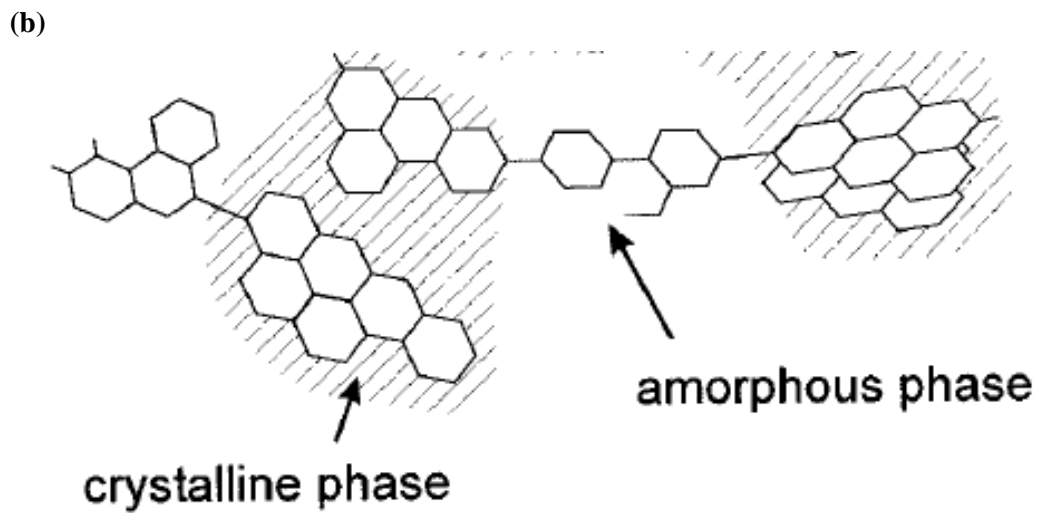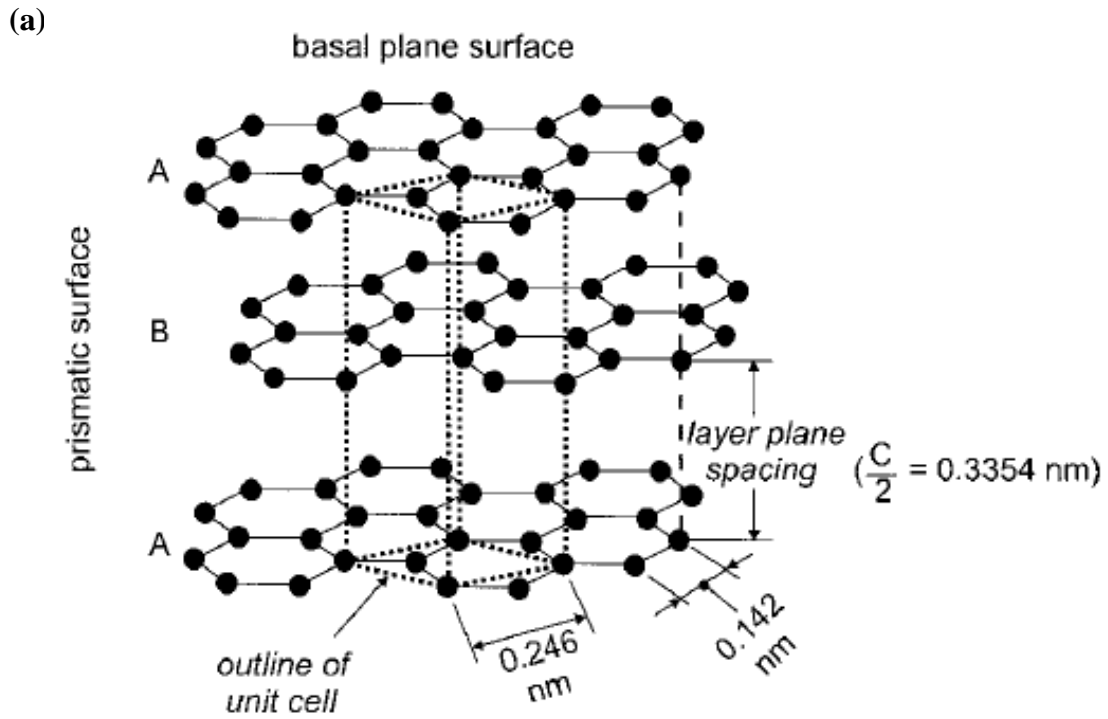
(b)

amorphous phase

crystalline phase

Figure 1.4. (a) Schematic drawing of the crystal structure of hexagonal graphite, showing the AB layer stacking sequence and the unit cell. (b) a cross section of the non graphitic (disordered) carbonaceous material [34].

21

Theoretically, Li^+ intercalation into graphite is fully reversible [34]. However, a certain fraction of lithium that reacts with carbon in the discharge of an electrochemical cell cannot be recuperated in the charge process. Some of the lithium atoms may remain trapped in the carbon microstructure. Lithium can be trapped in the internal porosity of disordered carbons. Heteroatoms such as oxygen and sulphur contained in the carbonaceous material can react irreversibly with lithium. The excess charge consumed in the first cycle is generally ascribed to the solid electrolyte interface (SEI) formation and corrosion-like reactions of Li_xC_6. The properties of the surface film are essential for the stability of the carbon electrode and mainly depend on the nature of the carbon material and the electrolyte solution. The nature of the SEI is not completely known, but it is generally accepted to be constituted by both organic and inorganic compounds that are electronically nonconducting and lithium-ion conducting. Like metallic lithium and lithium-rich lithium alloys, lithium/carbon intercalation compounds are thermodynamically unstable in all known electrolytes, and therefore the surfaces, which are exposed to the electrolyte, have to be kinetically protected by SEI films. In contrast to the spontaneous film formation on metallic lithium upon contact with electrolyte, the film formation on Li_xC_6 surfaces takes place as a charge-consuming side reaction in the first few Li^+ intercalation/deintercalation cycles, especially during the first reduction of the carbon host material. Recent studies have found that the main contribution to the SEI formed on the edge plane of graphite is the salt anion reduction, whereas the main contribution to the SEI formed on the basal plane is the solvent reduction, and on the other hand, the edge-plane SEI is thicker. The SEI protects the lithium-carbon material against the corrosion due to uncontrolled reactions with the electrolyte solution. Ideally, it should be compact and insoluble and should irreversibly adhere to the active surface. Since the positive electrode is the lithium source in a lithium-ion battery, charge, and lithium losses are detrimental to the specific energy of the whole cell and have to be minimized for an optimum cell performance [22, 34].

1.5. New negative electrode materials

Although carbon-based materials are still the dominant anodes in commercial lithium-ion batteries (due to their abundance, light weight, suitable working potential,

structural stability upon cycling, and safety compared to lithium metal), there has been great interest on the non-carbonaceous materials with high specific capacity to meet the high energy density demands in portable devices [36-38]. Graphite has a very low Li atomic density at full Li capacity in the carbon intercalation compound (LiC_6), resulting in a relatively low volumetric Li capacity. This is an important aspect in choosing the electrode materials because the total amount of Li-ions that can be taken up by the electrode material corresponds to the total time integration of the battery current. In addition, there are poor plating/stripping efficiencies in organic electrolyte solutions, formation of lithium dendrites during charge and discharge cycles and unsafe operating characteristics due to high reactivity of the lithium metal. Therefore, extensive research is being performed for the development of alternative anode materials that would give a higher energy density for Li-ion battery systems [36-40].

1.5-1. Conversion electrodes

Lithium-driven conversion reactions allow the complete reduction of transition metal oxide M_xO_y to their metallic state according to the following reaction,

$$M_xO_y + 2yLi^+ + 2ye^- = xM + yLi_2O$$
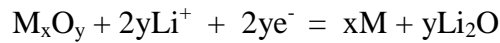
The reaction of these materials with Li^+ ions involves the formation of Li_2O [39]. The Gibbs free energy of the overall reaction can be calculated from the free energy values of the oxides:

$$\Delta G^0_r = y\Delta G^0_f (Li_2O) - \Delta G^0_f(M_xO_y) < 0 \qquad (1.1)$$

Hence, those metal oxides with less negative values of ΔG^0_f will lead to feasible conversion reactions.

The electromotive force (*emf*) values, calculated from the equation $\Delta G^0 = -nFE^0$, reveal that the cell voltage values for the first left-side elements are low enough to be considered as potential anodes in lithium ion batteries. Oxide anions migrate from the

transition metal to the alkaline metal, yielding a biphasic state consisting of nanodomains of M and Li_2O. Although there is evidence of metal oxidation upon charging, there is not much report of the whole recovery of the initial framework. The oxide anions diffusion is favoured by the large interfacial region among nanometric domains, although it is quite lower than the lithium diffusion in insertion compounds. Another drawback of these transition metal oxides is their low electronic conductivity which contributes to the polarization of approximately 1 V from the *emf* value during discharge and charge.

There has been a large amount of fundamental studies on the electrochemical performance of transition metal oxides that has focused on reaction mechanisms, the development of possible intermediate phases, and the effect of particle size on electrochemical performance. However, to enhance the commercial viability of these materials and their application to large scale technology such as electric vehicles, practical improvements must be made in terms of capacity retention and cycle life [41].

1.5-2. Titanium oxides

Among the numerous transition metal oxides that provide suitable host lattices for reversible lithium insertion reactions, titanium oxides are interesting candidates [42, 43]. Titanium is abundant in nature, and titania is chemically stable, non toxic, environmentally friendly and an inexpensive option. TiO_2 can be produced in various forms such as anatase, rutile, brookite, TiO_2 B (bronze), TiO_2 R (ramsdellite), TiO_2 H (Hollandite), TiO_2 II (Columbite) and TiO_2 III (baddeleyite). However, TiO_2 in anatase form is considered the most electroactive lithium insertion host among these TiO_2 polymorphs [44]. The reaction of anatase with lithium takes place at about 1.75 V vs. Li, reaching a maximum $Li_{0.5}TiO_2$ stoichiometry by a biphasic mechanism. The performance is significantly improved by using nanostructured anatase electrodes (NAE), which enhances the lithium insertion rate while decreasing the diffusion lengths [45]. Thus, NAE-based anodes reduce the overall cell voltage, but provide cells with enhanced safety, good capacity retention on cycling, and low self-discharge. However, the capacity of TiO_2 is still unsatisfactory. Hence much research is needed to modify

and to improve its efficiency as anode and to exploit the other interesting physiochemical characteristics of this good semiconductor.

Lithium titanates have also attracted much attention. $Li_4Ti_5O_{12}$ is characterized by a flat discharge curve at approximately 1.55 V ascribed to the Ti^{4+}/Ti^{3+} redox couple. This high working voltage involves a decrease in the energy density of the full cell. However, it is safer and does not suffer side reactions with the electrolyte, which is responsible for the irreversible capacity of the first cycles in graphite anodes. A positive contribution to their good reversibility is that the lithium insertion does not induce structural changes during the charge-discharge process. On the other hand, the insulating character of $Li_4Ti_5O_{12}$ precludes its use for high current applications [46].

1.5-3. Tin and tin oxides

Lithium can form alloys with some metals. Owing to their ability to store large amounts of lithium, lithium metal alloys, Li_xM_y, are of great interest as high capacity anode materials in lithium-ion cells. Several factors are considered in the choice of lithium alloying metals for lithium-ion batteries. Physical properties considered include: atomic weight, Li/Metal ratio (value of "n"), and mass and volumetric capacity; while price and toxicity are given socio-economic considerations. Such alloys have specific capacities which exceed that of the conventional graphite anode; for example, $Li_{4.4}Sn$ (993 mAh g^{-1} and 1000 mAh cm^{-3}, versus 372 mAh g^{-1} and 855 mAh cm^{-3} for graphite), and $Li_{4.4}Si$ (4200 mAh g^{-1} and 1750 mAh cm^{-3}) [5, 37]. However, one of the most important problems preventing the use of tin materials as anode in Lithium-ion batteries is their poor cyclability owing to their significant volume changes (Fig. 1.5) as compared to graphite during lithium intercalation and de-intercalation. This results in the cracking and crumbling of the electrode (pulverization) and subsequent loss of electrical contact between active materials and the current collector. Such volume effect consequently declines the reversible capacity during charge –discharge cycling [37, 47, 48].
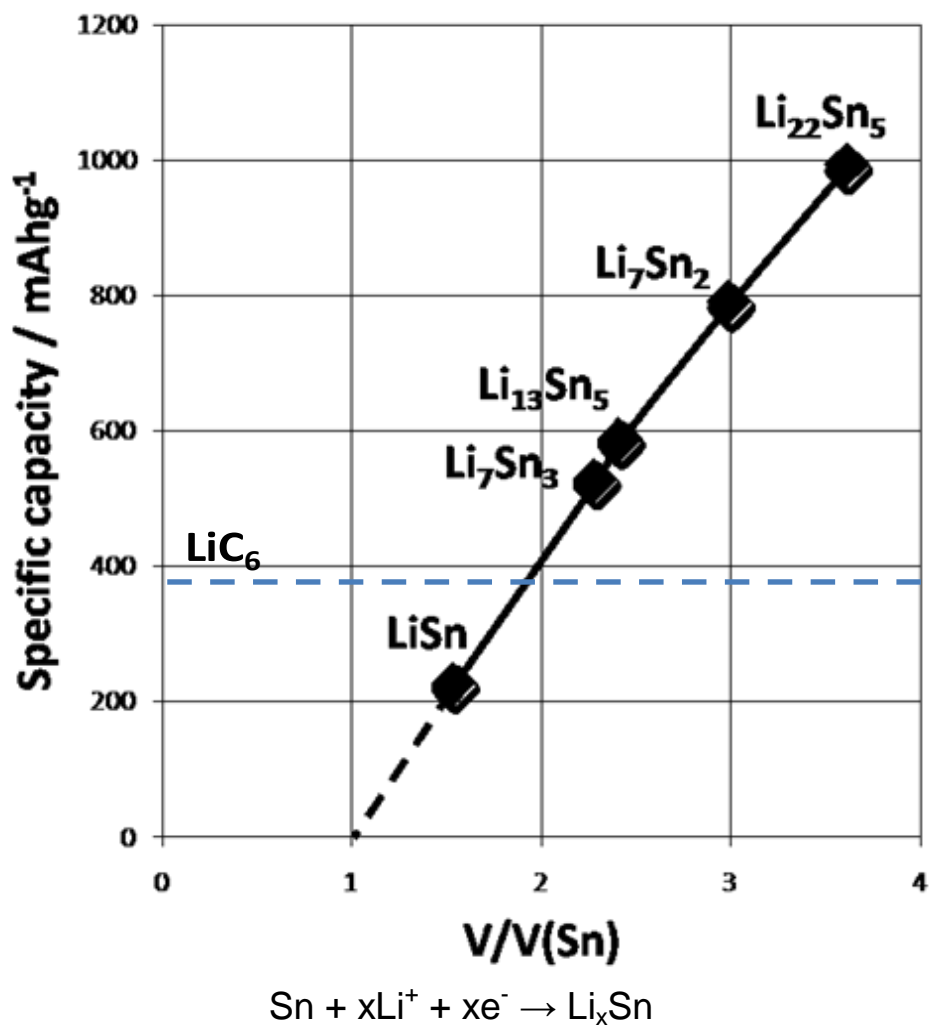
Figure 1.5. Specific capacities of various Li-Sn alloys and the corresponding ratio of volume expansion.

The use of nanostructured pure Sn seems not to be the ultimate solution. A procedure to improve the electrochemical behaviour of tin may be to form composite anodes in which the nanoparticles of tin are surrounded by a carbonaceous or organic matrix that buffers the volume change [49-51]. The carbonaceous matrix can prevent the aggregation of tin particles, buffer the volume change, and stabilize the surface of the particles.

Another strategy that has been proposed to improve the capacity retention of tin-based electrodes is the use of tin compounds. Materials based on tin oxide have been widely investigated since 1997 mainly on the basis of their high theoretical specific capacity of around 790 m Ah/g, low cost, safety and stable capacity retention [52-54].

The study of tin oxides have been reported, including SnO [55-57], and SnO_2 [58, 59].

The electrochemical reaction of lithium with tin dioxide involves two main steps. First, tin dioxide is converted to lithia and metallic tin:

$$4Li + SnO_2 = 2Li_2O + Sn$$
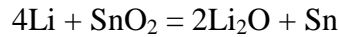
Second, the previously formed metallic tin reacts with lithium to form intermetallic phases:

$$xLi + Sn = Li_xSn \ (0 < x < 4.4)$$

Assuming a reversible alloying process of 4.4 Li per Sn, the maximum theoretical capacity for tin dioxide would be 781 mAhg^{-1}. The lithia forms a matrix that basically remains electrochemically inactive. However, during the extraction of lithium at potentials of around 2 V, certain tin-oxygen interactions have been observed, and partial tin reoxidation may occur [60]. To achieve good capacity retention, the potential window has to be limited within the approximate range of 0.1 to 0.9 V. Higher potential values in the upper limit may destroy the lithia matrix and lead to cell failure [61].

The reactions of Li with SnO can be written as follows:

$$2Li + SnO = Li_2O + Sn$$

$$xLi + Sn = Li_xSn \ (0 < x < 4.4)$$
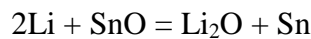
A main drawback of the tin oxides is the large irreversible consumption of lithium in the first cycle. The formation of a lithia matrix and surface films are involved

in this irreversibility [56]. The irreversible process would need an excess of positive electrode material in a lithium-ion battery that would be impractical for commercial use. The practical implementation of tin oxides is hampered by poor material cyclability arising from the large volume expansion-contraction experienced during discharge/charge cycling processes which causes electrode material pulverization and the loss of electrical contact [34]. Furthermore, SnO_2 has poor electronic conductivity; meaning that it must intimately be in contact with electronically conductive additives. This problem can be solved by nanostructuration and the use of a buffer matrix to avoid volume expansion during lithium alloying and de-alloying processes. From this point of view, SnO_2 nanowires can also be suggested as promising anode material because the nanowire structure is of special interest with predictions of unique electronic and structural properties. Furthermore, the nanowires can easily be synthesized by a thermal evaporation method. However, in its current form, this method of manufacture of SnO_2 nanowires has several limitations: it is inappropriate for mass production as high synthesis temperatures are required and there are difficulties in the elimination of metal catalysts that could act as impurities or defects. This results in reversible capacity loss or poor cyclic performance during electrochemical reactions [52].

1.5-4. Alloys and intermetallics

An alloy is a blend of metals that can be prepared by mixing the components when molten and then cooling the mixture. Alloys may be homogenous solid solutions, in which the atoms of one metal are distributed randomly among the atoms of the other. Intermetallic compounds have a definitive composition and internal structure [62]. Metal nanoparticles can be converted to alloys, typically through galvanic replacement reactions or through conversion of isolatable metal intermediates in "one-pot" reactions. Galvanic replacement reactions that use pre-made nanocrystals as precursors are particularly powerful, because they often provide a mechanism for controlling the morphology of the nanocrystal products. Alloying can also be done by the co-nucleation of two metals following reduction of metal salts and/or decomposition of metal complexes.

Intermetallic compounds represent a subset of alloys [63], containing exclusively two or more different kinds of metal (or metalloid). The difference between an intermetallic compound and a regular metal (e.g. a metallic element) is in the way the atoms bond. In metals, the bonding electrons distribute themselves throughout the material (i.e. the electrons are more localized), giving rise to predominantly non-directional bonding in the solid. Intermetallic compounds on the other hand, maintain a slight ionic and covalent character (i.e. electrons are localized), and the atomic bonding becomes more directional. This difference in bonding character results in differences in material behaviour.

The composition of most intermetallic compounds does not yield to the type of electron counting and oxidation-number analysis typically applied to more familiar solid-state compounds such as halides, oxides, and chalcogenides. It is therefore very difficult to predict the type of composition that would be stable in a given system of metallic elements and is even more complicated for quaternary compounds, e.g. $Sm_2NiAl_7Si_5$, etc [64].

In order to overcome the aforementioned problems, two approaches have been adopted recently. One approach is to use intermetallic compounds or active/inactive composite alloy materials such as Co-Sn, Ni-Sn, Sn-Sb, and Co-Sb [38]. Crystalline cobalt-tin phases, such as $CoSn$, $CoSn_2$ and Co_3Sn_2, and non-crystalline alloys are being studied [65, 66]. The ultimate role of the cobalt atoms is to avoid the volume changes of the Li_xSn phases and to help maintain the electrode integrity upon cycling. Carbon atoms help to achieve this goal but, in addition, carbon grains can contribute to the capacity for lithium intercalation. In contrast, the cobalt atoms decrease the global capacity. The study of the tin-rich phases of the cobalt-tin phase diagram might contribute the development of high capacity electrode materials.

The other approach is to use materials with a smaller particle size, with a higher surface to thickness ratio. The arrival of nanomaterials gave lithium-ion batteries a new lease of life and provided benefits in terms of capacity, power, cost and materials sustainability that are still far from being fully exploited [67]. As reported by Yang et al [68], the cycling stability of intermetallic anodes can be significantly improved by decreasing the particle size to submicron scale. Some advantages associated with the

application of nanomaterials include: enabling electrode reactions that ordinarily cannot take place for materials composed of micrometer-sized particles, significant increase in the rate of lithium insertion/de-insertion because of short distances for lithium-ion transport within the particles and enhanced electron transport. Also, the high surface area permits a high contact area with the electrolyte and hence a high lithium-ion flux across the interface, accommodation of the strain associated with intercalation, and enhanced Li-alloying kinetics [5, 69].

1.5.4-1.   Synthesis and challenges

Some of the most research efforts in current solid state chemistry are concerned with the design and prediction of new structures [70]. However, over the years, less attention has been focused on intermetallic compounds compared to the more ionic materials such as oxides, ceramics, chalcogenides or halides partly due to the difficulty in understanding some very basic characteristics e.g. compositions, bonding behaviour and reaction mechanism, and assignment of oxidation states for individual atoms. Consequently, bulk synthetic activity and innovation in solid state chemistry has focused primarily on the ionic type of materials, whereas typically the synthesis of intermetallic compounds has been carried out in fewer laboratories, and requires very high temperature conditions that are normally achieved by the use of induction heating and arc melting.

Synthesis is clearly one of the paramount frontier areas in the process of discovery of new materials and can be either exploratory or targeted. Different synthetic approaches often lead to different properties of the final material. The arsenal of synthetic methods for solid-state chemistry includes the direct combination high-temperature approaches, synthesis from fluxes and melts, hydrothermal synthesis, and synthesis from solutions, etc. To increase the odds for new compounds formation and to avoid the thermodynamic traps, the reactant diffusion must be increased so that the activation energy barrier (associated with solid-solid reactions) is lowered. Under these conditions the reaction could proceed at lower temperature to some other outcome. High diffusion rates (from solid-state perspective) could be achieved by simply allowing soluble starting materials to react in a solvent. Methods that permit reactions to be

carried out at lower temperature are likely to produce new phases. This applies to all classes of compounds including intermetallic phases [71].

Many techniques have been used in the synthesis of both bulk and nanomaterials. It is however noteworthy that the synthesis of intermetallic compounds/alloys (e.g.; Co-Sn) is very challenging and needs careful control of reaction parameters and synthesis conditions to achieve the desired result. However, when solids are dimensionally confined in the nanometer size regime, many interesting characteristics emerge that can be different from bulk analogs of the same material [63, 72]. Generally, some of the techniques include physical "top down" methods such as ball milling (mechanical milling/mechanical alloying) [73-77] and laser ablation are among the most straightforward, since they involve the direct size-reduction of already-made solids. While general for many classes of solids, it can be extremely difficult to control size, size dispersity, and morphology using these methods, which limits their utility. Other common synthetic strategies for nanocrystalline solids include gas-phase condensation sputtering and flame hydrolysis. Thin film deposition and annealing methods can also be used to form nanoparticles supported on a substrate. Also employed are thermal decomposition of organic complexes, co-precipitation, nucleation with inverse micelles or microemulsions, and solvothermal reactions [78-83]. Typically, reactions are performed in the presence of organic stabilizer, which help to passivate the nanocrystal surface, control its size and surface chemistry for solubility and surface accessibility, and influence growth directions to facilitate shape control.

1.5.4-2.   Co-Sn compounds

Cobalt is an anomalously fast diffuser in tin [84]. Amorphous as well as crystalline phases are known for the Co-Sn system. Thus, both crystalline CoSn compounds [85, 86] and poorly crystalline alloys have recently been studied as electrode-active materials for lithium-ion batteries [87-90]. Alcántara et al [91] prepared micro-CoSn by ball milling the elements Co and Sn in a 1:1 stoichiometric ratio, and then annealing the resulting mixture for 10 h at 500°C in an alumina crucible under Ar flow and the properties of microsized and nanosized Co-Sn were studied. Cable et al [82] prepared nano-CoSn based on a low-temperature one-pot method involving the

sequential $NaBH_4$ reduction of the metal salts in tetraethylene glycol (TEG), followed by heating under Ar-flow in the presence of poly(vinyl pyrrolidone) (PVP) and poly(2-ethyl-2-oxazoline) (PEO) as surface stabilizers. While crystalline Co_3Sn_2 is inactive against lithium [36, 92], amorphous Co_3Sn_2 prepared by a solvothermal route yielded a first capacity of 363 mAhg^{-1}, which decreased to below 250 mAhg^{-1} after 30 cycles [36]. Crystalline $CoSn_2$ exhibited around 300-400 mAhg^{-1} of reversible capacity after 10 cycles [85, 87]. A $CoSn_2$/Sn composite electrode had a reversible capacity of ca. 500 mAhg^{-1} after 30 cycles [88]. Amorphous CoSn alloy anodes obtained by electrodeposition on rough Cu foil showed more than 500 mAhg^{-1} after 20 cycles, while XRD peaks of unknown non-equilibrium phases accompanied by morphological changes were observed after cycling [89]. Kim and Cho observed the gradual crystallization of initially amorphous CoSn alloys after electrochemical cycling [93]. Fan and co-workers have studied the electrochemical behaviour of a commercial Sony electrode consisting of Sn-Co amorphous particles and also containing carbon and titanium. This electrode showed better electrochemical performance than crystalline tin [90].

The electrochemical behaviour of the Co-Sn system differs greatly from one phase to another, and it is also strongly influenced by particle size (Fig. 1.6).

The $CoSn_2$ phase with microsize particles shows great ability to react reversibly with lithium [85]. In contrast, CoSn [91] and Co_3Sn_2 [36, 94] poorly show significant capacities when nanometric particles are used. Moreover, stabilization of Co-Sn electrodes may involve the use of unknown phases [65, 92]. Large particles of the Co-rich compounds exhibit low capacity to react with lithium due to a slow diffusion of lithium that results in electrode overpotential. In nanoparticulate materials, the diffusion path length is shorter and the cobalt content is less critical.
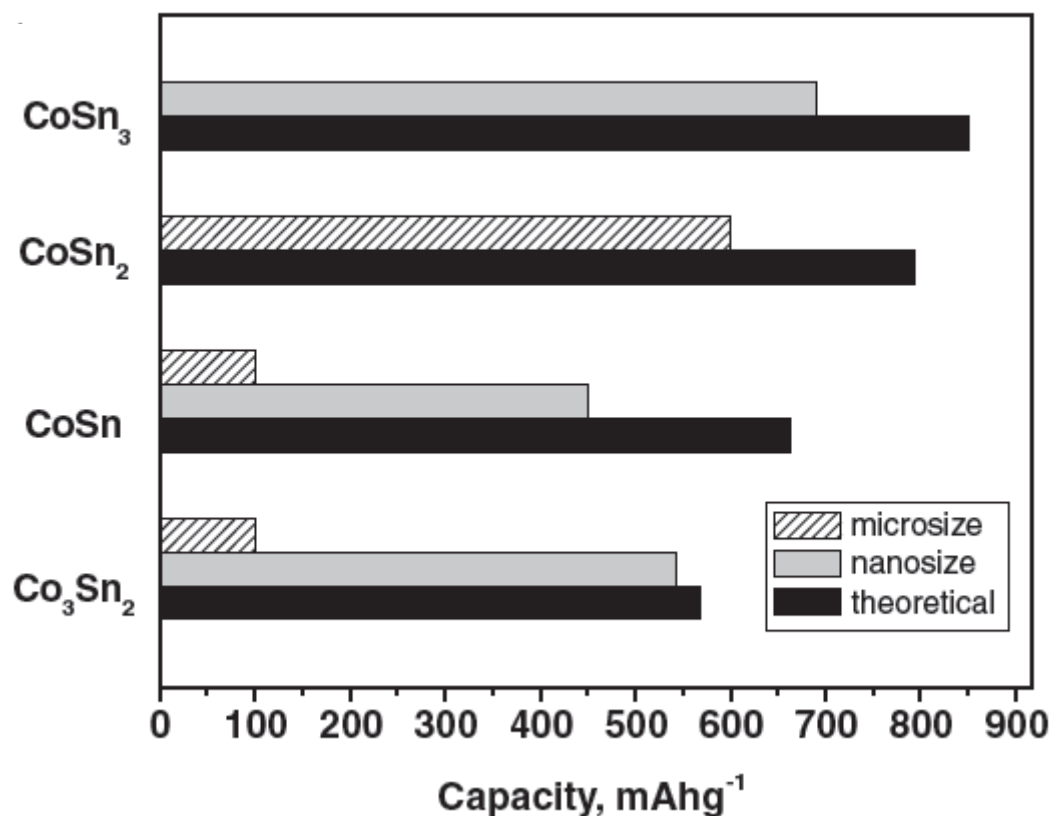
Figure 1.6. Capacities for $CoSn_x$ intermetallic electrodes. The theoretical capacity values calculated from the respective compositions and the experimental capacity values delivered by micrometric and nanometric particle size is shown [27].

Nanocarbons are a suitable option to support tin-based nanoparticles [95]. Nanoparticles of CoSn and Co_3Sn_2 deposited on carbon nanotubes have been prepared and the influence of the carbon nanotubes in preventing agglomeration of intermetallic particles was proposed [96]. The addition of organic polymers to tin-based electrodes has also been proposed a promising option [97]. The pyrolized material can form a matrix that improves the electrochemical behaviour due to the formation of stable solid/electrolyte interface and the ability to avoid nanoparticle aggregation upon cycling.

Nanostructured Sn-Co-C can be prepared in bulk by mechanosynthesis [98]. On the other hand, the occurrence of voids in intermetallic nanoparticles is usual and can be due to the Kirkendall effect [99]. The effects of these voids on the electrochemical behaviour have not yet been investigated.

The addition of binders has a great effect on the electrochemical behaviour of the anode materials formed by alloys [100-102]. To achieve an enhanced cycle life, the binder molecules should hold together the active material particles, thus avoiding the loss of electrical contact. According to Dahn´s group, the $Sn_{30}Co_{30}C_{40}$ electrodes using lithium polyacrylic acid (Li-PAA) and carboxymethyl cellulose (CMC) as binders show much smaller irreversible capacity than the ones using PVDF binder, and the electrodes using Li-PAA binder show excellent capacity retention [103].

$CoSn_3$ is an intermetallic compound that was recently discovered. This compound is difficult to synthesize using traditional high-temperature solid-state methods [99, 104]. However, we have studied the use of this compound in lithium-ion batteries [105] and high reversible capacity was observed. The preparation of nanostructured tin-based alloys is a hot topic and preparative routes such as sputtering and ball milling has been explored [98]. The difficulty in the synthesis of Co-Sn compounds is illustrated in the diagram below. Expectedly, it comprises of different intermetallic compounds; with different stability conditions and temperature.

Consider the phase diagram of the binary system cobalt-tin in Fig. 1.7. The compound designated as β-Co_3Sn_2 melts congruently (that is, the solid and liquid have the same composition) at 1180 °C. In contrast, CoSn melts incongruently at 966° C, forming solid β-Co_3Sn_2 and a liquid l, of a composition, which is indicated by the large down-pointing arrow in the phase diagram. Conversely, if a melt with a Co: Sn ratio of approximately 1:3 is cooled, the liquidus line will be reached at 966°C. On further cooling, the compound CoSn will crystallize until the sample reaches 571°C. At that temperature solid CoSn will react with the liquid (peritectic reaction) to form $CoSn_2$. The problem is that this phase forms an envelope around the reactant CoSn. Thus this reaction can now only proceed by diffusion through the solid envelope of $CoSn_2$. This diffusion process takes time and may not be finished before the sample reaches the next peritectic equilibrium temperature of 345°C. At that temperature (the high temperature

modification), β-CoSn$_3$ is formed. The melt changes its composition continuously, until the point where the remaining melt will solidify at the eutectic temperature of 229°C.
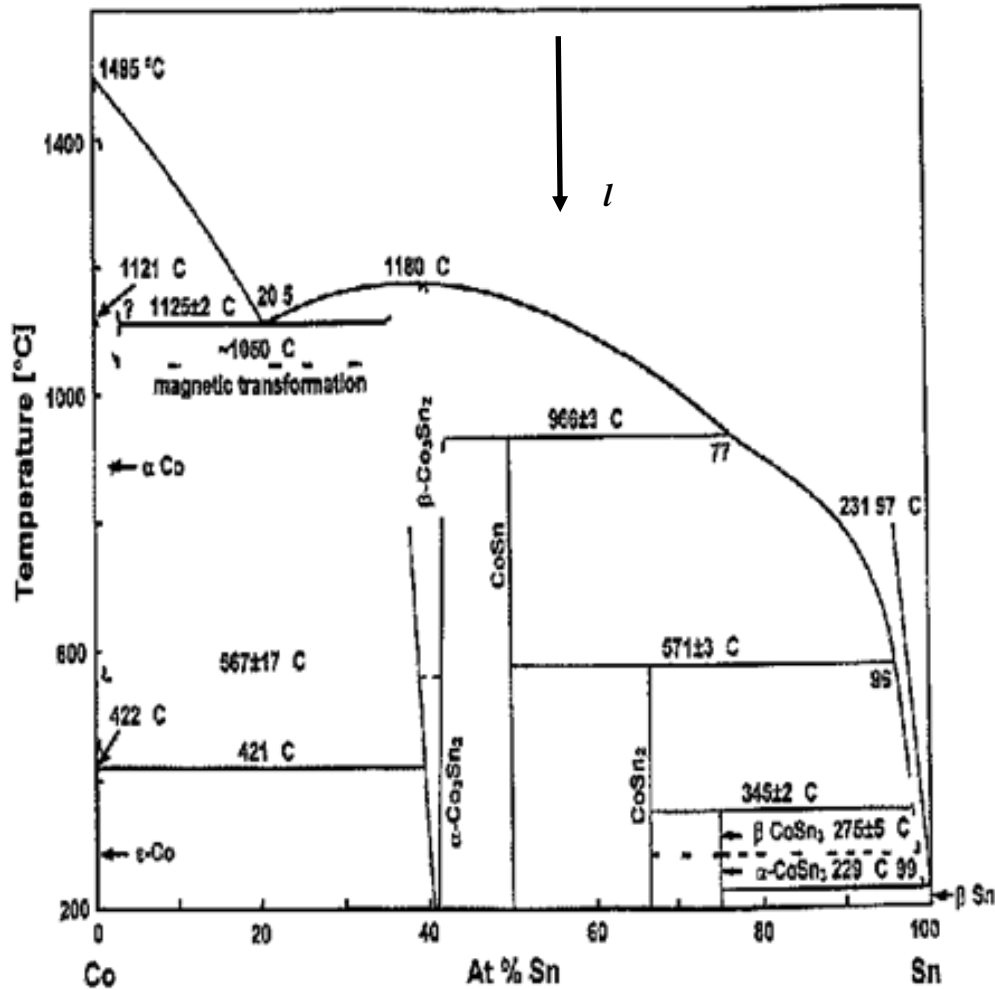

Figure 1.7. Phase diagram of the binary Cobalt-Tin system [104].

From the phase diagrams (Fig.1.7), it is clear that it is difficult to accurately estimate the different proportions of the reactants to yield the desired phase. However, this is not unexpected in exploratory research where the emphasis is on novel materials with potentially interesting properties.

CoSn₂

CoSn₂ belongs to the stannides represented as MSn₂ (M: Mn, Fe, Co) that adopts the CuAl₂ type of crystal structure. The CuAl₂ structure has a tetragonal unit cell and space group I4/mcm, in which Sn atoms occupy the 8h sites (x, x+½, 0) and Co atoms occupy the 4a sites (0, 0, ¼). The Co atom is surrounded 8 Sn atoms located at the corners of a square antiprism, with two additional Co neighbours along the c-axis forming linear chains, whereas the nearest neighbours of each Sn atom are 4 Co atoms [85, 106] with a crystal volume of 221.9 $Å^{3}$.
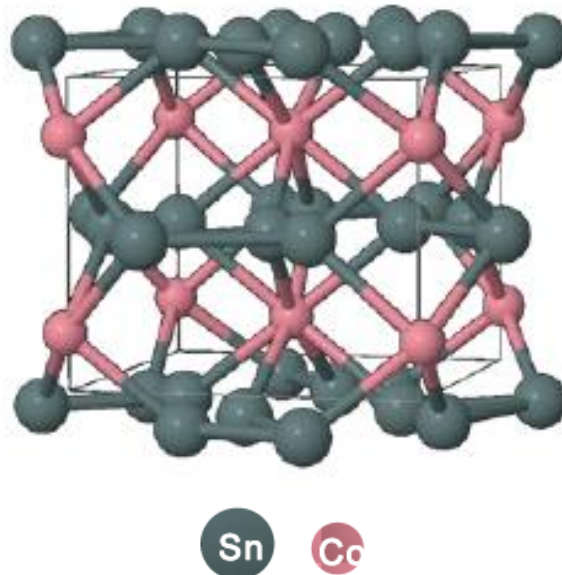

Figure 1.8. Crystal structure of CoSn₂. The Co atoms build chains parallel to the [001] plane (c-axis).

CoSn

The CoSn intermetallic compound adopts a hexagonal crystal structure. It belongs to the space group P6/mmm, no.191 (a = 5.2790(7), c = 4.259(10)) with Sn1 at

Wyckoff position 1a, Sn2 at 2d, and Co at 3f. The crystal structure crystal structure contains graphite-like 6^3 nets of Sn2 atoms and Kagomé nets of Co centred by the Sn1 atoms [91, 107]. This is a peculiar structure for an intermetallic compound because of the presence of a large void and large void and highly non-spherically coordinated Sn atoms (Fig. 1.9). This structural property is understood in terms of competition between covalent and metallic bonding in the system.

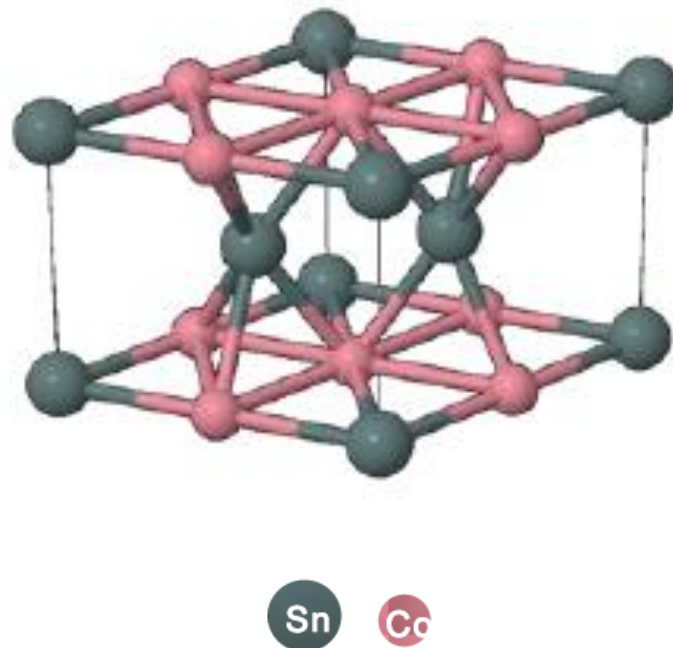**Figure 1.9.** Crystal structure of hexagonal CoSn. The larger dark spheres represent tin atoms and the smaller spheres represent cobalt atoms.

Co_3Sn_2

The intermetallic Co_3Sn_2 compound crystallizes in the NiAs($Sn8_1$) structure type (P6$_3$/mmc, Sn in Wyckoff position 2c and Co in 2a); according to Villars list 241. The

larger, more electronegative Sn forms a hexagonal closed-packed array and Co atoms are in all octahedral interstitials. The structure contains trigonal bipyramidal voids which may be filled to yield another common structure type, that of $Ni_2In(Sn8_2)$, often referred to as "stuffed" NiAs (Villars list 154). Partial occupancy of the trigonal bipyramids may either result in a disordered intermediate with partial occupancies, or in ordered super structures [108]. The lattice cell parameters are $a = 4.109$ Å, $c = 5.180$ Å (JCPDS File 27–1124) [36], and the structure is represented in Fig. 1.10.
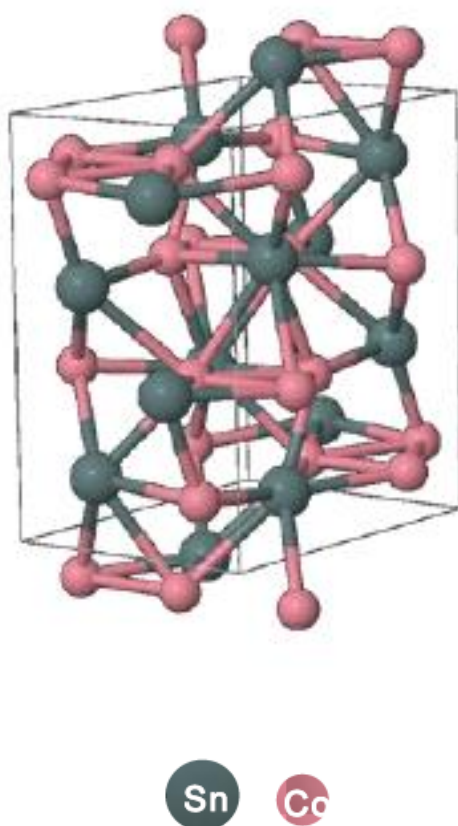

Sn   Co

Figure 1.10. Crystal structure of orthorhombic Co_3Sn_2.

CoSn₃

Generally, the two modifications of $CoSn_3$ are formed at relatively low temperatures and have been observed only in samples cooled at rates of 100 K/h or less.

At such low temperatures, the reactions are very slow and even with small cooling rates the samples are not in thermodynamic equilibrium. This may explain why the two modifications of $CoSn_3$ had been missed in earlier investigations of that binary system.

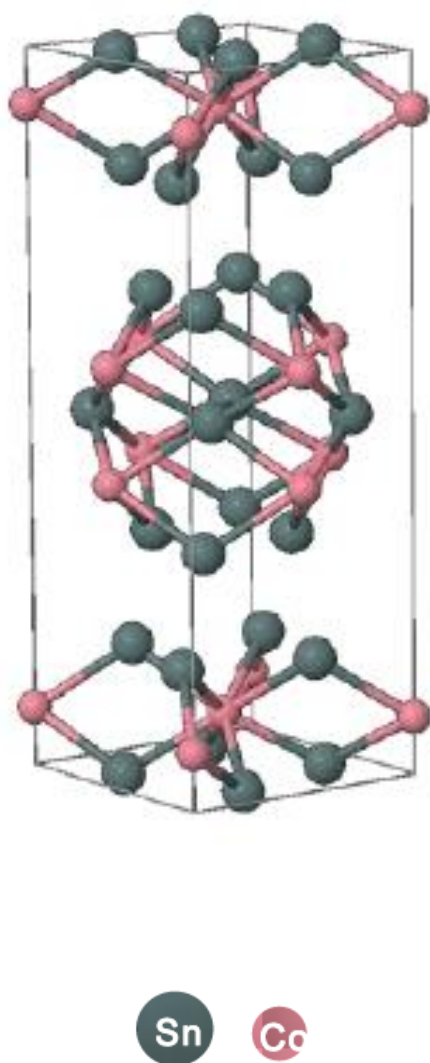**Figure 1.11.** Crystal structure of α-$CoSn_3$.

The high temperature β–modification of $CoSn_3$ crystallizes with a new structure type, while α-$CoSn_3$ shown in Figure 1.11 is isotropic with $PdSn_3$. The physical properties of the α modification should be very similar to those of β-$CoSn_3$ because the

two modifications are stacking variants of each other with the same coordination polyhedra of all atoms. The layered character of the $CoSn_3$ structures is emphasized in the figure. Since the packages always are terminated by tin atoms, two tin layers follow each other in going from one package to the next one; not two-dimensionally close packed as the tin layers contain not only tin triangles, but also tin squares. The low temperature α-$CoSn_3$ is orthorhombic; the general position is 16 fold with six variable positional parameters [104].

1.5.4-3.   Fe-Sn compounds

Under appropriate conditions, Fe reacts with Sn to form different $FeSn_x$ intermetallics. The application of these intermetallics as electrodes in lithium-ion batteries have been reported by various researchers. Mao et al. studied the electrochemical behaviour of $FeSn_2$ obtained by arc melting followed by mechanical alloying [109]. It is worth noting that isostructural $CoSn_2$ and $FeSn_2$ (*I4/mcm* space group) exhibit high capacity, irrespective of particle size. This feature suggests that structure plays an important role in making easier the insertion of lithium into these intermetallics. Several $FeSn_x$ phases with higher iron content, such as $FeSn$, Fe_3Sn_2, and Fe_5Sn_3, tend to form an electrochemically inactive "skin" of Fe over the surface of the active particles that prevents the full reaction with lithium [110] and the resulting capacities are lower than the theoretical values (Fig.1.12). Nanosized $FeSn_2$ exhibits 500 mAh g^{-1} of reversible capacity [111]. In order to improve the electrochemical behaviour, a composite electrode obtained by ball milling of Fe, Sn, and C was also reported [112].
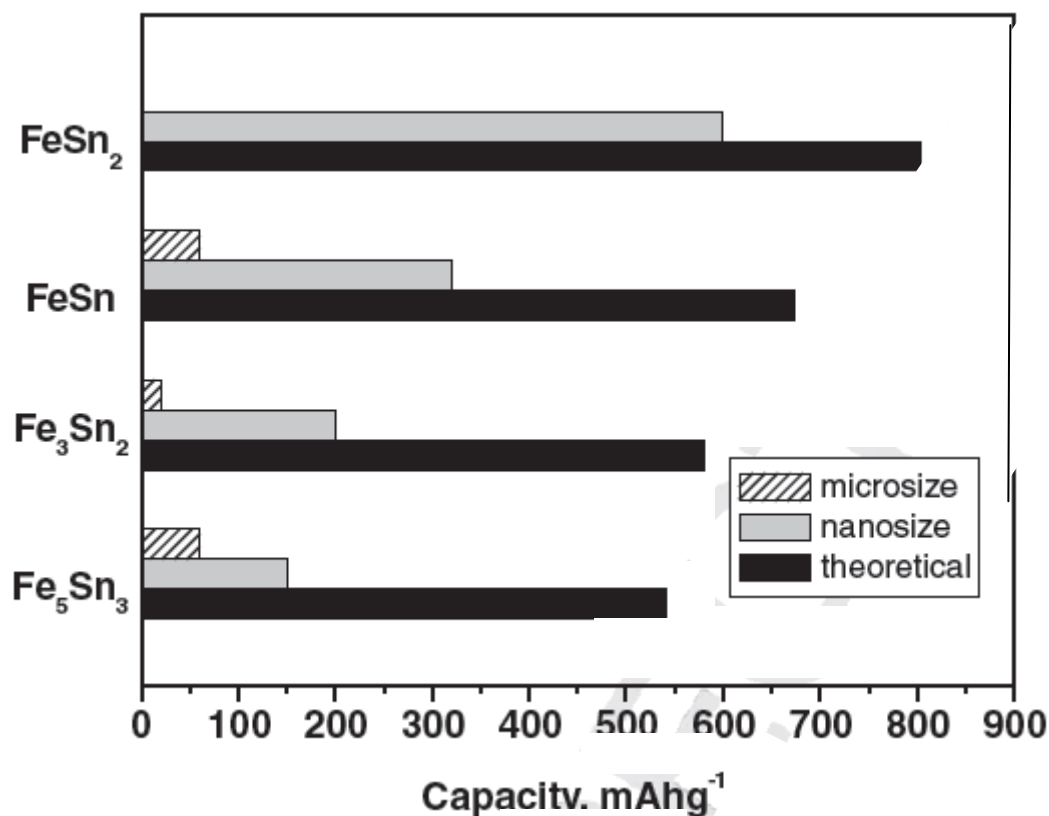
Figure 1.12. Capacities for $FeSn_x$ intermetallic electrodes. The theoretical capacity values calculated from the respective compositions and the experimental capacity values delivered by micrometric and nanometric particle size is shown [27].

For the Fe Sn system, six Fe-Sn intermetallic compounds were found in the phase diagram: $FeSn_2$, $FeSn$, $Fe_{1.3}Sn$, Fe_3Sn_2, Fe_5Sn_3, and Fe_3Sn. However, the lattice parameters of $Fe_{1.3}Sn$ (also called γ-FeSn) and of Fe_5Sn_3 are identical [113]. This mix-up is not unexpected considering the closeness of the synthesis temperatures and challenges in isolating the various phases. Altogether, the only intermetallic compounds in the iron-tin phase diagram are: $FeSn_2$, $FeSn$, Fe_3Sn_2, Fe_5Sn_3 and Fe_3Sn. The relevant phase diagram is shown in Fig. 1.13.
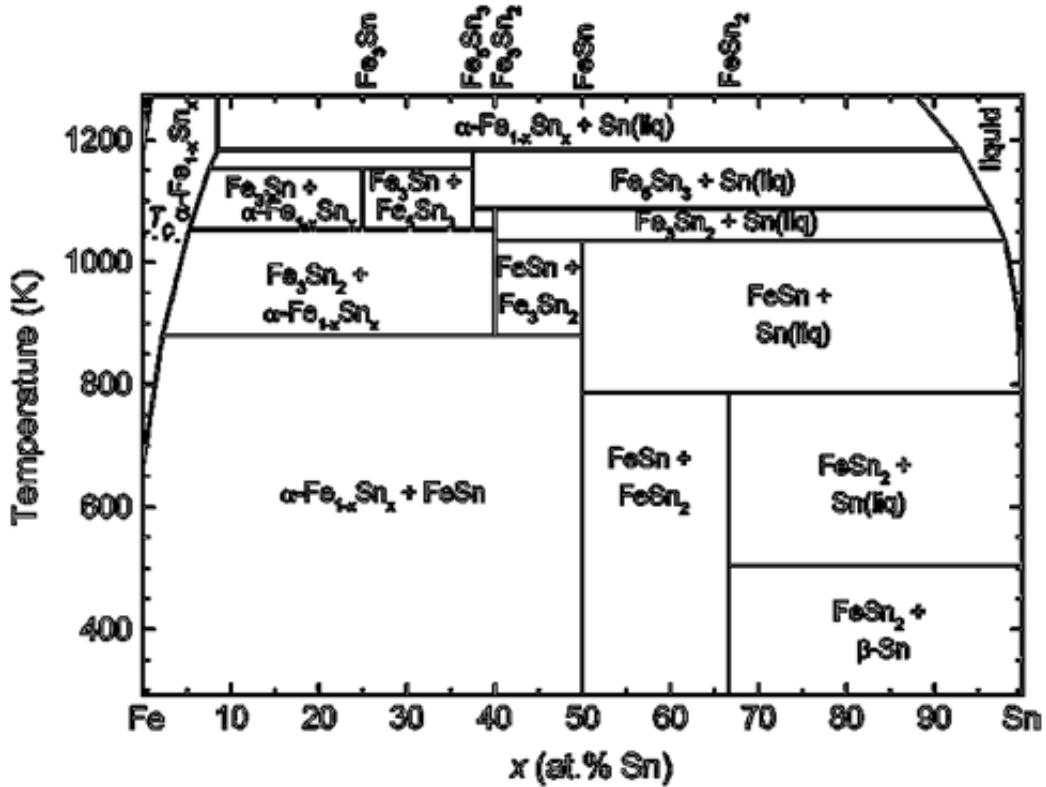
Figure 1.13. Phase diagram of Fe-Sn composition at various temperatures [113].

The iron-tin phase diagram shows that Sn is soluble in α-Fe to about 8.6% in contrast to Fe, which is practically insoluble in β-Sn. However, mechanical milling can increase the solubility of Sn in α-Fe to 32.7% [113].

$FeSn_2$

The stannides $FeSn_2$ and $CoSn_2$ are isostructural adopting the $CuAl_2$ type of crystal structure [114]. Therefore, the structure described above for $CoSn_2$ (Fig. 1.8) also applies for $FeSn_2$ and only substituting Co atoms for Fe atoms. All three MSn_2 compounds ($CoSn_2$, $MnSn_2$, and $FeSn_2$) show a metal-like temperature dependence of the electrical resistivity, ρ. While for $MnSn_2$ and $FeSn_2$ the resistivity is in the order of 100 μΩcm, (so called "bad" metals), $CoSn_2$ posses a significantly lower resistivity.

$FeSn_2$ has a crystal volume of 228.2 Å^3 and the phase diagram (Fig. 1.13) indicates phase stability of up to 786 K [113].

FeSn

FeSn has a hexagonal structure (CoSn, hP6, P6/mmm, SG No. 191, B35, Z = 3). Three Fe atoms occupy the 3f sites (½, 0, 0), 2 Sn atoms occupy the 2d sites (1/3, 2/3, 1/2), and 1 Sn atom occupies the 1a site (0, 0, 0). FeSn has a crystallographic density of 8.039 gcm^{-3} with a stability range of up to 1034 K (Fig. 1.13) [113].

Fe_3Sn_2

Fe_3Sn_2 adopts a rhombohedral structure (hR10, R-3m, SG No.166) with Z = 6 in a hexagonal unit cell. Fe occupies the 18h site (0.4949, -0.4949, 0.1134), the Sn$^{\#1}$ atoms occupy the 6c site (0, 0, 0.10387), and Sn$^{\#2}$ atoms occupy the 6c site (0, 0, 0.33158). The structure can be described as a particular stacking of the hexagonal unit cell of FeSn. This latter unit is repeated in the c-direction with a shift (2/3, 1/3, 1/3) and (1/3, 2/3, 2/3). The theoretical density of Fe_3Sn_2 is 8.243 gcm^{-3} with a stability range of 880-1088 K (Fig. 1.13) [113].

Fe_5Sn_3

Fe_5Sn_3 adopts a hexagonal structure (InNi$_2$, hP6, P6$_3$/mmc, SG No.194, B8$_2$, Z = 2/3). The 2a site (0, 0, 0) is fully occupied by Fe, but only 2/3 of the 2d site (1/3, 2/3, 3/4) is occupied by Fe atoms. The Sn atoms occupy the 2c site (1/3, 2/3, 1/4). The crystallographic density of Fe_5Sn_3 is between 8.670 and 8.693 gcm^{-3} with a stability range of 1053-1183 K (Fig. 1.13) [113].

Fe_3Sn

Fe$_3$Sn has a hexagonal structure (Ni$_3$Sn, hP8, P6$_3$/mmc, SG No.194, D0$_{19}$, Z = 2), in which Fe atoms occupy the 6h site (x, 2x, 1/4) and Sn atoms the 2c site (1/3, 2/3, 1/4). The unit cell parameters of Fe$_3$Sn are: a = 5.464 (1) Å, c = 4.352(1) Å and x = 0.844(1). It has a theoretical density of 8.445 gcm^{-3} and is stable between 1053 and 1153 K (Fig. 1.13) [113].

### 1.5-5.	Silicon-based negative electrode materials

Silicon is the second most abundant element in the earth´s crust. Although it is not naturally occurring in its free state, its extraction and purification processes are highly developed because of the need of modern electronics. The theoretical capacity produced upon the formation of Li$_{4.4}$Si is 4200 m Ah/g [115]. However, it has been observed that after the 5th electrochemical cycle, the capacity of bulk silicon is reduced by 90%. The main reason for this capacity loss is the pulverization that the silicon undergoes due to the 300% expansion it experiences upon the formation of lithium alloy. The use of nanoparticles is known to reduce the lithium diffusion path length of lithium electrodes, thus improving the rate performance. However, nanocrystalline forms obtained by heat treatment of silicon inverse opals proved to be unstable to the mechanical stresses induced by volume changes, leading to rapid loss of electrode capacity [116]. Over the years, several modifications have been proposed by various authors; tailoring of particle shape so as to reduce mechanical stress [117], the use of silicon nanowires prepared on a substrate [118], the use of composites containing intimately mixed carbon and silicon particles, more complex procedures such as thermal vapour decomposition methods to produce carbon silicon [119]. Also during cycling, the electrolyte decomposes on the electrode, forming a solid electrolyte interface (SEI) passivation layer on the electrode surface; this layer covers the Si active site thus affecting its ability to host lithium ions. However, coating the Si/C with a hard carbon shell protects the silicon, as the SEI passivation layer forms on the hard carbon shell thereby reducing the capacity degradation during cycling. The cyclability of nanostructured Si/C is better than that of pure nanosilicon due to the fact that carbon buffers the expansion of silicon and therefore minimizes the mechanical damage of the silicon active sites. The cyclability of carbon-coated Si/C is even better, as the carbon

coating offers additional stability from both mechanical and electrochemical point of view [115]. In summary, nanostrutured silicon could offer the highest capacities. However, several difficult problems are still to be resolved such as huge irreversible capacities and not easily scalable preparative routes.

1.6.   Electrolytes for lithium-ion batteries

Electrolyte decomposition and passivating film formation contribute to decrease of the efficiency in the charge/discharge of lithium-ion batteries. Electrolytes are substances that contain free ions that make them electrically conductive. They allow mutual ionic exchange between the battery electrodes. The electrolyte phase can consist of a liquid salt solution, polymer gel or a glassy solid. In addition to large potential window, E_g, the electrolyte must satisfy several additional requirements such as: retention of the electrode/electrolyte interface during cycling when the electrode particles are changing their volume, a Li^+ -ion conductivity $\sigma_{Li} > 10^{-4}$ S/cm over the temperature range of the battery operation, an electronic conductivity $\sigma_e < 10^{-10}$ S/cm, a transference number $\sigma_{Li}/\sigma_{total} \approx 1$, where σ_{total} includes conductivities by other ions in the electrolyte as well as $\sigma_{Li} + \sigma_e$. Others include chemical stability over ambient temperature ranges and temperatures in the battery under high power, chemical stability with respect to the electrodes, including the ability to form rapidly a passivating SEI layer where kinetic stability is required because the electrode potential lies outside the electrolyte window, and preferably non flammable, of low toxicity and cost [120].

1.6-1. Liquid electrolytes

The lithium battery could not function in an aqueous electrolyte since its voltage provides an oxidizing environment, resulting in electrolyte decomposition.

The high H^+ ion conductivity required of an aqueous electrolyte over the practical ambient-temperature range is only found in liquid or immobilized-liquid water. The energy of separation E_g between the highest occupied molecular orbital (HOMO) and the lowest unoccupied molecular orbital (LUMO) is ≈ 1.3 eV. This limits the open circuit voltage V_{oc} for the aqueous electrolyte. In order to obtain a cell with a higher V_{oc}

and therefore a higher energy density, it is necessary to turn to nonaqueous electrolytes with a larger E_g [120].

Organic solvents such as propylene carbonate (PC), ethylene carbonate (EC), diethyl carbonate (DEC) and dimethyl carbonate (DMC), with a large potential window (stable potential domain) containing dissolved electrolyte salts; lithium salts such as $LiClO_4$, $LiPF_6$, and $LiBF_4$ are stable to high voltage, low in toxicity and cost effective for use in practical lithium-ion batteries [6, 16].

Table 1.3. Characteristics of organic solvents [11].

Characteristic	EC	PC	DMC	EMC	DEC	1,2-DME	AN	THF	γ-BL
BP (°C)	248	242	90	109	126	84	81	66	206
MP (°C)	39	−48	4	−55	−43	−58	−46	−108	−43
Density (g/ml)	1.41	1.21	1.07	1.0	0.97	0.87	0.78	0.89	1.13
Viscosity (cP)	1.86 (40°C)	2.5	0.59	0.65	0.75	0.455	0.34	0.48	1.75
Dielectric constant	89.6 (40°C)	64.4	3.12	2.9	2.82	7.2	38.8	7.75	39
Donor number	16.4	15	8.7 [70]	6.5 [70]	8 [70]	—	14	–	—
Mol. wt.	88.1	102.1	90.1	104.1	118.1	90.1	41.0	72.1	86.1

* EC = ethylene carbonate, PC = propylene carbonate, DMC = dimethyl carbonate, EMC = ethyl methyl carbonate, DEC = diethyl carbonate, DME = dimethyl ether, AN=acetonitrile, THF =tetrahydrofuran, γBL = γ-butyrolactone.

Pure propylene carbonate (PC) is not used in lithium ion cells, as it causes exfoliation of the carbon-based electrode [121]. The solvent mixtures properties in intercalation cells for the binary mixtures of EC + DEC, and EC + DMC, and the ternary EC + DEC + DMC with 1M $LiPF_6$ was investigated by Ratnakumar et al. [122]. At ambient temperatures, the ionic electrolyte conductivity is highest for the EC + DEC mixture, as are the self-discharge and the irreversible capacity. The DMC-based electrolytes exhibit low irreversible capacity, capacity fade and self discharge, due to the protective nature of the interfacial film formed on the carbon electrode. However, the properties of the ternary mixture excel at low temperatures (< 0°C) [123].

1.6-2.　　　　Solid and gel electrolytes

Inorganic solid Li^+ ion conducting materials having a $\sigma_{Li} > 10^{-4}$ S/cm have been considered for Li-based electrolytes, as have been extensively reviewed [124], because they have a wide electrochemical window and additionally meet most of the requirements except that there is poor retention of the electrode/electrolyte interface during cycling when the particles are changing their volume. This has excluded inorganic solid Li^+-ion electrolytes from consideration for large scale batteries having solid electrodes. They have only been used in thin-film battery applications [120]. The solid electrolytes based on lithium sulphide (Li_2S) show high ionic conductivity, but are unstable in air, while Li_2O based electrolytes show high stability, but low conductivity. However, both materials decompose in direct contact with metallic lithium. Lithium superionic conductors, which can be used as solid electrolytes, exhibit a high ionic diffusion in the mobile ion sublattice at temperatures well below their melting points. Recently, Kamaya et al. [125] studied the electrochemical behaviour of $Li_{10}GeP_2S_{12}$ (a lithium superionic conductor) synthesized by reacting stoichiometric quantities of Li_2S, GeS_2 and P_2S_5 at 550°C in an evacuated quartz tube. The new $Li_{10}GeP_2S_{12}$ with a one-dimensional conduction pathway exhibits an extremely high bulk conductivity of over 10^{-2} S cm^{-1} at room temperature (27°C), thus making it the first electrolyte that has an ionic conductivity that is comparable to or even higher than those of liquid organic systems with much higher chemical and thermal stabilities. An all-solid-state battery with the structure $LiCoO_2/ Li_{10}GeP_2S_{12}/In$ exhibits an excellent battery performance.

Gel electrolytes are made by impregnation of organic liquid electrolytes consisting of a solvent mixture, such as ethylene carbonate and propylene carbonate, and lithium salts such as $LiPF_6$, into host polymers such as polyacrylonitrile, poly (vinylidene fluoride), and polyether. The activation energy of lithium ion conduction is around 0.2 eV, which is comparable to that of organic liquid electrolytes. The ionic conductivity depends on the weight ratio of host polymer/organic liquid electrolyte. To increase ionic conductivity, more liquid electrolytes are needed but giving rise to a safety problem associated with the use of flammable organic liquid electrolytes in conventional batteries. Therefore, breakthroughs are required to improve lithium ion conductivity and in the methodology to form good interface between electrolyte and active material [126].

Other hybrid electrolytes include ionic liquid + polymer electrolyte (ionic liquid-polymer gel), ionic liquid + polymer electrolyte + liquid organic electrolyte, ionic liquid + liquid organic electrolyte, and polymer + inorganic solid electrolyte [120].

REFERENCES

1. N. Armaroli, V. Balzani, Angew. Chem. Int. Ed., 46 (2007) 52.

2. International Energy Agency World Energy Outlook, 1996 Edition. Edited by Ken Wigley.

3. US Energy Information; International Energy Outlook, 2010 (www.eia.gov/oiaf/ieo7index.html).

4. S. Yoda, K. Ishihara, J. Power Sources, 81-82 (1999) 162.

5. P.G. Bruce, B. Scrosati, J. –M. Tarascon, Angew. Chem. Int. Ed., 47 (2008) 2930.

6. D. Berndt, Battery Technology HandBook, 2nd Ed., Expert Verlag, 2003.

7. D. Linden, T.B. Reddy (Editors), HandBook of Batteries, 3rd Ed. McGraw-Hill, New York (2001).

8. P. Lavela, J.L. Tirado, Baterías Avanzadas, Servicio de Publicaciones de la Universidad de Cordoba (1999).

9. J.M Tarascon, M. Armand, Nature, 414 (2003) 359.

10. A. Manthiram, J. Kim, Chem. Mater., 10 (1998) 2895.

11. D. Linden, T.B. Reddy, "Handbook of Batteries", 3rd Edition, Mc-Graw Hill (2002).

12. T. Minami, M. Tatsumisago, M. Wakihara, C. Iwakura, S. Kohjiya, I. Tanaka, "Solid State Ionics for Batteries", Springer-Verlag, Tokyo (2005).

13. H. Chen, X. Qiu, W. Zhu, P. Hagenmuller, Electrochem. Comm., 4 (2002) 488.

14. M. Winter, J.O. Besenhard, M.E. Spahr, P. Novak, Adv. Mater., 10 (1998) 725.

15. M.G. Kanatzidis, K.R. Poeppelmeier, Reports of The Third Workshop on Future Directions of Solid State Chemistry: The Status of Solid State Chemistry and its Impact in the Physical Sciences, Northw estern University, Evanston Illinois, USA, 2006.

16. R. Alcántara, P. Lavela, J.L. Tirado, E. Zhecheva, R. Stoyanova, J. Solid State Electrochem, 3 (1999) 121.

17. H. Gabrisch, Y. Ozawa, R. Yazami, Electrochim. Acta, 52 (2006) 1499.

18. T. Nohma, H. Kurokawa, M. Uehara, M. Takahashi, K. Nishio, T. Saito, J. Power Sources, 54 (1995) 522.

19. Y. Shao-Horn, L. Croguennec, C. Delmas, E. Chris Nelson, M.A. O´Keefe, Nat. Mater., 2 (2003).

20. J. Zhang, Y.J. Xiang, Y. Yu, S. Xie, G.S. Jiang, C.H. Chen, J. Power Sources, 132 (2004) 187.

21. A.W. Moses, J. Kim, H.G. Garcia Flores, M. Langell, Appl. Surf. Sci., 253 (2007) 4782.

22. R. Alcántara, G.F. Ortiz, P. Lavela, J.L. Tirado, R. Stoyanova, E. Zhecheva, Chem. Mater., 18 (2006) 2293.

23. H. Wulff, M. Mohan Rao, and F. Scholz, Chem. Mater., 15 (2003) 988.

24. C. Lu, H. Chang, C. Yen, Tamkang, J. Sci. Eng., 4 (2004) 199.

25. R. Stoyanova, E. Zhecheva, S. Angelov, Solid State Ionics 59 (1993) 17.

26. M.M. Thackery, Prog. Solid St. Chem., 25 (1997) 1.

27. V.V. Kharton, Handbook of Solid State Electrochemistry, Volume 2., Wiley-VCH Verlag GmBH & Co. KGaA (2011).

28. B. Ammundsen, J. Paulsen, Adv. Mat., 13 (2001) 943.

29. R. Chen, M.S. Whittingham, J. Electrochem. Soc., 144 (1997) L64.

30. A.K. Padhi, K.S. Nanjundaswamy, J.B. Goodenough, J. Electrochem. Soc., 144 (1997) 1188.

31. A.K. Padhi, K.S. Nanjundaswamy, C. Masquelier, S. Okada, J.B. Goodenough, J. Electrochem. Soc., 144 (1997) 1609.

32. A. Manthiram, J.B. Goodenough, J. Solid State Chem., 71 (1987) 349.

33. A. Manthiram, J.B. Goodenough, J. Power Sources, 26 (1989) 403.

34. M. Winter, J.O. Besenhard, M. Spahr, P.Novak, Adv. Mater., 10 (1998) 10.

35. R. Alcántara, P. Lavela, J.L. Tirado, R. Stoyanova, E. Kuzmanova, E. Zhecheva, Chem. Mater., 9 (1997) 2145.

36. J. Xie, X.B. Zhao, G.S. Cao, J.P. Tu, J. Power Sources, 164 (2007) 386.

37. J.L. Tirado, Mat. Sci. & Eng. R, 40 (2003) 103.

38. R. Alcántara, F.J. Fernández-Madrigal, P. Lavela, J.L. Tirado; J.C. Jumas, J. Olivier-Fourcade, J. Mater. Chem., 9 (1999) 2517.

39. B. Scrosati, J. Electrochem. Soc., 139 (1992) 2776.

40. Y. Nishi, J. Power Sources, 100 (2001) 101.

41. S.A. Needham, G.X. Wang, K. Konstantinov, Y. Tournayre, Z. Lao, H.K. Liu, Electrochem. Solid State Lett.,9 (2006) A315.

42. P. Poizot, S. Laruelle, S. Grugeon, L. Dupont, J.M. Tarascon, Nature, 407 (2000) 496.

43. P. Poizot, S. Laruelle, S. Grugeon, L. Dupont, J.M. Tarascon, J. Power Sources, 97-98 (2001) 235.

44. M. Zukolova, M. Kalbac, L. Kavan, I. Exnar, M. Gratzel, Chem. Mater., 17 (2005) 1248.

45. S. Huang, L. Kavan, I. Exnar, M. Gratzel, J. Electrochem. Soc., 142 (1995) L142.

46. T. Ohzuku, A. Ueda, N. Yamamoto, J. Electrochem. Soc., 142 (1995) 1431.

47. Y. Wang, M. Wu, Z. Jiao, J.Y. Lee, Chem. Mater., 21 (2009) 3210.

48. L.Y. Beaulieu, K.W. Eberman, R.L. Turner, L.J. Krause, J.R. Dahn, Electrochem. Solid-State Lett., 4 (2001) A137.

49. E. Kim, D. Son, T.G. Kim, J. Cho, B. Park, K.S. Ryu, S.H. Chang, Angew. Chem. Int. Ed., 43 (2004) 5987.

50. M. Noh, Y. Kwon, H. Lee, J. Cho, Y. Kim, M.G. Kim, Chem. Mate., 17 (2005) 1926.

51. X.M. He, W.H. Pu, L. Wang, J.G. Ren, C.Y. Jiang, C.R. Wan, Solid State Ionics 178 (2007) 833.

52. M. Park, G. Wang, Y. Kang, D. Wexler, S. Dou, H. Liu, Angew. Chem. Int. Ed., 46 (2007) 750.

53. M. Winter, J.O. Besenhard, Electrochim. Acta, 45 (1999) 31.

54. J. Hassoun, S. Panero, P. Reale, B. Scrosati, Int. J. Electrochem. Sci., 1 (2006) 110.

55. I.A. Courtney, J.R. Dahn, J. Electrochem. Soc., 144 (1997) 2045.

56. D. Aurbach, A. Nimberger, B. Markovsky, E. Levi, A. Gedanken, Chem. Mater., 14 (2002) 4155.

57. A.P. Hightower, P. Delcroix, G. LeCaer, C.K. Huang, B.V. Ratnakumar, C.C. Ahn, B. Fultz, J. Electrochem. Soc., 147 (2000) 1.

58. R. Alcántara, F.J. Fernandez-Madrigal, C. Perez-Vicente, J.L. Tirado, J.C. Jumas, J. Olivier-Fourcade, Chem. Mater., 12 (2000) 3044.

59. L.A. O´Dell, S.L.P. Savin, A.V. Chadwick, M.E. Smith, Nanotechnology 16 (2005) 1836.

60. I. Sandu, T. Brousse, D.M. Schleich, M. Danot, J. Solid State Chem.,179 (2006) 476.

61. I.A. Courtney, J.R. Dahn, J. Electrochem. Soc., 144 (1997) 2943.

62. D.F. Shiver, P.W. Atkins, C.H. Langford, "Inorganic Chemistry", Oxford University Press (1990).

63. Y. Vasquez, A.E. Henkes, J.C. Bauer, R.E. Schaak, J. Solid State Chem., 181 (2008) 1509.

64. M.G. Kanatzidis, R. Pottgen, W. Jeitschko, Angew. Chem. Int. Ed., 44 (2005) 6996.

65. G.F. Ortiz, R. Alcántara, I. Rodríguez, J.L. Tirado, J. Electroanal. Chem., 605 (2007) 98.

66. H. Kim, J. Cho, Electrochim. Acta, 52 (2007) 4197.

67. M. Armand J.M. Tarascon, Nature, 451 (2008) 652.

68. J. Yang, Y. Takada, N. Imanishi, O. Yamamoto, J. Electrochem. Soc., 146 (1999) 4009.

69. M. Wachtler, M. Winter, J.O. Besenhard, J. Power Sources, 105 (2002) 151.

70. Y. Wang, I. Djerdj, B. Smarshy, M. Antonietti, Chem. Mater., 21 (2009) 3202.

71. L. Smart, E. Moore, "Solid State Chemistry, An Introduction", 2nd Edition, Chapman and Hall (1995).

72. M. Jain, T. Christman, Acta. Metall. Mater., 6 (1994) 1901.

73. C.C. Koch, J.D. Whittenberger, Intermetallics , 5 (1996) 339.

74. E. Ma, M. Atzmon, Mater. Chem. Phys., 39 (1995) 249.

75. R.B. Schwarz, P.B. Desch, S. Srinivasan, P. Nash, Nanostruct. Mater., 1 (1992) 37.

76. Z.G. Liu, J.T. Guo, L.L. He, Z,Q. Hu, Nanostruct. Mater., 7 (1994) 787.

77. A. Calka and A.P. Radlinski, Scripta Metallurgica, 9 (1989) 1497.

78. U.G. Nwokeke, R. Alcántara, J.L. Tirado, R. Stoyanova, M. Yoncheva, E. Zhecheva, Chem. Mater., 22 (2010) 2268.

79. U.G. Nwokeke, R. Alcántara, J.L. Tirado, R. Stoyanova, E. Zhecheva, J. Power Sources, 196 (2011) 6768.

80. U.G. Nwokeke, A. Chadwick, R. Alcántara, M. Alfredsson, J.L. Tirado, J. Alloys Compd., 509 (2011) 3074.

81. M. Rajamathi, R. Seshadri, Curr. Opin. Solid State Mater. Sci., 6 (2002) 337.

82. R.E. Cable and R. Schaak, Chem. Mater., 17 (2005) 6835.

83. N.H. Chou, R. Schaak, Chem. Mater., 20 (2008) 2081.

84. P. Guilmin, P. Guyot, G. Marchal, Phys. Lett. A, 109 (1985) 230.

85. C.M. Ioniqua-Bousquet, P.E. Lippens, L. Aldon, J. Olivier-Fourcade, J.C. Jumas, Chem. Mater., 18 (2006) 6442.

86. R. Alcántara, G.F. Ortiz, J.L. Tirado, ChemPhysChem., 8 (2007) 80.

87. M.Z. Xue, Z.W. Fu, Solid State Ionics, 177 (2006) 1501.

88. H. Guo, H. Zhao, X. Jia, X. Li, W. Qiu, Electrochim. Acta, 52 (2007) 4853.

89. N. Tamura, Y. Kato, A, Mikami, M. Kamino, S. Matsuta, Fujitani, J. Electrochem. Soc., 153 (2006) A1626.

90. Q. Fan, P.J. Chupas, M.S. Whittingham, Electrochem. Solid-State Lett., 10 (2007) A274.

91. R. Alcántara, I. Rodríguez, J.L. Tirado, ChemPhysChem., 9 (2008) 1171.

92. J.R. Dahn, R.E. Mar, A. Abouzeid, J. Electrochem. Soc., 153 (2006) A361.

93. H. Kim, J. Cho, J. Electrochem. Soc., 154 (2007) A462.

94. R. Alcántara, G. Ortiz, I. Rodríguez, J.L. Tirado, J. Power Sources, 189 (2009) 309.

95. G.F. Ortiz, R. Alcántara, P. Lavela, J.L. Tirado, J. Electrochem. Soc., 152 (2005) A1797.

96. L. Huang, J.S. Cai, Y. He, F.S. Ke, S.G. Sun, Elecrochem. Commun., 11 (2009) 950.

97. U.G. Nwokeke, F. Nacimiento, R. Alcántara, J.L. Tirado, Electrochem. Solid-State Lett., 14 (2011) A148.

98. P.P. Ferguson, A.D.W. Todd, J.R. Dahn, Electrochem. Commun., 10 (2008) 25.

99. N.H. Chou, R.E. Schaak, J. Am. Chem. Soc., 129 (2007) 7339.

100. M.R. Wagner, M. Wachtler, M. Schmied, P. Preishuber-Pflugl, F. Stelzer, J.O. Besenhard, M. Winter, Abstract 73 at 10th International Meeting of Lithium Batteries (IMLB), Como (Italy), 2000.

101. N.S. Hochgatterer, M.R. Schweiger, S. Koller, P.R. Raimann, T. Wohrle, C. Wurm, M. Winter, Electrochem. Solid-State Lett., 11 (2008) A76.

102. Z. Chen, V. Chevrier, L. Christensen, J.R. Dahn, Electrochem. Solid-State Lett., 7 (2004) A310.

103. J. Li, D.B. Le, P.P. Ferguson, J.R. Dahn, Electrochim. Acta 55 (2010) 2991.

104. A. Lang, W. Jeitschko, Z Metallkd., 87 (1996) 759.

105. R. Alcántara, U. Nwokeke, I. Rodríguez, J.L. Tirado, Electrochem. Solid-State Lett., 11 (2008) A209.

106. U.G. Nwokeke, F. Nacimiento, J.R. González, R. Alcántara, J.L. Tirado, C. Perez-Vicente, 5th International Meeting on Developments in Materials, Processes and Applications of Emerging Technologies, Alvor (Portugal) June (2011).

107. A.K. Larsson, M. Haeberlein, S. Lidin, U. Schwarz, J. Alloys Compd., 240 (1996) 79.

108. A.K. Larsson, L. Stenberg, S. Lidin, Acta Chem. Scandinavica, 49 (1995) 800.

109. O. Mao, R.D. Dunlap, J.R. Dahn, J. Elecrochem. Soc., 146 (1999) 405.

110. O. Mao, J.R. Dahn, J. Elecrochem. Soc., 146 (1999) 414.

111. C.Q. Zhang, J.P. Tu, X.H. Huang, Y.F. Yuan, S.W. Wang, F. Mao, J. Alloys Compd., 457 (2008) 81.

112. O. Mao, R.L. Turner, I.A. Courtney, B.D. Fredericksen, M.I. Buckett, L.J. Krause, J.R. Dahn, Electrochem. Solid-State Lett., 2 (1999) 3.

113. H. Giefers, M. Nicol, J. Alloys Compd., 442 (2006) 132.

114. M. Armbruster, W. Schnelle, R. Cardoso-Gil, Y. Grin, Chem. Eur. J., 16 (2010) 10357.

115. A. Eftekhari, "Nanostructured Materials in Electrochemistry", Wiley-VCH Verlag GmBH & Co. KGaA (2008).

116. M.N. Obrovac, L. Christensen, Electrochem. Solid-State Lett., 7 (2004) A93.

117. M. Green, E. Fielder, B. Scrosati, M. Wachtler, J.S. Moreno, Electrochem. Solid State Lett., 6 (2003) A75.

118. C.K. Chan, H. Peng, G. Liu, K. Mcilwrath, X.F. Zhang, R.A. Huggins, Y. Cui, Nature Nanotech., 3 (2008) 31.

119. M. Yoshio, H. Wang, K. Fukuda, T. Umeno, N. Dimov, Z. Ogumi, J. Electrochem. Soc., 149 (2002) A1598.

120. J.B. Goodenough, Y. Kim, Chem. Mater., 22 (2010) 587.

121. D. Aurbach, "Nonaquaous Electrochemistry" Marcel Dekker Inc., New York (1999).

122. B.V. Ratnakumar, M.C. Smart, S. Surampudi, J. Power Sources, 97-98 (2001) 137.

123. H.J. Bergveld, W.S. Kruijt, P.H.L. Notten, "Battery Management Systems-Design by Modelling", Philips Research Book series, 1, Kluwer Academic Publishers, Boston (2002).

124. N.J. Dudney, G.A. Nazri, G. Pistoia, "Lithium Batteries" Kluwer Academic Publishers, Norwell, MA (2004).

125. N. Kamaya, K. Homma, Y. Yamakawa, M. Hirayama, R. Kanno, M. Yonemura, T. Kamiyama, Y. Kato, S. Hama, K. Kawamoto, A. Mitsui, Nat. Mater., 10 (20119 682.

126. T. Minami, M. Tatsumisago, M. Wakihara, C. Iwakura, S. Kohjiya, I. Tanaka, "Solid State Ionics for Batteries", Springer-Verlag, Tokyo (2005).

2. PROJECT JUSTIFICATION, OBJECTIVES AND WORK PLAN

2.1. Project justification

The finding of novel electrode materials for high-power and high density lithium ion batteries is one of the most widely investigated topics in Materials Chemistry in the last few decades [1-6]. To this aim, several systems such as lithium transition metal oxides, carbonaceous materials, and alloys have been employed. Among them, lithium alloys and intermetallics attracted early research interest due to their high theoretical capacity [7, 8]. Based on recent research in this field, there is evidence that tin and tin compounds are a hot topic in the present state-of-the-art electrode materials for lithium-ion batteries [9-14].

The basis for this research stems from the very promising result obtained at the Department of Inorganic Chemistry and Chemical Engineering in Cordoba (Spain) under the European Union Erasmus Mundus Grant Scheme for Master of Science (M.Sc) Materials for Energy Storage and Conversion (MESC), in 2008 [15]. Consequently, the Centre National de la Recherche Scientific, CNRS, France in conjunction with ALISTORE-European Research Institute (Alistore-ERI) graciously provided subsequent funding for further research on this topic. The research funding provides the framework for this Doctoral Thesis.

This project has been carried out at the Department of Inorganic Chemistry and Chemical Engineering, University of Cordoba Spain, an ALISTORE-ERI partner institution.

In this Doctoral Thesis, there is further in-depth study of nanoparticulate Sn-based alloys and intermetallics as electrode materials for high energy lithium-ion batteries. Within the main context for Electric Vehicles/Plug-In Hybrid Electric Vehicles (EV/PHEV), Sn or Sn-alloy nano-partices are suitable systems to provide high energy density anodes in lithium-ion batteries. The preparation of new forms of nanodispersed intermetallics is an open way to improve the performance of these materials. Tin intermetallic compounds can be formed by Li-alloying elements and by non Li-alloying elements and have been examined by different authors in lithium test cells [15-22]. Crystallinity and particle size are relevant properties that influence on the electrochemical behaviour of these solids. For Co-Sn intermetallics, it is generally accepted that cobalt might contribute to avoid tin aggregation upon cycling and the

consequent capacity fade. Cobalt is an anomalous fast diffuser in tin and amorphous and crystalline phases are known for the Co-Sn system. Both crystalline Co-Sn compounds and low-crystallinity alloys have been tested as electrode active materials for lithium-ion batteries. The substitution of Co by Fe can be advantageous for toxicity and economic concerns. A precise knowledge of tin-transition metal interactions in the intermetallic electrodes is of fundamental relevance to improve pre-existing materials. Powerful tools used in this task are X-ray diffraction, Electron paramagnetic resonance (EPR) spectroscopy and Mössbauer Spectroscopy.

2.2. Objective

The main scientific <u>objectives</u> are listed below:-

1. Development of preparative routes for nanometric intermetallics based on tin compounds.

2. Improving the capacity and cycling stability of tin-transition metal intermetallics with or without carbon as the negative electrode of Li-ion batteries by nanostructuring.

3. Understanding the effect of particle size on physical and electrochemical properties.

4. Study the mechanisms of the reactions between nanosized intermetallics and lithium.

5. Substitution of Co by Fe in M-Sn alloys.

2.3. Work plan

To achieve these objectives the following main <u>tasks</u> have been carried out:

1. Preparation of intermetallic compounds of MSn_2-type and composites with nanosized particles. Exploration of new synthetic routes and phases. Study of the synthetic pathways. Tailoring of crystallite size and morphology.

2. Physical-Chemical characterization. Elucidating the influence of nanostructuring intermetallic phases, surface properties, thermal and electrochemical behaviour. Establishing the relationships between the size-dependent properties. Effect of the composition (Co/Fe in MSn_2).

3. Electrochemical characterization. Battery applications. Evaluation of the possible use in lithium test cells. Study of the reaction mechanisms.

For each task, the <u>methodology</u> includes:

Task 1:

➢ One-pot method. Polymer: PVP. Chemical reduction with $NaBH_4$ as main reducer. Solvent: Tetraethylene glycol.

➢ Capping nanoparticles. Embedding metallic nanoparticles in a organic matrix.

➢ Sonochemistry.

Task 2:

➢ Structure and morphology. XRD, SEM, HRTEM. ^{57}Fe and ^{119}Sn Mössbauer spectroscopies.

➢ Thermal analysis and stability. DTA.

Task 3:

➢ Lithium test cells. Two-electrode cells. Batteries. Ar-filled dry box. Binder. Electrochemical charge-discharge cycling. Capacity evaluation.

➢ Ex-situ analysis. Post-mortem analysis. Spectroscopic techniques.

REFERENCES

1. M.S. Whittingham, Mater. Sci., 192 (1976) 1226.

2. M. Winter, J.O. Besenhard, M. E. Spahr, P. Nocak, Adv. Mater., 10 (1998) 725.

3. J.M. Tarascon, M. Armand, Nature, 414 (2003) 359.

4. J.L. Tirado, Mater. Sci. Eng., 40 (2003) 103.

5. M. S. Whittingham, Chem. Rev., 104 (2004) 4271.

6. A.S. Arico, P. Bruce, B. Scrosati, J.M. Tarascon, W. Van Schalkwijk, Nat. Mater., 4 (2005) 366.

7. J.O. Besenhard, J. Yamg, M. Winter, J. Power Sources, 68 (1997) 87.

8. R.A. Dunlap, R.A. Small, D.D. McNeil, M.N. Obrovac, J.R. Dahn, J. Alloys Compd., 289 (1999) 135.

9. J. Hassoun, P. Reale, B. Scrosati, J. Mater. Chem. 17 (2007) 3688.

10. X.W. Lou, D. Deng, J.Y. Lee, L.A. Archer, Chem. Mater., 20 (2008) 6562.

11. K.K.D. Ehinon, S. Naille, R. Dedryvere, P.E. Lippens, J.C. Jumas, D. Gonbeau, Chem. Mater., 20 (2008) 5388.

12. Y. Wang, M. Wu, Z. Jiao, J.Y. Lee, Chem. Mater., 21 (2009) 3210

13. Y. Wang, I. Djerdj, B. Smarshy, M. Antonietti, Chem. Mater., 21 (2009) 3202.

14. U.G. Nwokeke, R. Alcántara, J.L. Tirado, R. Stoyanova, M. Yoncheva, E. Zhecheva, Chem. Mater., 22 (2010) 2268.

15. R. Alcántara, U. Nwokeke, I. Rodríguez, J.L. Tirado, Electrochem. Solid-State Lett, 11 (2008) A209.

16. J.J. Zhang, Y.Y. Xia, J. Electrochem. Soc., 153 (2006) A1466.

17. A.D.W. Todd, R.E. Mar, J.R. Dahn, J. Electrochem. Soc., 153 (2006) A1998.

18. M.Z. Xue, Z.W. Fu, Solid State Ionics, 177 (2006) 1501.

19. R. Alcántara, I. Rodríguez, J.L. Tirado, Chem Phys Chem., 9 (2008) 1171

20. H. Guo, H. Zhao, X. Jia, X. Li, W. Qui, Electrochim. Acta, 52 (20079 4853.

21. G.F. Ortiz, R. Alcántara, I. Rodríguez, J.L. Tirado, J. Electroanal. Chem., 605 (2007) 98.

22. R. Alcántara, G.F. Ortiz, Rodríguez, J.L. Tirado, J. Power Sources, 189 (2009) 309.

# 3.   MATERIALS AND METHODS

3.1. Preparation of materials

In this work, various synthetic techniques were applied for the synthesis of Sn-based intermetallics. The solvothermal (polyol) and ultrasonication methods were employed for the synthesis of $Fe_{1-x}Co_xSn_2$ nanocrystals. Alternatively, direct combination method (by heating) was applied for the synthesis of microsized particles.

3.1-1. Synthesis of $Fe_{1-x}Co_xSn_2$ following the polyol method

The polyol method lets to obtain intermetallics at relatively low temperatures, avoiding the extensive grain growth. Considering the MSn_2 stannides, the process that converts β-Sn nanocrystals to M-Sn nanocrystals is a diffusion-based process. As one would predict, temperature plays a primary role in the formation of intermetallic crystals, as well as the ability to retain the morphology of β-Sn nanocrystal templates. Also, the melting point of an element can serve as a rough estimate of its rate of diffusion relative to that of other elements. This is useful for establishing qualitative and empirical guidelines for differences in reactivity among several comparable systems, especially considering the inherent complexity of nanoscale diffusion phenomena [1, 2]. A hypothesized pathway for the synthesis of MSn_2 nanocrystals from cube-shaped β-Sn nanocrystals is shown below. Firstly, there is the formation of Sn nanoparticles by reduction of Sn^{2+} with borohydride in tetraethylene glycol. Tetraethylene glycol is selected because of its high boiling point and reduction power when it is heated.

$$Sn^{2+} \xrightarrow{BH_4^-, TEG} \text{nano-Sn}$$
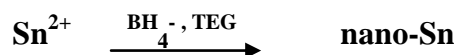
The Sn-nanoparticles are stabilized by the polymer molecules.

Then, the Sn nanoparticles serve as "seeds" to produce intermetallics. There is the diffusion of metals into Sn to form MSn_2 nanoparticles.

$$\text{nano-Sn} \xrightarrow{M^{2+}, BH_4^-, TEG} \text{nano-}MSn_2$$
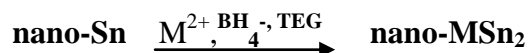
The shape-conserving reactivity and the formation of hollowed-out nanostructures can be rationalized by considering the crystal structure, morphology, and

diffusion characteristics of the β-Sn nanoparticle template. The lattice fringes of the single-crystal β-Sn nanocubes indicate that the (100) crystallographic faces are exposed, consistent with previous reports of β-Sn nanowires [3, 4]. The structure of β-Sn is highly anisotropic: the top and bottom faces have a low density of surface atoms, while the four sides have a much higher atomic density. β-Sn is known to have different diffusion rates along the a- and c- axes as well, with the rate of diffusion along each axis being dependent upon the metal that is diffusing into the β-Sn crystal [5, 6]. Furthermore, because of the higher atomic density of Sn atoms on the four side faces relative to the top and bottom faces, the top and bottom faces are likely to be more reactive in solution than the sides, with the polymer being better able to absorb and stabilize the side faces, helping to inhibit their reactivity [2].

Different metals have varying diffusion rates. Fe and Co belong to the moderately fast (intermediate) melting and diffusing elements. They do not form intermetallics at room temperature, but react with Sn at moderate temperatures (~150°C) to form intermetallics. The difference in the directional diffusion of the metals into Sn can be considered in the so-called Kirkendal effect and influences on the particle morphology. This anisotropic diffusion can produce U-shaped nanoparticles, slabs, nanorods, and fused nanorod dimmers [1, 7].

All the chemicals in the various syntheses were used as received without processing or purification and sourced from reputable and quality makers and suppliers. A summary of the chemicals used and their analytical data are presented in Table 3.1.

Table 3.1. List of reagents used in this work for the synthesis of MSn_2 compounds and composites.

Chemical	Supplier	Properties
Co	Sigma-Aldrich	M=58.93 g/mol CAS: 7440-48-4 Lot.No: S22157-475
Fe	Merck	M=55.845 g/mol 10μm K33244619 502

Sn	Sigma-Aldrich	M=118.69 g/mol CAS: 7440-31-5 d:7.31, < 45μm
Sn	Panreac Química SA	Assay: 99.5%, Pb: 0.07% Lot.715640BP
Tin(II) chloride (SnCl$_2$)	Sigma-Aldrich	M = 189.62 g/mol Assay: min 98% Lot. No.: 71090
Cobalt (II) chloride 6-hydrate (CoCl$_2$.6H$_2$O)	Panreac Química SA	M = 237.93 g/mol Assay: 99.0 – 102.0% Lot. 131257.1209
Tetra ethylene glycol (TEG) O(CH$_2$CH$_2$OCH$_2$CH$_2$OH)$_2$ C$_8$H$_{18}$O$_5$	Sigma-Aldrich	M= 194.23 g/mol Assay: ≥ 99% H$_2$O: ≤ 0.1% Lot: 1048848 21107377
Polyvinylpyrrolidone (PVP) (C$_6$H$_9$NO)$_x$	Sigma-Aldrich	K-Value : 29-32
Poly(2-ethyl-2-oxazoline PEO, (C$_5$H$_9$NO)$_x$	Sigma-Aldrich	Mw = 50, 000 g/mol Tg: 69.0 – 71.0 °C d = 1.14 g/cm^3
Polyacrylonitrile (PAN) (C$_3$H$_3$N)	Sigma-Aldrich	M: 150, 000 g/mol Tg: 85.0°C d: 1.184 g/cm^3 CAS: 25014-41-9
N, N-Dimethylformamide (C$_3$H$_7$NO)	Sigma-Aldrich	M: 73.09 g/mol d: 0.944 g/cm^3 CAS: 68-12-2
Sodium borohydride NaBH$_4$	Panreac Química SA	M = 37.83 g/mol Assay: 99.5%
Ethanol (absolute , QP) CH$_3$CH$_2$OH	Panreac Química SA	M = 46.07 g/mol Min.assay: 99.5%

A photograph of the reaction vessel is shown in Fig. 3.1. This is a "one-pot" method because the preparation is carried out in a single vessel of reaction. The preparation was carried out under flowing argon to avoid the oxidation with air. The temperature was digitally controlled. The resulting powders were separated from the solvent by centrifugation, washed with ethanol and dried under vacuum at 80°C.

Figure 3.1. Photograph of the experimental set-up used for the synthesis of MSn_2 using the "polyol" method.

Powders of $Fe_{1-x}Co_xSn_2$ were obtained by following the polyol method [1, 7-10]. For this purpose, solutions of anhydrous $SnCl_2$, $FeCl_3.6H_2O$, $CoCl_2.6H_2O$ and TEG were prepared. The ratio between the reagents cobalt chloride and iron chloride was

modified in order to obtain the x-value in the nominal composition (x = 0.0, 0.25, 0.3, 0.5, 0.6, and 0.8). Poly (vinyl pyrrolidone) (PVP) and poly (2-ethyl-2-oxazoline) (PEO) were also added to the TEG. The polymers PEO and PVP are used as surface stabilizers and to help the formation of very small metallic particles. $NaBH_4$ dissolved in TEG was used to reduce the ions. Firstly, the tin ions were reduced by adding borohydride solution to the solution containing tin ions and polymers. Then, after stirring for 15 min at 170°C, iron and cobalt ions solution were sequentially added. The solution was then heated to 186°C with continued stirring.

The polyol method described above however, was not successful for the synthesis of nano-$CoSn_2$, as all the attempts yielded nanoparticles of $CoSn_3$ thus highlighting the difficulty arising from a complex temperature-phase relationship in nanocrystal conversion chemistry. Consequently, other synthetic routes were employed for the synthesis of $CoSn_2$ nanoparticles.

3.1-2. Synthesis of $Fe_{1-x}Co_xSn_2$ following the sonochemical method

The ultrasonication method employs the acoustic cavitation effect. The formation, growth and impulsive collapse of bubbles in a liquid, is a vehicle for materials synthesis. During the acoustic cavitation, there is intense heating of the bubbles; generating very high temperatures and pressure in a few microseconds, while bubbles are collapsing and this process creates clean highly reactive surfaces on metals.

The synthesis of several nano$Fe_{1-x}Co_xSn_2$ samples involves the $NaBH_4$ reduction of metal salts in tetraethylene glycol (TEG) using an ultrasonic medium. This was done using a Sonics Vibra-cell Ultrasonic Processor (Model VCX 750); with an operating power of 750 Watts and 20 KHz of frequency. However, for this synthesis, a pre-selected operating power of 35% of nominal power was applied based on the operating regulations. This method does not use the polymers PVP and PEO, and was very successful for the synthesis of $CoSn_2$ nanoparticles, which we could not obtain using the polyol method. A solid-horn was selected to avoid damage of this horn by the surface tension of organic solvents.

A schematic representation of the ultrasound equipment is as presented in Fig. 3.2.
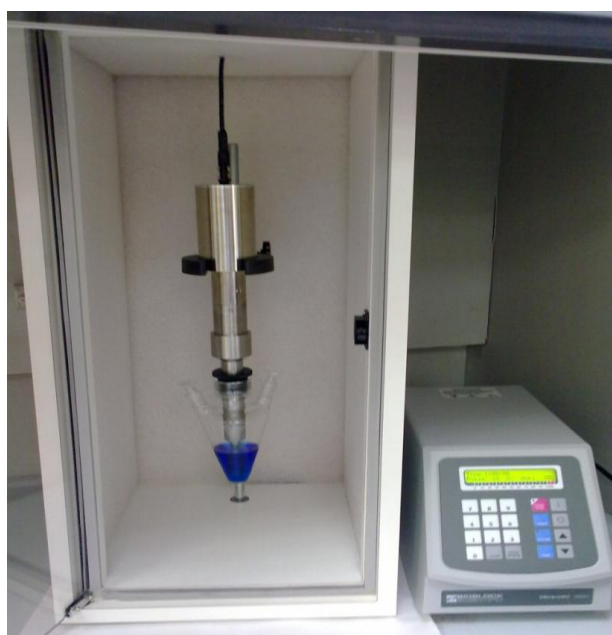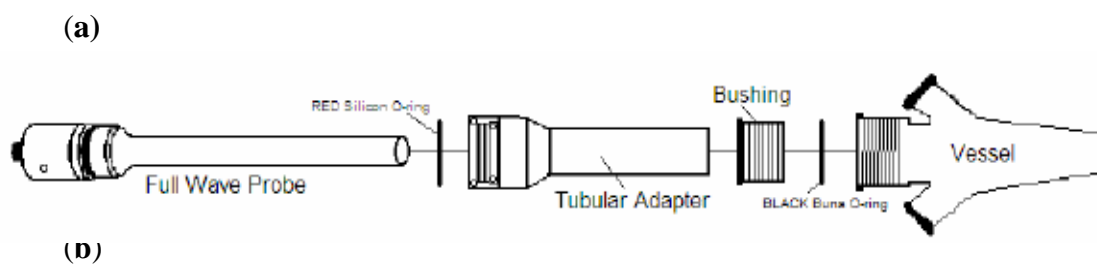
(**a**)

(**b**)

Figure 3.2. (a) The component parts of the Sonics & Materials ultrasonic probe. (b) Photograph of the ultrasonic probe coupled to a 750W ultrasonic processor.

For the synthesis, stoichiometric ratios of anhydrous $SnCl_2$, $FeCl_3.6H_2O$ and $CoCl_3.6H_2O$ were added to TEG and homogenized (dissolved) with the ultrasonic probe for about 15 minutes. Then, $NaBH_4$ dissolved in TEG was added drop-wise into the solution containing tin, iron and cobalt compounds and TEG as a reducing agent. The heat and pressure generated from "acoustic cavitations" by the ultrasonic probe provides

the ideal reaction environment. The resulting metal ions then lead to the formation of $Fe_{1-x}Co_xSn_2$ nanoparticles. In order to allow for intermittent re-distribution of the ions in the reaction medium, the ultrasonic probe is set in a "pulse mode" of 10 minutes operation and 2 seconds standby throughout the duration of the synthesis. Finally, the solution was left for 90 minutes leading to the formation of a black colloidal solution. The resulting powders were separated from the solvent by centrifugation, washed with ethanol and dried under vacuum at 80°C.

3.1-3. Preparation of nano-FeSn$_2$/polyacrylonitrile composites using high-intensity ultrasonication.

Polymers such as polyacrylonitrile (PAN) can be used in solid electrolyte batteries [11]. In addition, it is worth noting that PAN molecules have great ability to interact with metallic surfaces (chemisorption) [12, 13], the Li^+ ions can migrate through the PAN chains by interaction with the CN groups [11] and PAN thin films can be electrical conductors by electron hopping [12]. Having all these in mind, PAN may be used in tin-containing composite electrodes. Thus, tin-transition metal-PAN composites have been explored as electrode materials and the encapsulation of CoSn$_2$ nanoparticles in a PAN matrix has been reported [14-16]. The reduction of Co(II) and Sn(II) with NaBH$_4$ in PAN-dimethylformamide solutions leads to CoSn$_2$ nanoparticles embedded in a PAN matrix (represented as CoSn$_2$@PAN). The addition of PAN hinders the grain growth of the metallic phase, resulting in an improved electrochemical behaviour. In contrast, the reduction of Fe(II) and Sn(II) leads to crystalline Sn [16]. This can be related to the easier Co/Sn alloying. Due to cost and environmental factors, the use of iron instead of cobalt would be advantageous, but it seems to be difficult to achieve good cycling behaviour with cobalt-free tin alloys [17].

The sonochemical method can be used to prepare metallic nanoparticles, such as tin nanorods [18], electrode materials for batteries [19] and to perform coating treatments [20]. In this work, we describe a new strategy for the fabrication of FeSn$_2$ and FeSn$_2$-PAN by using a sonochemical method for the first time.

Nano-FeSn$_2$ was prepared by a combination of polyol and sonochemical methods described earlier. This is here represented as method A. For the preparation of

the FeSn$_2$-PAN composite (method B), SnCl$_2$.2H$_2$O, FeCl$_2$.4H$_2$O and PAN (molecular weight=150.000) were added into n-dimethylformamide (DMF) and ultrasound irradiation was applied. PAN is soluble in DMF and insoluble in water. Then, an aqueous solution of NaBH$_4$ was added while the ultrasound irradiation was continuously applied. Alternatively, the same synthesis procedure was applied except that no ultrasonication was applied (method C) as it was previously reported [16]. An iron-free tin-PAN composite sample was also prepared by using method C [9]. The carbon-nitrogen analysis was carried out using an elemental analyzer Eurovector 3000.

3.1-4. Synthesis of Fe$_{1-x}$Co$_x$Sn$_2$ following the ceramic method

For the preparation of larger particles of crystalline intermetallics, powders of Fe$_{1-x}$Co$_x$Sn$_2$ were obtained at high temperature. In its simplest form, the ceramic method consists of heating together two solids which react to form the required product and used widely both industrially and in the laboratory [21]. In this work, appropriate amounts of Sn, Co, and Fe powders were heated in an HOBERSAL tubular furnace (T$_{max}$ = 1200°C) at 490°C for around 12-15 h under Ar flow. A quartz tube was used to flow the Ar. The high temperature direct synthesis of micrometric powders is illustrated below:

$$\textbf{M} + \textbf{2Sn} \xrightarrow{\textbf{~500°C}} \text{micro-}\textbf{MSn}_2 \qquad (\textbf{M= Fe, Co})$$

After heating to the required temperature and time, they were allowed to gradually cool down to room temperature. The resulting products were then gently ground manually in agate mortar.

3.2.   Instrumentation

In this project, various analytical techniques were employed for in-depth study of materials. The most outstanding techniques are highlighted below under physico-chemical, thermal and electrochemical techniques:

3.2-1. X-Ray Diffraction

In order to explore the structure of crystals we require waves which interact with atoms and which have a wavelength comparable with the interatomic spacing in crystals; that is, we require a wavelength of the order of 1Å (= 10^{-8} cm). The interaction should be weak enough so that the wave can penetrate in a coherent fashion into the crystal for a distance of the order of perhaps 1000 lattice constants [22]. X-rays are a form of electromagnetic radiation that have high energies and short wavelengths-wavelengths on the order of atomic spacings for solids [23], thus making X-rays the correct order of magnitude for diffraction of atoms of crystalline materials. The X-Ray diffraction (XRD) technique is therefore one of the most important analytical techniques employed in Solid State Chemistry. Diffraction techniques exploit the scattering of radiation from large number of sites; from atoms, groups of atoms and molecules, mainly in crystals (structures that have long-range order).

The condition for diffraction was discovered by William H. Bragg and W. Lawrence Bragg and is known as the Bragg Law:

$$2d_{hkl}Sin\Theta = n\lambda \qquad (3.1)$$

where,

λ = wavelength of the x-ray, Θ = scattering angle, n = integer representing the order of the diffraction peak, and d = inter-plane distance

Powder diffractometers come in two basic varieties: θ-θ in which the X-ray tube and the detector move simultaneously or a θ-2θ in which the X-ray tube is fixed, and the specimen move at ½ the rate of the detector to maintain the θ-2θ geometry. The angle of the diffraction (recorded as 2θ by convention) is related to the interplanar spacing, d_{hkl}, by the Bragg law, and the intensity of the diffraction maximum is related to the strength of those diffractions in the specimen. The angles and intensities of diffraction are recorded electronically resulting in a plot of Intensity (vertical axis) vs. 2θ (horizontal axis) for the specimen.

By the right choice of metal anode and energy of accelerated electrons, a known wavelength (i.e., energy) or group of wavelengths will dominate the X-rays generated. Copper (Cu) X-ray tubes are the most commonly used for X-ray diffraction of inorganic

materials, with the wavelength of the strongest Cu radiation (Kα) approximately 1.54 angstroms (Å). Other anodes commonly used in X-ray generating tubes include Cr (Kα, 2.29Å), Fe (Kα, 1.94Å), Co (Kα, 1.79Å), and Mo (Kα, 0.71Å) [24].

For structural refinement and determining the cell lattice parameters, the Cellref programme and the Rietveld method (Fullprof programme) were used.

In this thesis, XRD diagrams were recorded on a Siemens D5000 instrument with θ-2θ geometry. Cu$_{k\alpha}$ radiation and 8s - 0.04°/2Θ steps were used. The average crystallite size or coherently diffracting domain was calculated using the Scherrer equation shown below:

$$Lc = 0.9\,\lambda\,/\,\beta\,cos\,\Theta \qquad\qquad (3.2)$$

where β = line breadth of the Bragg peak centered at Θ

A commercial LaB_6 product was used as a standard reference material for line width correction. For recording ex-situ XRD diagrams of the lithiated electrodes, the electrochemical cells were disassembled in a dry box, the electrode material supported on a copper foil was placed in the XRD sample holder and then covered with a protective plastic film to avoid the reaction with air during the XRD scan.

3.2-2. Mössbauer Spectroscopy

The Mössbauer effect was first discovered by the Nobel laureate Rudolph Mössbauer in 1957. Today, the Mössbauer spectroscopy is a versatile technique that can be used to provide information in many areas of Science such as Physics, Chemistry, Biology and Metallurgy. The Mössbauer effect involves resonant absorption of gamma (γ) rays by atoms of the same isotope. If a free atom or molecule with mass, m, emits or absorbs a gamma quantum of energy, E_γ, a linear momentum with recoil energy, E_R is imparted to the atom and molecule respectively and is given by the following equation;

$$E_R = E_\gamma^2 \,/\, 2mc^2 \qquad\qquad (3.3)$$

As a result of the recoil energy, resonant absorption is prevented. If however, the atom is bonded to other atoms (say, in a crystal), then its effective mass is increased by a large factor, reducing the energy it absorbs from the gamma rays, i.e. the atom is now so massive it doesn't recoil. In these conditions, it is possible to achieve resonant absorption by modulating the energy of the gamma ray beam, by oscillating the gamma ray source with the resulting Doppler shift changing the energy of the photons. When the modulated beam matches the difference in energy between the ground and first excited state of the absorber (i.e. at resonance) then the gamma rays are resonantly absorbed. This gives a reduction in the number of counts at the detector giving an output which shows a very simple spectrum for an emitter and absorber in the same surroundings [25].

The output of the Mössbauer spectrum can be affected by temperature and three other factors:

1. Isomer shift:

The isomer shift results from the difference in the electron density at the nuclear sites in the emitting and absorbing atoms leading to the shifting of the spectrum.

The energetic variation between the ground and excited state is given by the expression:

$$\Delta E = \frac{1}{6\varepsilon_0} Ze^2 \left(\left\langle R^2 \right\rangle_{excited} - \left\langle R^2 \right\rangle_{ground} \right) |\Psi_0|^2 \qquad (3.4)$$

where: Ψ_0 is the electronic density at the nucleus
R is the nuclear radius
Z is the atomic number
e is the electron charge

This energy variation applies both to the source and the absorber material. If the energy is the same, there is no observed shift but if the energy is not the same, there is a shift which corresponds to the chemical shift. It is represented as:

$$\delta_{cs} = \Delta E_{abs} - \Delta E_{sour} = S(Z) \frac{Ze^2 R^2}{5\varepsilon_0} \frac{\Delta R}{R} \left(|\Psi_0|^2_{abs} - |\Psi_0|^2_{sour} \right) \qquad (3.5)$$

where S(Z) is the relativistic correction factor.

However, instead of recording the spectrum of the source, we record the spectrum of an external source reference. Therefore, the chemical shift is finally represented as:

$$\delta_{cs} = \Delta E_{abs} - \Delta E_{sour} = S(Z)\frac{Ze^2R^2}{5\varepsilon_0}\frac{\Delta R}{R}\left(|\Psi_0|^2_{abs} - |\Psi_0|^2_{ref}\right) \qquad (3.6)$$

There are various factors affecting the electron density of the nucleus of the absorber, and hence the isomer shift. They include:

- Effect of orbital penetration: the main contribution arises from the s-orbitals. ($1s$ > $2s$ > $3s$). Also, orbitals p and d have low penetration and exert mainly shielding effect.
- Core/Valence electrons: the main contribution arises from valence shell electrons. The contribution of core electrons is almost unaffected by valence shell electrons.
- If the number of s electrons increases, then electronic density increases.
- If the number of p and d electrons increases, then the isomer shift decreases.

This isomer shift effect is exemplified by Sn and Fe compounds (studied in this thesis). Fig.3.3 shows the effect of s, p, and d electrons on the isomer shift of Sn compounds. Considering the electronic configuration of Sn^{2+} ([Kr] $4d^{10}$ $5s^2$), Sn^0 ([Kr] $4d^{10}$ $5s^2$ $5p^2$, and Sn^{4+} ([Kr] $4d^{10}$), the highest increase in isomer shift is witnessed for Sn^{2+} due to the presence of the s electrons, followed by Sn^0 due to the shielding effect of the p electrons (even though it has the same number of s electrons with Sn^{2+}), while the least effect is seen for Sn^{4+} due to the absence of s and p electrons.
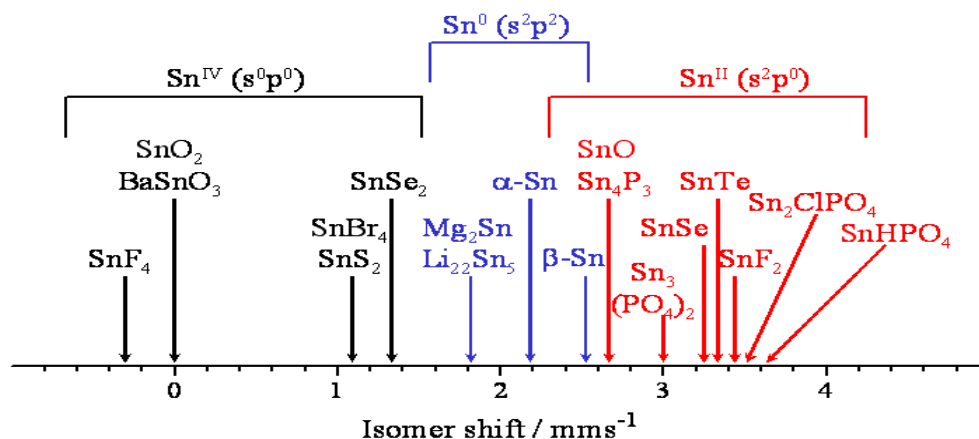
Figure 3.3. The effect of oxidation state on the isomer shift of Sn compounds.

In the case of Fe compounds, the following observations are made: (Fig.3.4)

- There is the decrease of isomer shift with increasing oxidation state. This is because the ratio $\Delta R/R$ (eqn. 3.5) for Fe is negative.

- Decrease of the isomer shift decreasing ligand electronegativity (for a given iron oxidation state and coordination)

- Decrease of isomer shift with decreasing coordination (for a given oxidation state and ligand).
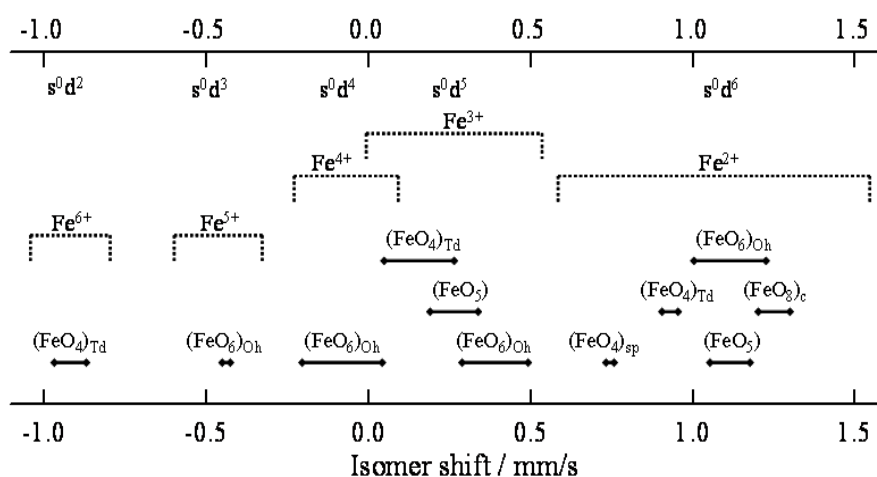
Figure 3.4. The effect of oxidation state, ligand electronegativity and coordination on the isomer shift of Fe compounds.

75

2. Quadrupole splitting:

When the nuclei under investigation do not have a charge distribution that is spherically symmetric, it leads to an electric nuclear quadrupole moment which interacts with an asymmetric electronic charge distribution to give splitting of the nuclear energy levels. Therefore, quadrupole splitting results from the interaction between the electronic field gradient (EFG) at the nucleus and the electric quadrupole moment of the nucleus itself.

The quadrupole moment is present when the nuclear spin is greater than ½. Assuming all the Mossbauer-active nuclei have nuclear spin > ½ (ground, excited state, or both), all the nuclei are susceptible to quadrupolar splitting. The energetic difference between the sublevels characterized by a given value of $Im_I I$ is:

$$\Delta EQ = \frac{eqeQ}{4} = \frac{3m_I^2 - I(I+1)}{I(2I-1)} \left(1 + \eta^2/3 \right)^{1/2} \tag{3.7}$$

where,

$$eq = \left(\frac{\partial^2 V}{\partial z^2} \right)_0 \qquad = \text{Principal component of the EFG}$$

$$\eta = \left[\left(\frac{\partial^2 V}{\partial x^2} \right)_0 - \left(\frac{\partial^2 V}{\partial y^2} \right)_0 \right] \Big/ \left(\frac{\partial^2 V}{\partial z^2} \right)_0 \qquad = \text{Asymmetry parameter of the EFG}$$

$$eQ = \frac{3}{2} Q_{33} \frac{2I-1}{I+1} \qquad = \text{Electric quadrupole moment}$$

The splitting of the nuclear energy levels (e.g. Fe and Sn) is show in Fig. 3.5.

The asymmetry parameter (non-uniformity in the quadrupole splitting) is known as the Goldanskii-Karyagin effect. This effect increases with increasing temperature but does not depend on the orientation. There is also the texture effect which is independent of the temperature but varies with the orientation of the sample. However, the texture effect disappears by recording at the magic angle of $\Theta = 54.74°$.

Example: case of ^{57}Fe and ^{119}Sn:
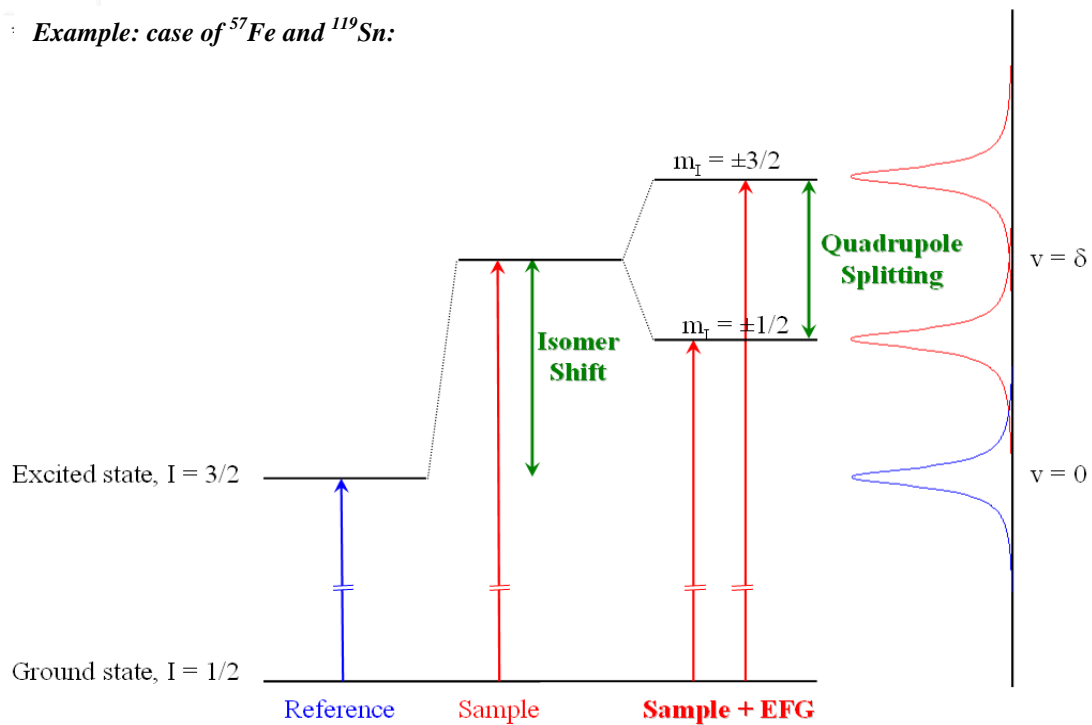
Figure 3.5. Quadrupole splitting arising from the interaction of the nuclear electric field gradient (EFG) and its electric quadrupole moment.

3. Magnetic splitting:

When placed in a magnetic field a nucleus with a magnetic moment has a dipole interaction with the field. The interaction of the nuclear magnetic moment μ associated to the nuclear spin with a magnetic field H (internal or external), raises the degeneracy of nuclear states with angular momentum quantum number I>0 to 2I+1 and the splitting is directly proportional to the magnetic field applied. For a nuclear spin of I = ½ and 3/2 (which is the case of ^{57}Fe and ^{119}Sn) corresponding to the ground and excited states (Fig. 3.6), there are two sets of splitting as shown below:

I = 1/2   two sublevels: $m_I = + 1/2, - 1/2$

I = 3/2   four sublevels: $m_I = + 3/2, + 1/2, - 1/2, - 3/2$

The splitting shown in Fig. 3.6 is the case for [57]Fe. In the case of [119]Sn, sometimes we observe the 7th and 8th component splits as a result of a residual magnetic interaction arising from the superparamagnetic Sn nanoparticles. The energetic variation, ΔE_m, different for each I value, is given by the expression below:

$$\Delta E_m = -\frac{\mu H m_I}{I}$$

(3.8)
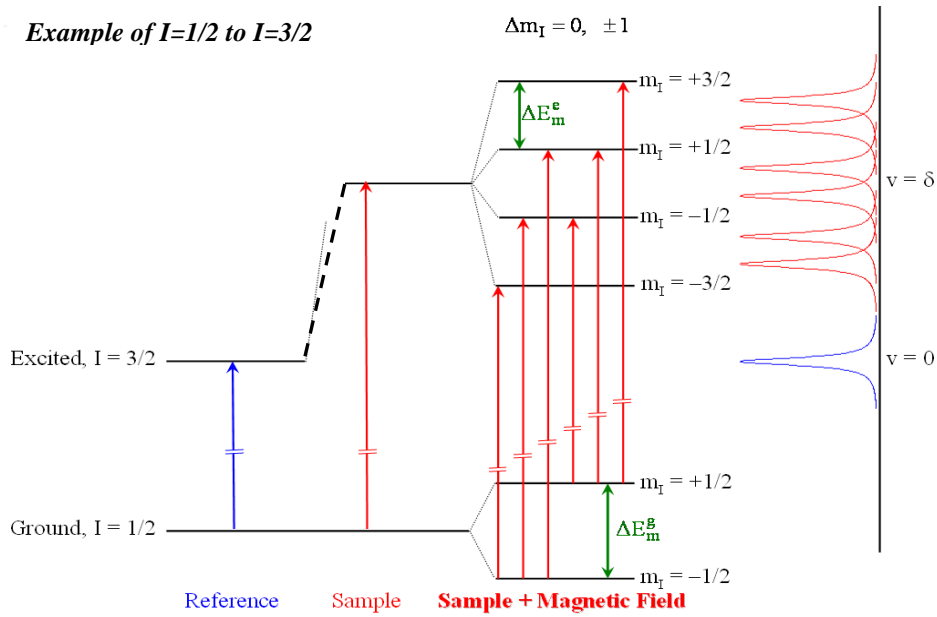
Figure 3.6. Magnetic splitting arising from the interaction of the nuclear magnetic moment,μ associated to the nuclear spin with the magnetic field, *H*.

The Mössbauer effect has been observed in ~ 100 nuclear transition, ~ 80 isotopes and 43 elements including [57]Fe , [61]Ni, [67]Zn, [119]Sn, [121]Sb, [125]Te, etc [25, 26].

In this work, [119]Sn and [57]Fe Mössbauer spectra were recorded in transmission mode at room temperature by using a Wissel instrument. Ba[119]SnO$_3$ (δ = 0.0 mm s^{-1}) and [57]Co in a Rh matrix were used as radioactive sources, respectively. The [119]Sn isomer shifts were referenced to BaSnO$_3$ and pure β-Sn foils was used for the

instrument calibration. A pure α-Fe foil was used for calibration and as reference in the ^{57}Fe Mössbauer Spectra. For the fitting of the experimental spectra, Lorentzian profiles and a least-square method were employed. The fit quality was controlled by the χ^2-test. For Mössbauer measurements, used electrodes were kept inside a thermo-sealed bag (Aldrich) inside the drybox, and the bag was directly transferred to the Mössbauer spectroscopy instrument.

### 3.2-3.	Electron Microscopy

Electron microscopes are scientific instruments that use a beam of energetic electrons to examine objects on a very fine scale and were developed due to the limitations of light microscopes. The interaction of electrons with materials result to different signals which when captured with adequate detectors, reveal information about their nature. They are advantageous in that a high degree of magnification as well as an excellent depth of focus can be achieved.

### 3.2-4.	Scanning Electron Microscopy (SEM)

The scanning electron microscopy (SEM) is based on the study of secondary and backscattered electrons emitted by a specimen when impinged on by electrons. The secondary electrons can be described as those electrons which escape from the specimen with energies below about 50 eV. They could conceivably be primary electrons which at the end of their trajectory reach the surface with a few remaining eV or more likely electrons to which a small amount of energy has been transferred by scattering or excitation within a short distance of the surface. On the other hand, some primary electrons may leave the surface before giving up all their energy and are most likely to do this while they still have a large fraction of their incident energy. These are the backscattered electrons and are not usually as numerous as secondary electrons.

The electron source (or gun) is usually of the tungsten filament thermionic emission type. The fine beam of electrons is scanned across the specimen, while a detector counts the number of low energy secondary electrons, or other radiation, given off from each point on the surface. At the same time, the spot of a cathode ray tube is

scanned across the screen and sent to a television screen for recording [27]. The principal application of SEM is to study the morphology of specimens with the advantage of obtaining three dimensional effects as a result of its high depth of focus of up to 1000Å.

The SEM images were recorded on a JEOL SM6300 at the University of Cordoba *Servicios Centrales de Apoyo a la Investigacíon* (SCAI) microscopy facility. This microscopy uses a fine beam of electrons, within a 10 nm diameter, 5 to 50 KeV of energy and scans specimens in parallel lines throughout the surface rapidly. The samples were prepared on black adhesive film on a copper sample holder surface.

3.2-5. Energy Dispersive Spectroscopy (EDS)

The energy dispersive X-ray spectroscopy (EDS) is an analytical technique that qualitatively and quantitatively identifies the elemental composition of materials analyzed in SEM. When the electron beam of the SEM is scanned across a sample, it generates X-rays from the atoms in the top 2 microns. The energy of each X-ray is characteristic of the atom from which it escaped and is detected by a semiconductor, processed by a detector protected by an ultrathin window and cooled at liquid nitrogen temperature to avoid the thermal noise and the diffusion of the dopant in the semiconductor. The EDS system collects the X-rays, sorts them by energy and displays the number of X-rays versus their energy.

An EDS spectrum is constituted by a background produced by the Bremsstrahlung (continuum) X-rays and by peaks characteristic to the chemical elements of the material, and displays the distribution of elements as either dot maps or line profiles with a spatial resolution of 1 micron.

In general, EDS is used in material composition verification, alloy and intermetallic identification and their relative proportions, contaminant location and identification, elemental diffusion profiles, and multiple spot analyses of areas from 1 micron to 10 cm. However, the elements identified are limited to those heavier than beryllium [28].

The EDS analyses were also measured on the SEM apparatus described above.

3.2-6. Transmission Electron Microscopy (TEM)

This is a microscopy technique whereby a beam of electrons is transmitted through an ultra thin specimen, interacting with the specimen as it passes through. The most common types of TEM have thermionic guns capable of accelerating the electrons through a selected potential difference in the range 40-200 KV [28-31]. Therefore, for TEM observations, thin samples are required due to the important absorption of the electrons in the material. An image is formed from the electrons transmitted through the specimen, magnified and focused by an objective lens and appears on an imaging screen, or to be detected by a sensor such as a CCD camera (Fig.3.7).
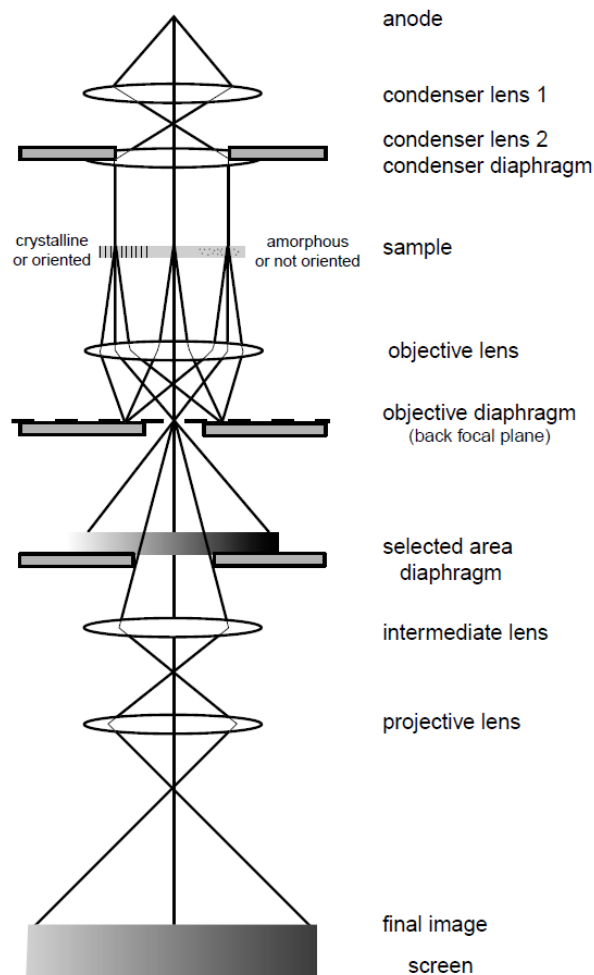
Figure 3.7. Ray diagram for a transmission electron microscope in image mode [31].

The TEM provides information about the internal structure of the specimens, and allows the direct observation of crystal structure and can also determine types and positions of defects in samples.

High Resolution Transmission electron microscopy (HRTEM) images of the intermetallic particles were recorded on a JEM-2010 apparatus at the University of Cordoba *Servicios Centrales de Apoyo a la Investigacíon* (SCAI) microscopy facility. For this purpose, the sample was dispersed in acetone by using ultrasonication, and a drop of the resulting dispersion was deposited on a formvard grid.

3.2-7. Electron Paramagnetic Resonance (EPR) Spectroscopy

Electron paramagnetic resonance (EPR) was discovered in 1944 by Evgeniy K. Zavoyskiy. It is a sensitive spectroscopic method for the determination of the geometric and electronic structure, the dynamics and the spatial distribution of paramagnetic species in materials. It directly focuses on the unpaired electrons and nuclei in their vicinity and is therefore the method of choice for studying free radicals, triplet states, compounds with transition metal and rare earth ions and defect centres. It is a particularly useful technique for analysing orientationally disordered systems such as powders or frozen solutions where standard diffraction methods fail [26, 32-35].

The phenomenon of electron spin (electron paramagnetic) resonance spectroscopy can be explained by considering the behaviour of a free electron [36, 37]. According to quantum theory the electron has a spin which can be understood as an angular momentum leading to a magnetic moment. Consequently, the negative charge that the electron carries is also spinning and constitutes a circulating electric current. The circulating current induces a magnetic moment μs which, if the electron is subjected to a steady magnetic field $H_0 \parallel z$, causes the electron to experience a torque tending to align the magnetic moment with the field. The relation between the moment and the spin vector is

$$\mu s = -g\mu_B/\hbar *S \tag{3.9}$$

where μ_B is the Bohr magnetron and g is the Landé factor (or spectroscopic splitting factor, equal to 2.0023 for a free electron). The g factor is very important in EPR

measurements since unpaired electrons in different environments have slightly different g factors, resulting in the appearance of signals for different centres at different magnetic field strengths. For an unknown signal, the g factor (g_2) is determined using a standard signal with a known g factor (g_1) at their corresponding H values, (H_{02} and H_{01}) respectively using the following relation;

$$g_1 H_{01} = g_2 H_{02} = h\nu/B, \quad \Rightarrow g_2 = g_1 (1 - \Delta H/H_{01}) \tag{3.10}$$

The absorption of electromagnetic radiation at the resonance frequency $\nu = \Delta E/h$ induces transitions from the low energy level to the higher energy level. (The numerical value equation is $\nu = 2.8026 * 10^{10} * B_0 \text{Hz/T}$, i.e. for a magnetic field of about 0.35T the resonance frequency lies in the so-called X-band between 9 and 10 GHz). The energy of the system depends upon the projection of the spin vector along H_0. Quantum theory stipulates that only two values are permitted for an electron $S_z = \pm\hbar/2$, which means that the electron magnetic moment can only assume two projections onto the applied field. Consequently,

$$\mu_z = \pm\frac{1}{2}g\mu_B \tag{3.11}$$

and the ensemble of energy levels therefore reduce to the two values

$$E\pm = \pm\frac{1}{2}g\mu_B H_0 \tag{3.12}$$

If electromagnetic radiation is applied at a frequency that corresponds to the separation between the permitted energies equal to $\Delta E = E_+ - E_- = g\mu_B H_0 = \hbar\omega$, energy is absorbed from the electromagnetic field.

For electrons bound into an atom or a molecule, the phenomenon of EPR may not be observed at all, because electron spins pair off in atomic or molecular orbitals so that virtually no net spin magnetism is exhibited and the material is said to be diamagnetic. When an atom or molecule has an odd number of electrons, however, complete pairing is clearly not possible and the material is said to be paramagnetic. In

that case, EPR can be observed. In EPR measurements, the source of radiation (microwaves) in radiospectrometer is a klystron which represents a radiolamp giving monochrome radiation in the cm-wave band. The signal represents the first-order derivative of absorption line as shown in Fig.3.8.
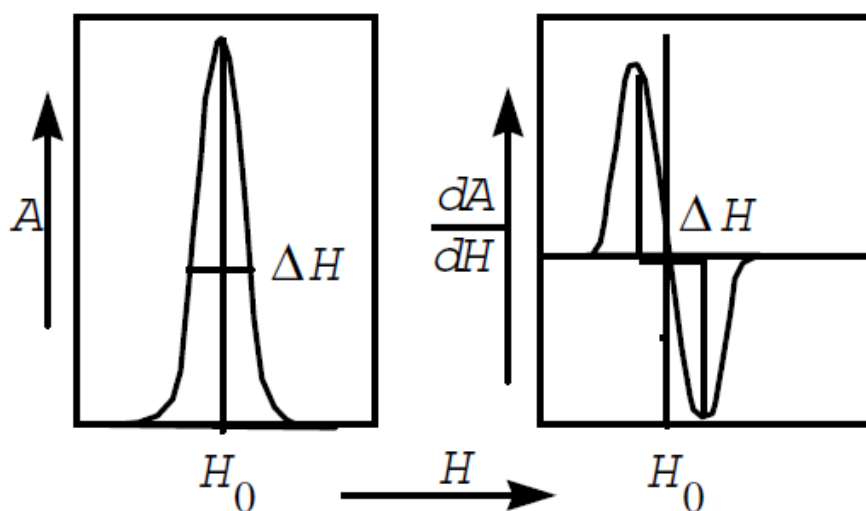
Figure 3.8. A schematic representation of an EPR signal.

The area under the line of absorption is proportional to the concentration of paramagnetic particles in the sample. Thus, the concentration of paramagnetic centres is proportional to the first integral under the line of absorption or to the second integral of EPR spectra.

In general, the following parameters can be determined from EPR spectroscopy;

- the electronic state of the material under study (electron Zeeman interaction)

- the coupling between unpaired electrons (fine structure term)

- interactions between the unpaired electron and the nuclei (hyperfine couplings)

- type of nuclei in the vicinity of the unpaired electron (nuclear Zeeman interaction)

- the electric field gradient caused by the electrostatic charges (nuclear quadrupole interactions) [32].

EPR spectra were registered at X-band (9.23 GHz) as the first derivative of the absorption signal using ERS 220/Q spectrometer in the temperature range 90-410 K. The g-factors were established with respect to a Mn^{2+}/ZnS standard. The signal intensity was determined by double integration of the experimental EPR spectrum. The EPR measurements were done at the Institute of General and Inorganic Chemistry, Bulgarian Academy of Sciences. For EPR measurements of anode materials, the samples were manipulated in a glove box in Ar atmosphere. All EPR measurements on dry electrode compositions (without electrolyte) were carried out in quartz tubes in an Ar atmosphere.

3.2-8.   Differential Thermal Analysis (DTA)

Differential thermal analysis (DTA) involves heating or cooling a test sample and an inert reference under identical conditions while recording any temperature difference between the sample and the reference. The reference material is any substance with about the same mass as the sample, which undergoes no transformations in the temperature range of interest. The temperature difference between the sample and reference is measured by a "differential" thermocouple in which one junction is in contact with the underside of the sample crucible, and the other is in contact with the underside of the reference crucible. In a DTA classical configuration, thermocouples are in the sample and reference material. Therefore the signal is:

$$\Delta T = R \frac{dT}{dt} \left(C_s - C_r \right)$$

(3.13)

where, Ts = actual sample temperature

R = thermal resistance

C_s = heat capacity of sample

C_r = heat capacity of reference

When the sample undergoes transformation, it will either absorb (endothermic) or release (exothermic) heat. DTA is used to study thermal properties and phase changes which lead to a change in enthalpy; and as a finger print for identification purposes, for example, where the structural similarity of different forms renders diffraction experiments difficult to interpret [38-40].

Differential thermal analysis (DTA) experiments were performed in a Shimadzu DTG-60 instrument, using alumina pans and a heating rate of 10ºC/min. A continuous Ar-flow of 70 mL/min was used as purging gas and to create an inert atmosphere. To remove the air, the Ar-flow was initiated 50 minutes prior to starting the DTA measurement. The employed Ar had 2 ppm of O_2 and 2 ppm of H_2O impurities. The continuous flow of Ar was electronically controlled with a Bronkhorst apparatus.

3.3. Electrochemical Analysis

Batteries are electrochemical devices which convert chemical energy into electrical energy by electrochemical oxidation and reduction reactions, which occur at the electrodes. A cell consists of an anode where oxidation takes place and a cathode where oxidation takes place, and an electrolyte which conducts the electrons (via ions) within the cell [41].

3.3-1. Cell potential, mechanism and driving force for lithium intercalation

In generalized terms, the reaction at one electrode (reduction in forward direction) can be represented by

$$aA + ne \rightleftharpoons cC \qquad\qquad (3.14)$$

where a molecules of A take n electrons e to form c molecules of C. At the other electrode, the reaction (oxidation in forward reaction) can be represented by

$$bB - ne \rightleftharpoons dD \qquad\qquad (3.15)$$

The overall reaction in the cell is given by addition of these two half reactions

$$aA + bB \rightleftharpoons cC + dD \qquad (3.16)$$
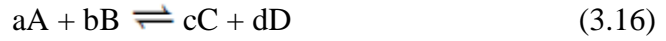
The change in the standard free energy, ΔG^0 of this reaction is expressed as

$$\Delta G^0 = -nFE^0 \qquad (3.17)$$

where F = the Faraday´s constant (96, 487 coulombs)

E^0 = the standard electromotive force.

The change in the standard free energy ΔG^0 of a cell reaction is the driving force which enables a battery to deliver electrical energy to an external circuit [41-44].

However, when conditions are other than the standard state, the voltage E of a cell is given by the Nernst equation

$$(3.18)$$

$$E = E^0 - \frac{RT}{nF} \ln \frac{a_C^c a_D^d}{a_A^a a_B^b}$$

where a is the activity of relevant species

R = gas constant

T = absolute temperature

Consider the total cell reaction:

$$Li_xCoO_2 + Li_yC_6 \qquad \rightleftharpoons \qquad Li_{x+\delta}CoO_2 + Li_{y-\delta}C_6$$
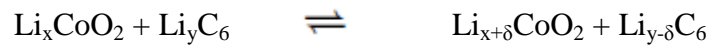
The thermodynamic quantity describing the change in energy as a function of changes in lithium concentration in the host matrix is the chemical potential (μ), defined as:

$$(3.19)$$

$$\mu = \frac{\partial G}{\partial x}$$

where G is the Gibbs free energy, and x is the number of inserted lithium ions.

By combining the equations above, we get the relation between electrical and chemical energy in the system:

$$-nFE = \mu_c - \mu_a \qquad (3.20)$$

where μ_c and μ_a are the chemical potentials of the lithium ions in the cathode and anode respectively. In an electrochemical cell, these oxidation-reduction reactions occur simultaneously but spatially separated.

It would be desirable if during cell discharge, all of the energy could be converted to useful electric energy. However, losses due to polarization occur when a load current, *i,* pass through the electrodes accompanying the electrochemical reactions. These losses include activation polarization, which drives the electrochemical reaction at the electrode surface, and concentration polarization, which arises from the concentration differences of the reactants and products at the electrode surface and in the bulk as a result of mass transfer. The polarization effect consumes part of the energy, which is given off as waste heat, and thus not all of the theoretically available energy stored in electrodes is fully converted into useful electrical energy. Another important factor that strongly affects the performance or rate capability of a cell is the internal impedance of the cell. This causes a voltage drop during operation and consumes part of the energy. The voltage drop due to internal impedance is usually referred to as "ohmic polarization" or IR drop and is proportional to the current drawn from the system [41].

Therefore the actual cell voltage is the difference between the thermodynamic voltage and all the voltage losses, and expressed as follows:

$$\Delta E_{observed} = \Delta E_{thermodynamic} - \Delta E_{polarization} \qquad (3.21)$$

3.3-2. Electrochemical measurements

Several electrochemical methods have been developed by which information about insertion-reaction electroactive components can be obtained [41]. The voltage-composition relation can be determined either in a current controlled mode or in a potential controlled mode.

The Galvanostatic Cycling with Potential Limitation (GCPL) is the most used standard technique for studying the behaviour of batteries upon cycling. The electrodes studied in this project have been electrochemically cycled by this method. In this electrochemical method, the performance of a battery is determined as a function of its charge and discharge conditions: a given rate within a given potential range mainly. The galvanostatic rate of a battery is usually expressed in C/h; C being the nominal charge of the battery (both positive and negative electrode), and h being the number of hours at which this nominal charge will be passed through [45]. In general, C corresponds to the total expected reduction/oxidation of the electrode, i.e. the insertion/extraction of one lithium in *h* hours (normally between 5-10 h).

Generally, the quantity of total electric charge, Q applied for a charge-discharge process is derived from the Faraday´s law

$$Q = It/ \text{Equiv.} = F \qquad\qquad (3.22)$$

where, I = current (Amperes), t = time (S), Equiv. = (M/z), M = molar mass (g/mol), and z = the valency number of ions of the substance (electrons transferred per ion), and F = Faraday´s constant (96480 C/mol; 1C = 1As).

3.3-3. Battery assembly and cycling

For battery assembly, a 2-electrode Swagelok$^®$ type cells were used. The Swagelok$^®$ cell is made of a perfluoroalkoxy (PFA) copolymer body and stainless steel electrode collector. One half part of the cell is used for the working electrode while the counter electrode is lithium metal foil. In the case of electrodes prepared for electrochemical impedance studies, a 3-electrode Swagelok$^®$ type cells were used with the third electrode (also a lithium metal foil) used as the reference (Fig. 3.9).

For the anode materials studied, the electrodes are composed of a mixture of 77% active material, 15% of graphite (to improve electrical contact between the particles) and 8% polyvinylidene fluoride (PVDF) as binder (to improve mechanical resistance). The mixture of $Fe_{1-x}Co_xSn_2$ powder, carbon and PVDF was firstly

homogenized by grinding in an agate mortar. Secondly, the slurry was made with some drops of N-methylpyrrolidone (NMP) that was then evaporated at 120°C for some hours under vacuum. To prepare the electrode, a high-purity copper foil (Goodfellow; 99.99%) was used as the support base and conducting media for the electrode. Circular pieces were cut from the copper foil, pressed to about 4-5 Tons/cm^2 in a SPECAC pressing device and then weighed. The slurry was deposited on the copper and then dried under vacuum. After drying, the electrodes are then pressed to about 2 Tons/cm^2. They are then weighed again to determine the actual weight of the active material.

The electrodes are coupled for cycling inside an M-Braun LabMaster 139 glove box with an argon atmosphere equipped with an oxygen analyzer to monitor oxygen levels (normally less than 2 ppm is necessary to avoid materials contamination). To ensure the flow of ions in-between the two ends of the electrode, an electrolyte is used. In this work, we have used a solution of 1M LiFP$_6$ dissolved in Ethylene Carbonate/Diethyl Carbonate (EC: DC, 1/1 v/v) supplied by Merck. Few drops of the electrolyte are added on the separator; a Whatman GF/A glass microfibre filter, which ensures the flow of ions between the two electrodes.
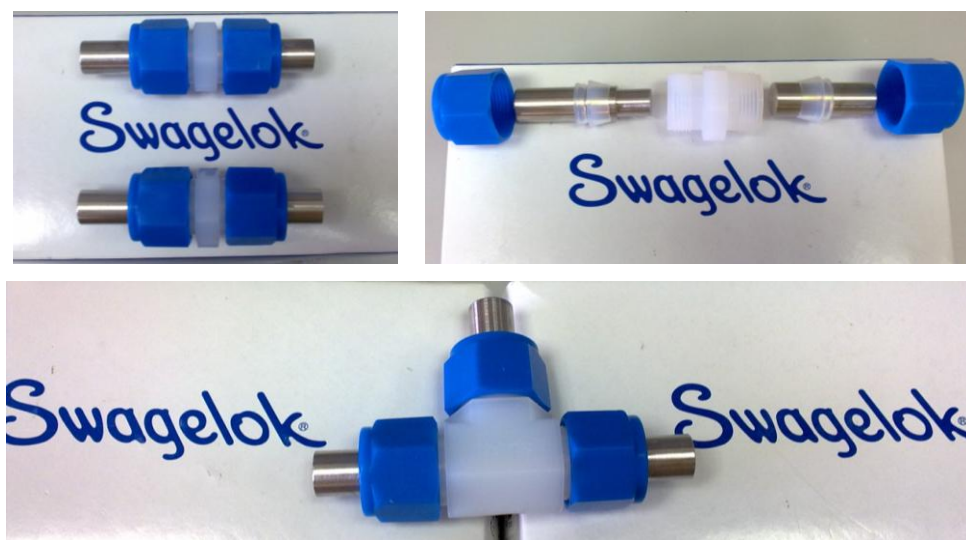
Figure 3.9. Typical Swagelok® (2-electrode and 3-electrode) cells used for battery cycling.

The electrochemical analyses were performed on a Biologic multi-channel "MacPile-II" system (VMP) and a multi-channel battery testing system-BT 2000 from Arbin Instruments.

3.3-4. Battery discharge-charge terms

There are various terms used to describe the performance of batteries. They include:

- Capacity:

This is the electrical charge effectively stored in a primary or secondary battery and available for transfer during discharge. It is usually expressed in ampere-hours (Ah) or milliampere hours (mAh). Specific capacity is given in mAh/g units.

- Theoretical Capacity:

The theoretical capacity (Q) of an intercalation electrode material is considered in electrode material per weight (Ah/Kg or mAh/g). Considering the molar mass, M in g/mol, the capacity, Q, in mAh/g is therefore calculated using the Faraday´s Law as follows:

$$Q = nF/3.6M \qquad (mAhg^{-1}) \tag{3.23}$$

Where n= number of Li per formula and F= 964800 C.

Elements with Li/M ratio of more than 3 (e.g. Si, Ge, Sr, Pd, In, Sn, Ba Pt, Au, Tl and P) are very interesting for Li alloying in Li-ion batteries.

Considering $FeSn_2$ the theoretical capacity is shown below and calculated from the typical de-insertion/insertion redox process in a lithium ion cell:

$$FeSn_2 + 8.8Li^+ \leftrightarrow 2\ Li_{4.4}Sn + Fe$$
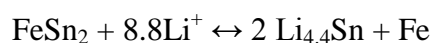
The theoretical capacity will be equal to 804 mAh/g.

In order to calculate rate in this work, we have used the mass-normalized intensities in mA/g units.

- Energy Density

The energy density is a measure of the energy storage efficiency of a battery. It can be described in two different ways;

i. Volumetric energy density: This is the amount of energy per unit volume of material. It is measured in Watt-hours/litre (Wh/l)

ii. Gravimetric energy density: This is the amount of energy per unit weight of material. It is measured in Watt-hours/kilogram (Wh/kg).

REFERENCES

1. N.H Chou, R. Schaak, Chem. Mater., 20 (2008) 2081.

2. N.H. Chou, R.E. Schaak, J. Am. Chem. Soc., 129 (2007) 7339.

3. Y.J. Hsu, S.Y. Lu, J. Phys. Chem. B, 109 (2005) 4398.

4. Y.J. Hsu, S.Y. Lu, Y.F. Small, J. Phys. Chem. B, 2 (2006) 268.

5. F. Seitz, D. Turnbull, H. Ehrenreich, "Solid State Physics", Vol.22, Academic Press, New York (1968).

6. J.A. Van Beek, S.A. Stolk, F.J.Z. Van Loo, Metallkunde, 73 (1982) 439.

7. U.G. Nwokeke, A. Chadwick, R. Alcántara, M. Alfredsson, J.L. Tirado, J. Alloys Compd., 509 (2011) 3074.

8. U.G. Nwokeke, R. Alcántara, J.L. Tirado, R. Stoyanova, M. Yoncheva, E. Zhecheva, Chem. Mater., 22 (2010) 2268.

9. R.E. Cable, R. Schaak, Chem. Mater., 17 (2005) 6835.

10. U.G. Nwokeke, R. Alcántara, J.L. Tirado, R. Stoyanova, E. Zhecheva, J. Power Sources, 196 (2011) 6768.

11. Y.T. Chen, Y.C. Chuang, J.H. Su, H.C. Yu, Y.W. Cheng-Yang, J. Power Sources, 196, (2011) 2802.

12. G. Lecayon, Y. Bouizem, C. Le Greuss, C. Reynaud, C. Boiziau, C. Juret, Chem. Phys. Lett., 91 (1982) 506.

13. C. Reynaud, C. Boiziau, C. Juret, S. Leroy, J. Perrau, G. Lecayon, Synth. Met., 11 (1985) 159.

14. U.G. Nwokeke, F. Nacimiento, R. Alcántara, J.L. Tirado, Electrochem. Solid-State Lett., 14 (10) (2011) 1.

15. F. Nacimiento, R. Alcántara, J.L. Tirado, J. Electrochem. Soc., 157 (2010) A666.

16. F. Nacimiento, R. Alcántara, J.L. Tirado, J. Power Sources, 196 (2011) 2893.

17. P.P. Ferguson, P. Liao, R.A. Dunlap, J.R. Dahn, J. Electrochem. Soc., 156 (2009) A13.

18. L. Qiu, V. G. Pol. J. Calderon-Moreno, A. Gedanken, Ultrason. Sonochem., 12 (2005) 243.

19. A. Odani, A. Nimberger, B. Markovsky, E. Sominski, E. Levi, V. G. Kumar, M. Motiei, A. Gedanken, P. Dan, A. Aurbach, J. Power Sources, 119-121 (2003) 517.

20. R. Gottesman, S. Shukla, N. Perkas, L. A. Solovyov, Y. Nitzan, A. Gedanken, Langmuir, 27 (2010), 720.

21. L. Smart, E. Moore, "Solid State Chemistry, An Introduction", 2nd Edition, Chapman and Hall (1995).

22. C. Kittel, "Introduction to Solid State Physics" John Wiley & Sons Inc., (1953).

23. W.D. Callister, "Materials Science and Engineering, An Introduction" 6th Edition. John Wiley & Sons Inc., (2003).

24. B.D. Cullity, S.R. Stock, "Elements of X-Ray Diffraction" 3rd Edition, Addison-Wesley (2001).

25. P. Gutlich, "Mössbauer Spectroscopy, Principles and Applications", Johannes Gutenberg, Germany (2005).

26. F. Menil, J.Phys.Chem.Solids, 46 (1985) 763.

27. P.J. Goodhew, J. Humphreys, R. Beanland, "Electron Microscopy and Analysis", 3rd Edition, Taylor and Francis (2001).

28. J. Goldstein, D. Newbury, D. Joy, C. Lyman, P. Echlin, E. Lifshin, L. Sawyer, J. Michael, "Scanning Electron Microscopy and X-Ray Analysis" 3rd Edition, Kluwer Academic-Plenum Publishers (1981).

29. D.K. Bowen and C.R. Hall, "Microscopy of Materials", The MacMillian Press Ltd., (1975).

30. M. De Graef, "Introduction to Conventional Transmission Electron Microscopy", Cambridge University Press, Cambridge (2003).

31. D.B. Williams, C.B. Carter, "Transmission Electron microscopy", Plenum Press, New York (1996).

32. C. Calle, R-A. Eichel, C. Finazzo, J. Forrer, J. Granwehr, I. Gromov, W. Groth, J. Harmer, M. Kalin, W. Lammler, L. Liesum, Z. Madi, S. Stoll, S. Van Doorslaer, A. Schweiger, Chimia, 55 (2001) 763.

33. C.P. Poole Jr.,"Electron Spin Resonance", 2nd Edition, Interscience Publishers (1976).

34. W. Gordy, "Theory and Applications of Electron Spin Resonance", John Wiley & Sons Inc., (1980).

35. E.D. Seletchi, "Principles and methods of Electron Paramagnetic Resonance – Dating and Dosimetry" The First International Proficiency Testing Conference, Sinaia, Romania, (2007).

36. A. Abragam and B. Bleany, "Electron Paramagnetic Resonance of Transition Ions", Clarendon Press, (1970).

37. B. Simovic, "Introduction to the Technique of Electron Spin Resonance (ESR) Spectroscopy", ETH, Zurich, Switzerland, (2004).

38. M.E. Brown, "Introduction to Thermal Analysis, Techniques and Applications", Chapman and Hall, (1988).

39. H.K.D.H. Bhadeshia, "An Introduction to Thermal Analysis Techniques", University of Cambridge Online Resource (2002).

40. R.F. Speyer, "Thermal Analysis of Materials", School of Materials Science, Mercel Dekker Inc., (1994).

41. D. Linden, T.B. Reddy (Editors), HandBook of Batteries, 3rd Ed. McGraw-Hill, New York (2001).

42. R.A. Huggins, "Advanced Batteries", Springer Science + Business Media, LLC, (2009).

43. P.H. Rieger, "Electrochemistry", Prentice-Hall International Inc., (1987).

44. J.R. Akridge, M. Balkanski, ed, "Solid State Microbatteries", Plenum Press, (1990).

45. "Electrochemistry-Application Note No. 1, Biologic Science Instruments. http://bio-logic.info .

4. RESULTS AND DISCUSSION

4.1.   Nano- and micro-FeSn$_2$

4.1-1.   Structure and morphology

For the sake of comparison, samples of FeSn$_2$ with different particle sizes were obtained. The observed XRD pattern of the obtained FeSn$_2$ sample prepared by Fe^{2+} and Sn^{2+} ions reduction in TEG at 185ºC (polyol method) agrees well with the diffraction file number 25-415 (Fig. 4.1-top).
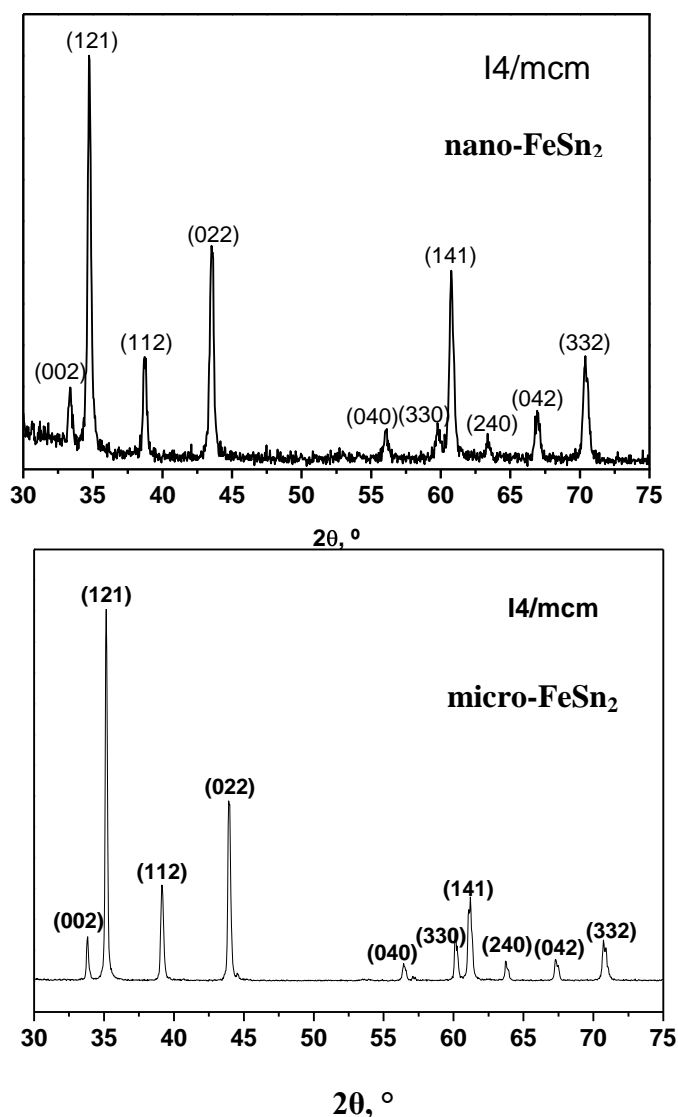
Figure 4.1. XRD pattern for crystalline FeSn$_2$ samples. Top: nano-FeSn$_2$ (185°C) Bottom: micro-FeSn$_2$ (490°C). The Miller indexes are indicated.

The nano-FeSn$_2$ sample is composed of nanosized particles of around 20 nm of diameter (Fig. 4.2a) and exhibits broadened XRD reflections (Fig. 4.1 top). These nanoparticles tend to form aggregates. Crystalline impurities are not observed. The calculated tetragonal lattice cells parameters are a=b=6.55(1) Å and c=5.365(2) Å. The average grain size obtained by applying the Scherrer equation to the most intense reflection is equals to 26 nm. The TEM micrographs (Fig. 4.2 a, c) show nanometric particles with poorly defined morphologies.
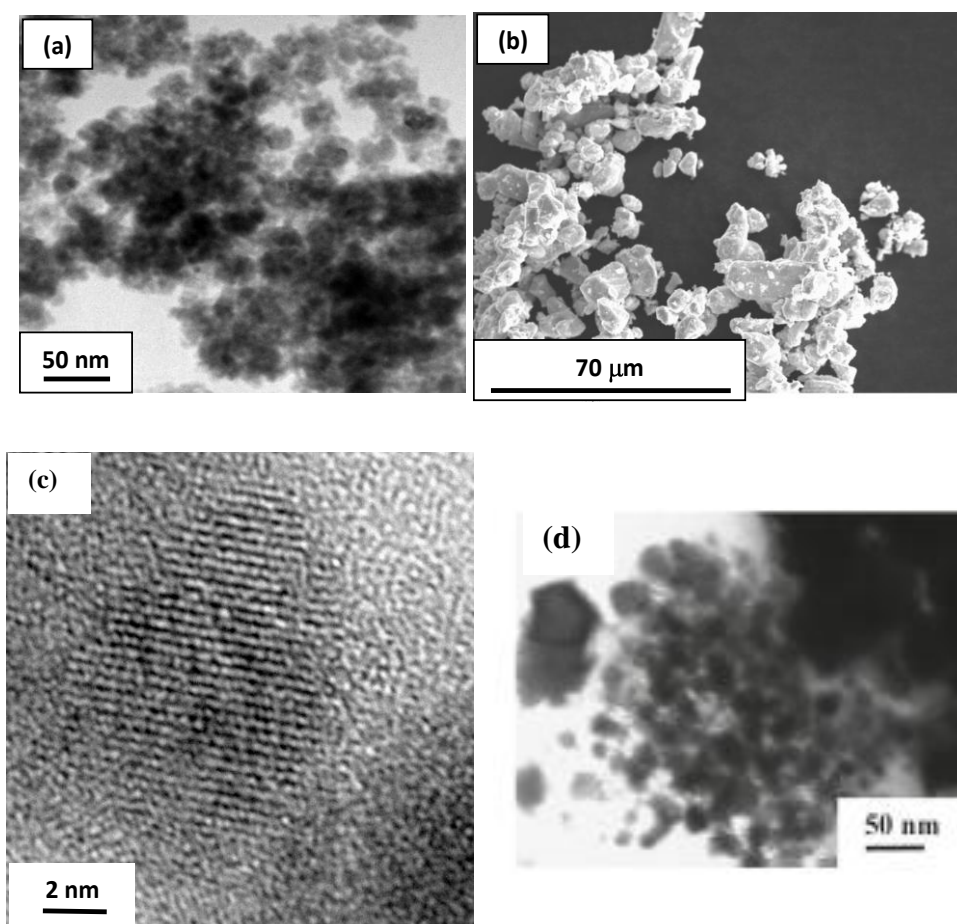
Figure 4.2. Electron microscopy of FeSn$_2$ samples. (a, c) TEM image of nano-FeSn$_2$ obtained by the polyol method. (b) SEM image of micro-FeSn$_2$. (d) Micrograph of used nano-FeSn$_2$ electrode after the first discharge.

The observation of lattice fringes within small domains evidence the nanocrystalline character of the sample. Particle size was not uniform but varied in the 6-30 nm range, leading to an average value close to the Scherrer crystallite size.

The sample prepared by heating powders of Fe and Sn at 490ºC under Ar atmosphere is composed of micrometric particles with irregular morphologies (Fig. 4.2b) and exhibits narrow XRD reflections (Fig. 4.1 bottom). The EDAX microanalysis reveals that the experimental tin/iron ratio is the expected, for both micro-$FeSn_2$ and nano-$FeSn_2$ samples.

The ^{57}Fe Mössbauer spectroscopy of $FeSn_2$ samples are shown in Fig. 4.3. The spectra illustrate the influence of particle size on magnetic ordering. Micro-$FeSn_2$ shows a sextuplet at isomer shift value $\delta=0.50(1)$ mm/s due to the expected antiferromagnetic behaviour. In contrast, the ^{57}Fe MS of the nano-$FeSn_2$ contains a singlet signal at isomer shift value $\delta=0.51(4)$ mm/s, which is indicative of a superparamagnetic state at room temperature. The small particle size hinders the long-range magnetism. The particles with very small size can exhibit smaller recoil-free fraction and drive to MS with lower intensity and broadened [1]. According to previous neutron diffraction and Mössbauer spectroscopy studies, [2] micrometric $FeSn_2$ is antiferromagnetic below 378 K (T_N), and a second magnetic transition occurs at 93 K (T_t). Between T_N and T_t the magnetic structure is collinear and characterized by ferromagnetic (100) planes, antiferromagnetically coupled along the [100] direction. Below T_t, $FeSn_2$ becomes non-collinear antiferromagnetic. For $FeSn_2$ with very small grain sizes, a super-paramagnetic state is found at room temperature [3]. The ^{57}Fe Mössbauer spectrum of the nano-$FeSn_2$ sample (Fig. 4.3) agrees with this description. A superparamagnetic singlet is observed with the expected isomer shift (0.51(4) mm/s, Table 4.1) for the intermetallic compound [3, 4].
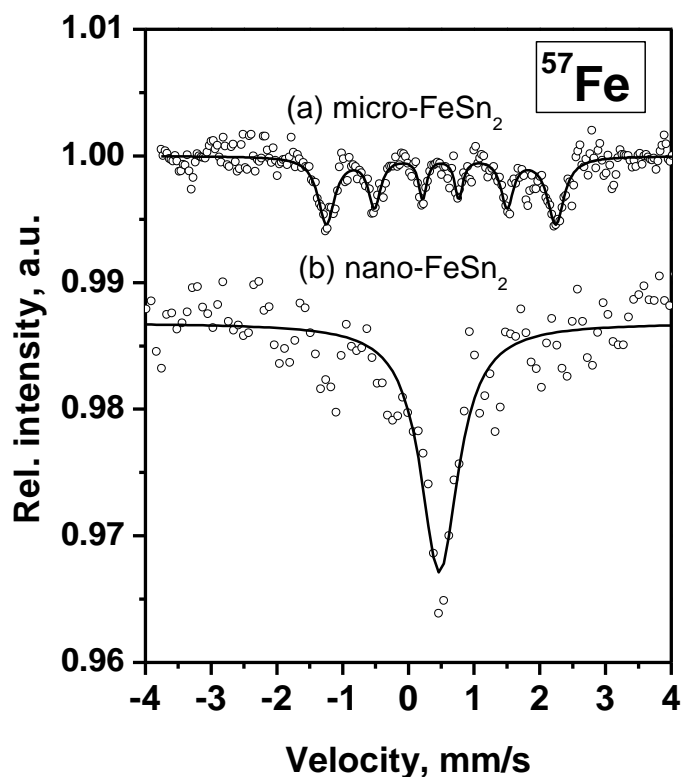
Figure 4.3. Room temperature ^{57}Fe Mössbauer spectra for (a) micro-FeSn$_2$ and (b) nano-FeSn$_2$.

The room temperature ^{119}Sn Mössbauer spectrum of nanocrystalline FeSn$_2$ shows a broadened and low intensity signal that can be fitted with a doublet (Fig. 4.4-top, Table 4.1). This doublet is centred at isomer shift δ= 1.91(3) mm/s and the quadrupole splitting value is Δ=2.10(4) mm/s. This quadrupole splitting value is apparently high having in mind that an octet is common for FeSn$_2$ microparticles at room temperature [5]. In fact, what we see is a poorly-resolved signal resulting from the depression in the magnetic ordering in FeSn$_2$ nanoparticles. The bonding with some covalent character reduces the electron densities at the nuclei and decreases the isomer

shift value as compared to pure Sn [6]. Tin oxides are not detected. The small particle size can decrease the recoil-free fraction of the tin atoms and the decrease the signal intensity.
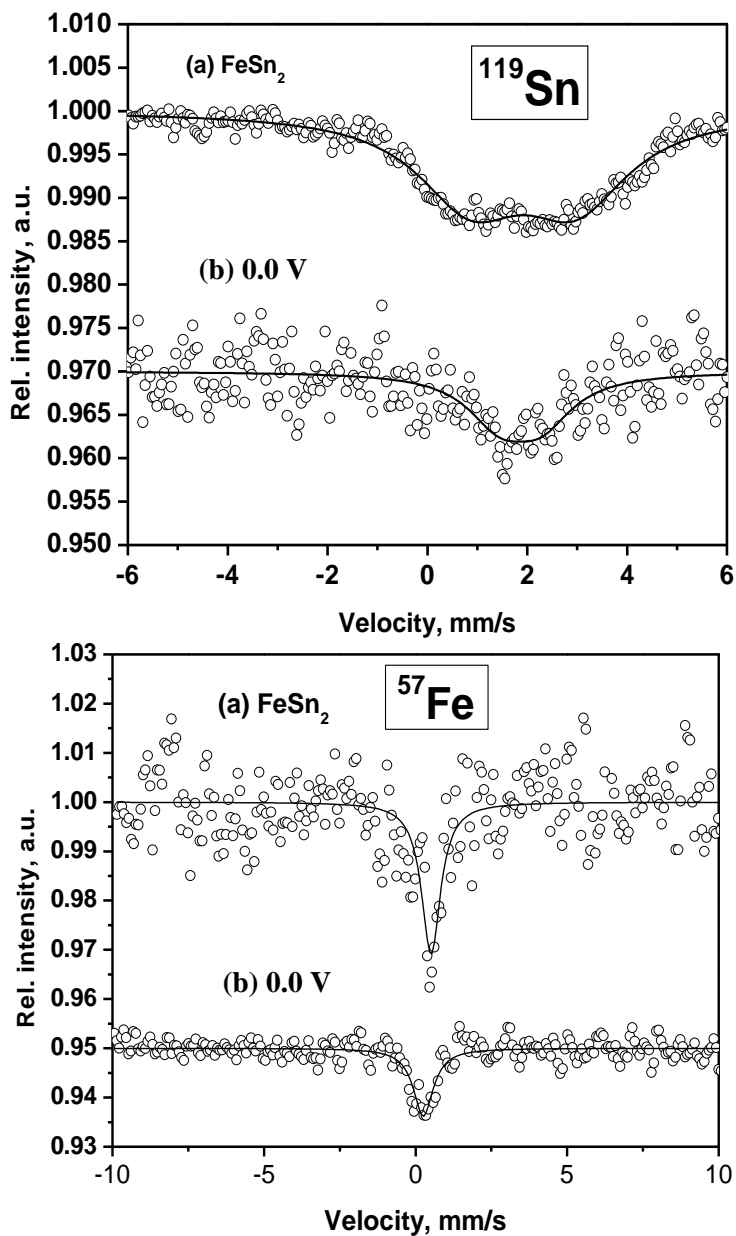
Figure 4.4. ^{119}Sn and ^{57}Fe Mössbauer spectra of a pristine nanocrystalline FeSn$_2$ and electrodes discharged to 0.0 V.

Table 4.1. Results of the ^{119}Sn and ^{57}Fe Mössbauer spectra fitting for (a) nano-FeSn$_2$ and (b) electrodes discharged to 0.0 V vs. Li$^+$/Li.

Notation	Atom	δ	Δ	Γ	C
(a) pristine	^{119}Sn	1.91(3)	2.10(4)	2.6(1)	100
	^{57}Fe	0.51(4)	–	0.8(1)	100
(e) 0.0 V	^{119}Sn	1.9(1)	0.8(2)	1.6(4)	100
	^{57}Fe	0.26(3)	–	0.8(1)	100

δ: isomer shift (mm s^{-1}). Δ: quadrupole splitting (mm s^{-1}). Γ: line width (mm s^{-1}). C: relative contribution (%).

EPR was furthermore used for analysis of nanocrystalline FeSn$_2$. The influence of the small particle sizes is evidenced on the EPR spectra. At high-registration temperature, the EPR spectrum of pristine nanosized FeSn$_2$ consists of nearly symmetric line (Fig. 4.5). On cooling, the EPR signal becomes anisotropic. In the same time, the EPR signal intensity decreases and below 140 K the signal disappears. This means that for pristine nanosized FeSn$_2$ the EPR signal comes from magnetically correlated spins, which are ordered in a long-range below 140 K. The EPR results are in agreement with the magnetic properties of nanocrystalline Fe-Sn alloys [3, 7]. It is worth mentioning that there is no resonance signal due to iron oxide phases. This result outlines the capability of the polyol method to prepare pure FeSn$_2$ with very small particles.
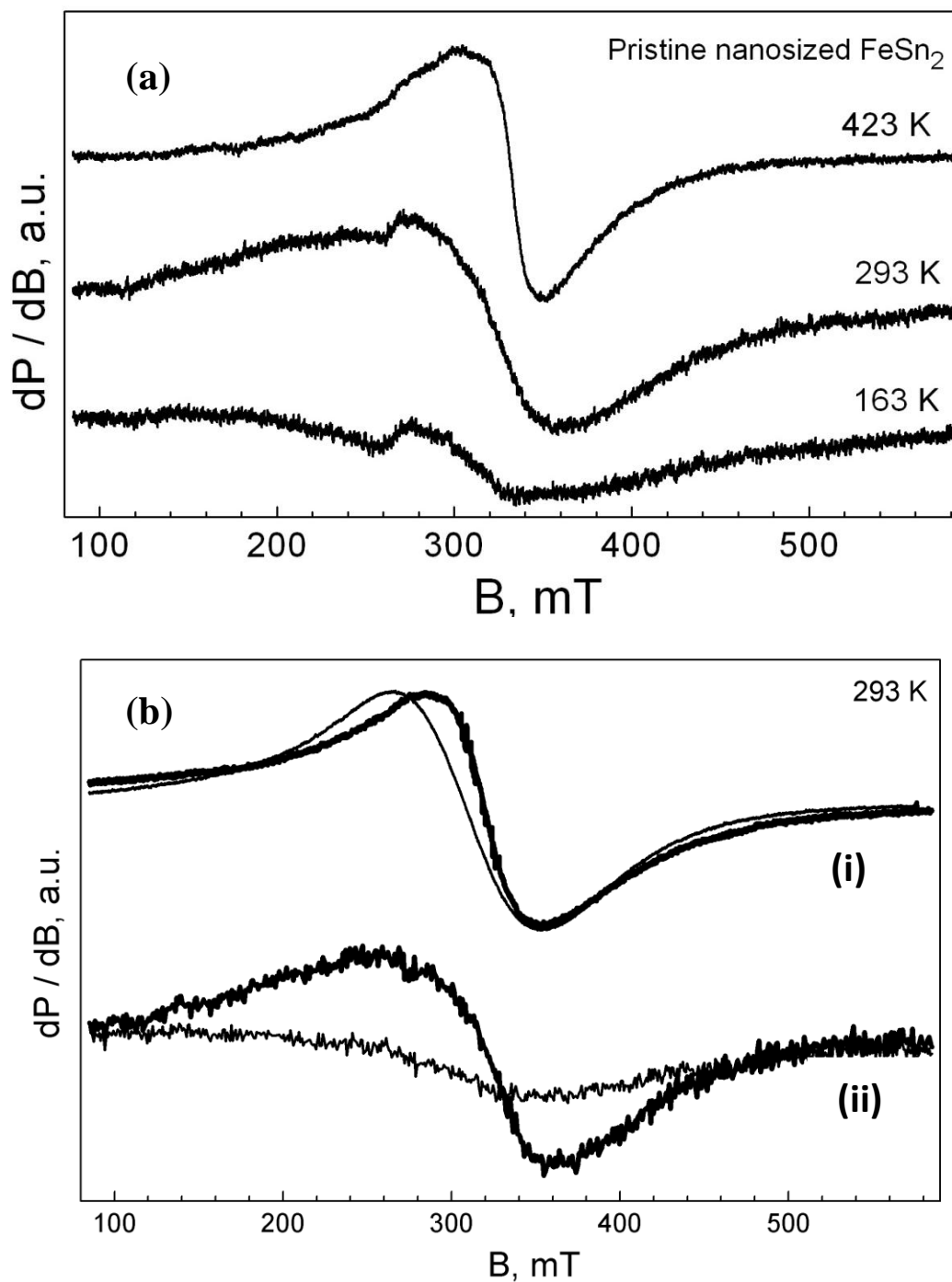
Figure 4.5. (a) EPR spectra of pristine $FeSn_2$ at several temperatures. (b) EPR spectra of pristine $FeSn_2$ (i) and $FeSn_2$ discharged up to 1.15 V (ii) registered at 293 K (bold lines) and 143 K (thin lines).

4.1-2. Thermal analysis

Differential thermal analysis results for micro- and nano-FeSn$_2$ are shown in Figs. 4.6 and 4.7. Firstly, the DTA curve was obtained while heating the sample under Ar-flow. Then, the sample was cooled with continuous Ar-flow, and the second DTA curve was obtained by re-heating under Ar-flow. After cooling under Ar-flow, the inert gas flow was stopped and the third DTA curve was obtained by re-heating the sample in air.
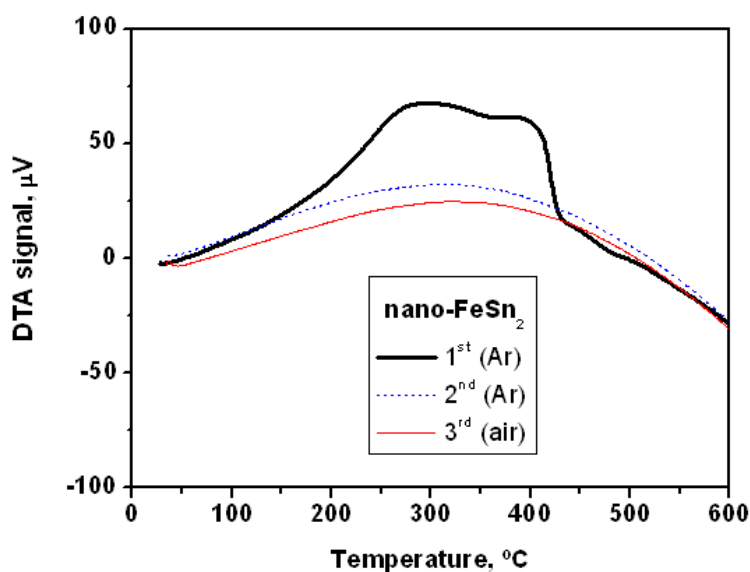
Figure 4.6. DTA of nano-FeSn$_2$ for the first and second heating processes under Ar-flow, and third heating in air.

The first heating process of nano-FeSn$_2$ under Ar-flow (Fig. 4.6) shows a broad exothermal feature between ca. 200 and 430ºC, while no endothermal peak is observed at the melting point of pure tin (232ºC). This exothermal region has a complex nature and may involve several processes. In principle, it may be related to the growth of the nanocrystalline grains and reduction of their surface energy, phase transformation and oxidation. Exothermal peaks were also previously reported for nano-CoSn$_3$ [8] and nano-Sn$_3$Co$_3$C$_4$ [9]. The participation of oxidative processes due to traces of oxygen cannot be ruled out, particularly due to the expected reactivity of the surface of very small metallic particles. For example, previous studies showed that metallic Fe

nanoparticles are exothermally oxidized at 177ºC [10]. To ensure the validity of the results, after this first heating process, the same sample was cooled and re-heated under continuous Ar-flow. The second heating process shows no thermal events. On the contrary, the DTA curve of micro-$FeSn_2$ (Fig. 4.7) does not show any exothermal processes in the first heating from room temperature to 700ºC. Small endothermal peaks are observed at 443ºC and around 513-540ºC which more probably are related to phase transformations. According to the phase diagram, $FeSn_2$ decomposes at 513ºC. In the second heating of micro-$FeSn_2$, an intense and endothermal peak is observed at the melting point of Sn, indicating the previous decomposition of micro-$FeSn_2$ during the first heating. Since the melting peak of Sn is not observed in the second heating of nano-$FeSn_2$, it can be deduced that nano-$FeSn_2$ does not decompose in the first heating most probably because it is oxidized with traces of oxygen. A third heating process was carried out in air, and no thermal events are observed for nano-$FeSn_2$.
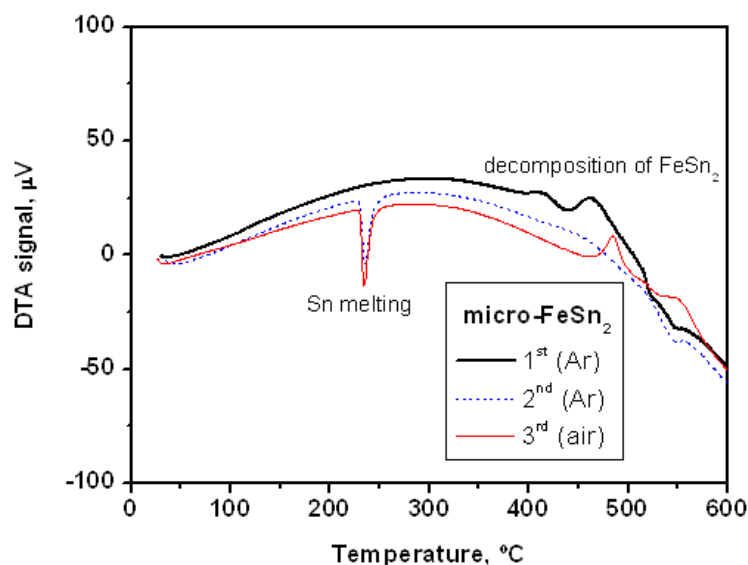
Figure 4.7. DTA of micro-$FeSn_2$ for the first and second heating processes under Ar-flow, and third heating in air.

Irrespective of the poor crystallinity, the XRD pattern (Fig. 4.8a) of the nanosized sample after the third heating showed only very broadened reflections

corresponding to SnO_2. After the third heating process in air, the microsized sample shows the endothermal peak of tin melting point and an exothermal peak at 484°C as a result of oxidation in air (Fig. 4.7). The XRD patterns of the sample recuperated from this last DTA experiment confirmed the occurrence of SnO_2 and Fe_2O_3 (Fig. 4.8b). These results show the higher reactivity of the surface of the intermetallic nanoparticles in comparison with the microparticles.
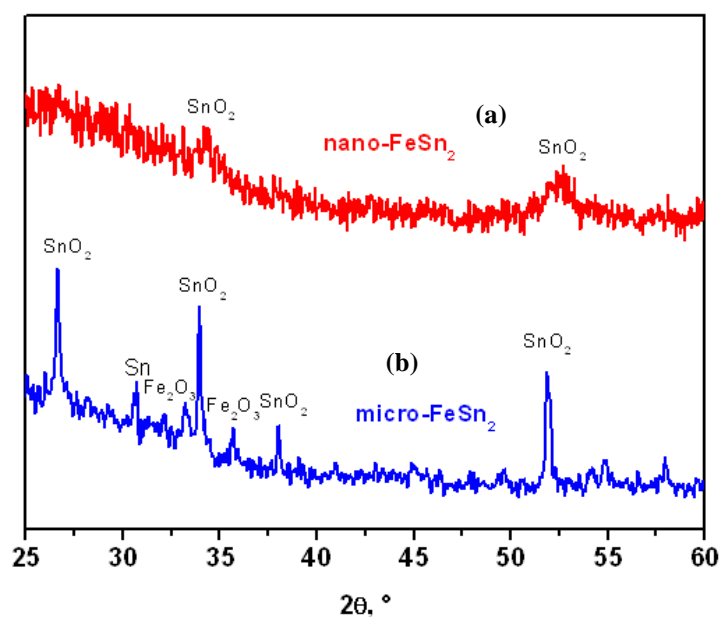
Figure 4.8. XRD pattern of (a) nano-$FeSn_2$ and (b) micro-$FeSn_2$ after third DTA heating in air.

4.1-3. Electrochemistry

The effect of the particle size is particularly dramatic in the electrochemical performance. Nano-$FeSn_2$ exhibits much better electrochemical behaviour than micro-$FeSn_2$ (Figs. 4.9 and 4.10). A reversible discharge capacity above 500 mAh/g is observed in lithium test cells (Fig. 4.9). In comparison with bulk samples and results already in literature, there is a significant improvement in electrochemical behaviour which makes it an interesting anode material for lithium-ion batteries. Two possibilities of poor capacity retention in microparticles: core not reached by lithium or particle

fragmentation due to mechanical stresses leading to the loss of electrical contact. To discern between both options, it can be seen that both samples have almost the same capacity during the first two cycles. Thus, the core of the particles seems to be accessible to lithium for the starting material in both samples. The very small particles exhibit much better cycling behaviour for the nano-FeSn$_2$ electrodes, while the very large particles lead to rapid pulverization, loss of electrical contact and subsequent capacity fading of the micro-FeSn$_2$ electrodes.
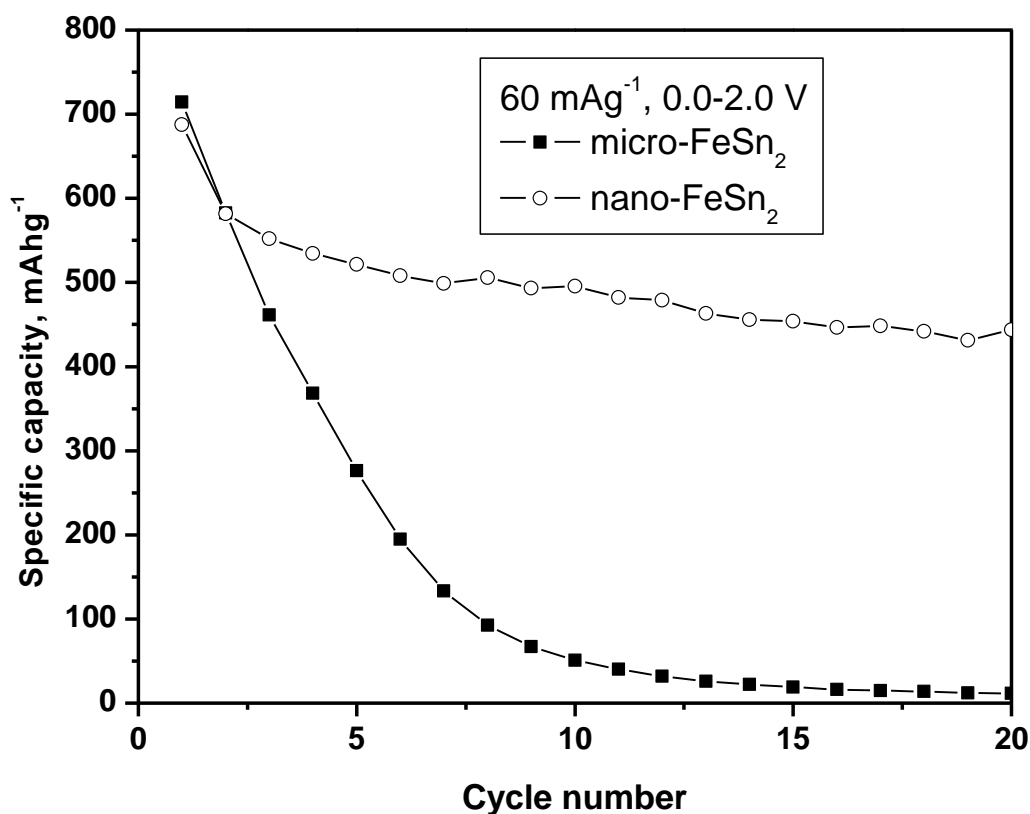
Figure 4.9. Specific capacity as a function of cycle number for microcrystalline and nanocrystalline FeSn$_2$.

The derivative plots of the corresponding galvanostatic discharge-charge cycles are shown in Fig. 4.10 for micro-FeSn$_2$ and nano-FeSn$_2$. The formation of surface films

(SEI) in the very small particles is more evident for the first discharge of nano-$FeSn_2$, and an irreversible peak is observed at 1.3 V. This result is in good agreement with the DTA experiments shown above that demonstrate a higher surface reactivity for nano-$FeSn_2$. The reduction of amorphous oxides in the surface of the nanoparticles also may contribute to the irreversible peak at 1.3 V. The higher surface reactivity is also demonstrated by the EPR spectrum of nano-$FeSn_2$ discharged up to 1.15 V. The EPR spectrum of pristine nano-$FeSn_2$ is changed at lower depth of discharge, as a result of which a single Lorentzian line becomes visible (Fig. 4.5b). The signal is broadened on cooling (from 300 to 100 K) together with a shift of the effective resonance absorption towards a lower magnetic field (Fig. 4.5b).

The occurrence of Li_xSn phases is evidenced by several peaks in the derivative plots of both micro and nanosized samples (Fig. 4.10). The peak at 0.58 V in the first charge of micro-$FeSn_2$, which corresponds to the extraction of lithium from Li_xSn phases, becomes less intense and is shifted to higher potentials from the first to the third cycle (Fig. 4.10 (a)). It seems that lithium is hardly removed from the Li_xSn grains. The peak at ca. 0.4 V in the discharge process shifts to lower potentials when the cycle number increases. Consequently, the polarization of the cell is higher for the micro-$FeSn_2$ when the cycle number increases. In contrast, the derivative plot of nano-$FeSn_2$ remains almost unchanged after the first discharge, suggesting the best stability of the electrode nanomaterial (Fig. 4.10 (b)). The electrochemical process involves the conversion of the $FeSn_2$ nanocrystals into Li_xSn phases. The reaction mechanism of nano-$FeSn_2$ differs from micro-$FeSn_2$, which evidences the dramatic effect commonly exerted by nanodispersion on the behaviour of electrode materials for lithium ion batteries. In the case of micro-$FeSn_2$, the iron particles do not hold the processes of alloying/dealloying between tin and lithium. The derivative curve of the first discharge exhibits a very intense peak at ca. 0.1 V and a low-intensity signal at 1.3 V (Fig. 4.10). The peak at 1.3 V is irreversible and is ascribed to side reactions such as electrolyte solution consumption and formation of a solid electrolyte interface or, alternatively, to true lithium insertion into $FeSn_2$. In addition, the participation of some organic residues (such as PEO and TEG) in side reactions cannot be ruled out. The peak at 0.1 V is also irreversible and is ascribed to the destruction of the $FeSn_2$ structure and formation of lithium-containing intermetallics. The formation of Fe and Li_xSn grains was previously reported [3]. In the charge process, the peaks centred at 0.57, 0.45 and 0.7 V are

ascribed to the extraction of lithium from Li_xSn phases. The peak centred at 0.38 V in the second discharge is ascribed to the formation of Li_xSn. The iron atoms seem to act as "spectators" of the electrochemical reactions between Li and Sn and might help to maintain the electrode integrity. These results are in agreement with previous studies [11].
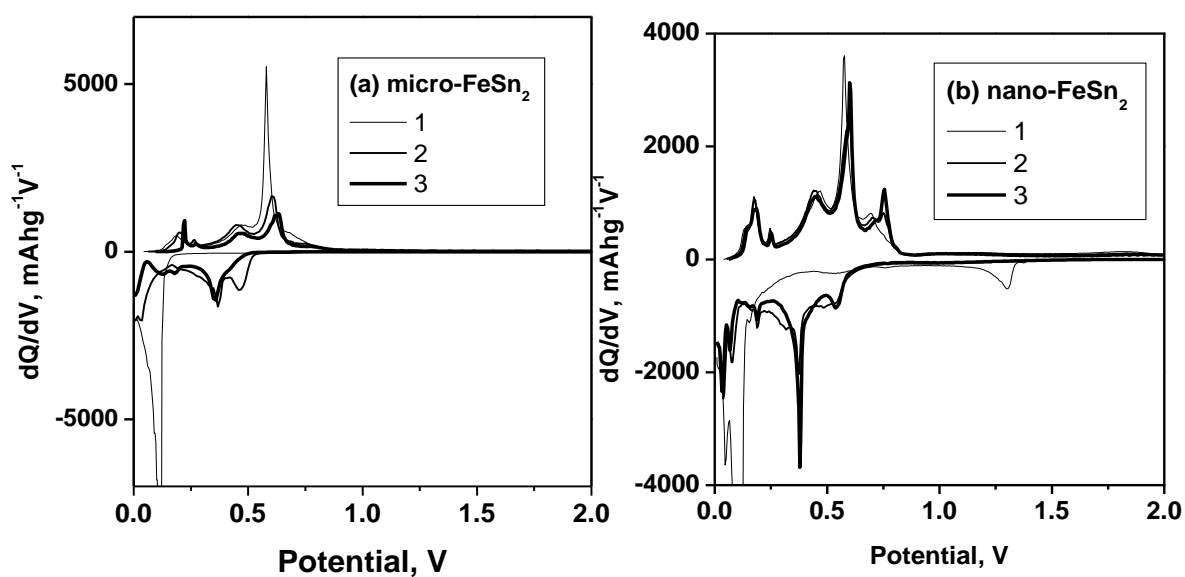
Figure 4.10. Derivative plots of the first three cycles for (a) micro-FeSn₂ and (b) nano-FeSn₂.

The origin of the better behaviour of the nano-sample results from two different phenomena. First, both micro- and nano-particles seem to react completely with lithium during the first discharge, as evidenced by the initial capacities, which have similar values. However, capacity degrades sharply on successive cycles for the micro-sample. It is a well-known fact that tin intermetallics suffer giant volume changes (Fig.4.11) on lithium insertion-deinsertion, which lead to particle fragmentation and the loss of

110

electrical contacts, with the subsequent capacity fade [12-16]. This is avoided in the nano-sample, as the size of the particles is sufficiently small (as shown by both [57]Fe MS and EPR) to retain a small size basically unaltered during cycling. A second factor is the lack of participation of iron nanoparticles generated after the first discharge in the cycling of the nano-sample, which is studied below in the light of the EPR data. This phenomenon provides a constant conducting matrix of metallic particles which also contributes to the preservation of the size of the nanodomain.
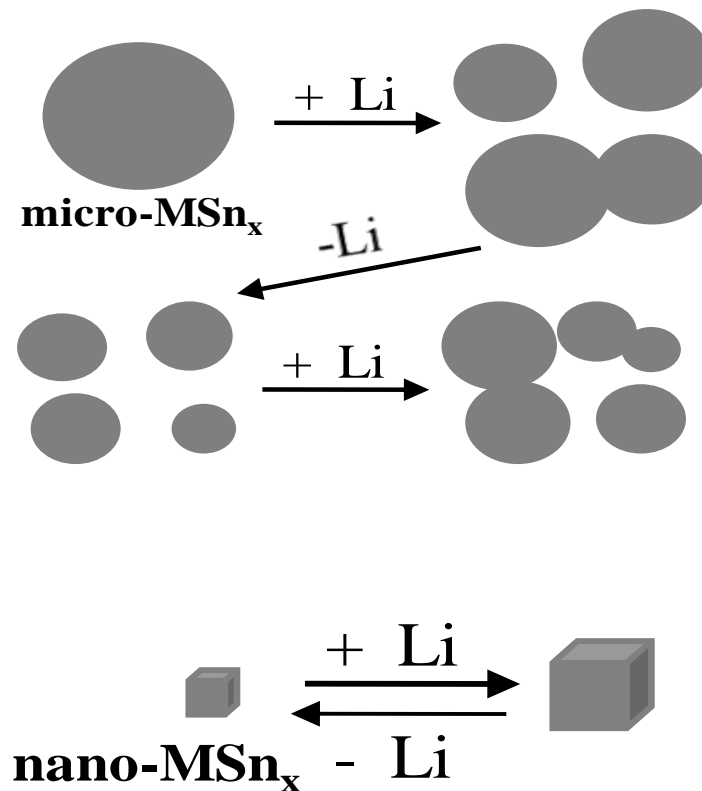
Figure 4.11. A schematic representation of changes in lattice cell volume, break-up of particles and loss of electrical contact during discharge-charge of electrodes for microsized particles in comparison with the ductile behaviour of the nanosized particles.

Further electrochemical studies were carried on nanocrystalline $FeSn_2$ at various cycling conditions. The electrochemical behaviour of nanocrystalline $FeSn_2$ in lithium test cells is shown in Figs. 4.12 and 4.13. The capacity of the first discharge, which is referred to the mass of $FeSn_2$, exceeds the theoretical maximum value (Fig. 4.12). Henceforth, it is assumable that side reactions are taking place in the surface of the nanoparticles. The graphite additive used as conductive agent also can contribute to the excess of capacity. The irreversible part of the first cycle is around 200 mAh/g, depending on the cycling conditions. Reversible capacity values slightly over 800 mAh/g are observed in the first cycles. The values are near the maximum theoretical capacity (804 mAh/g). Most of this capacity is developed between 0.0 and 0.8 V.
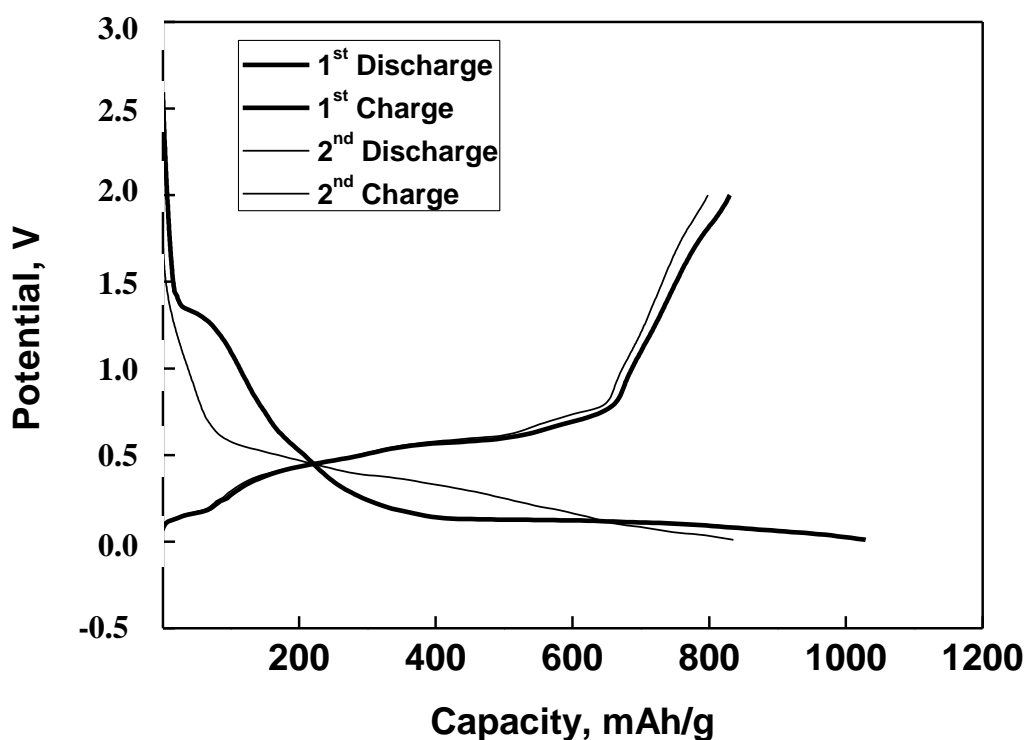
Figure 4.12. Potential-capacity curves for nano-$FeSn_2$ at 30 mA/g.
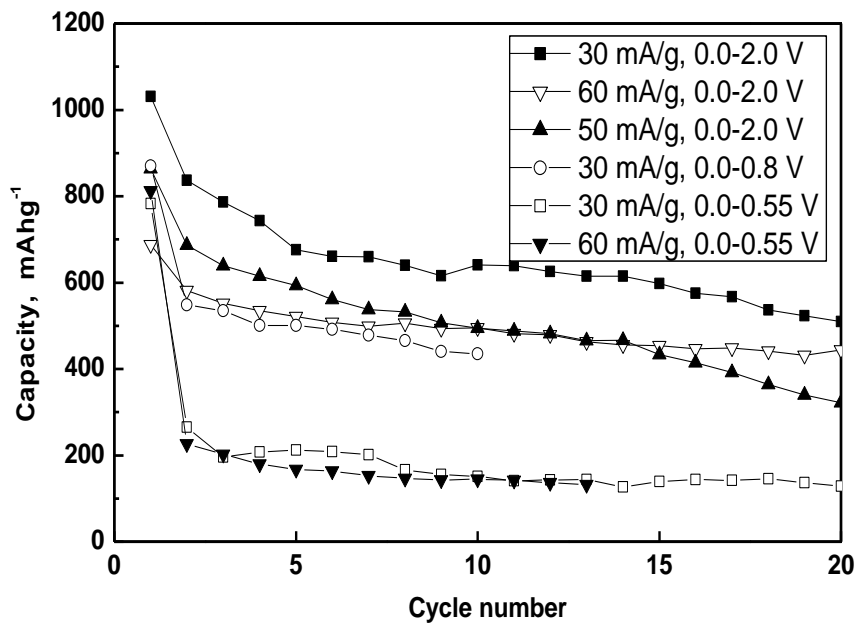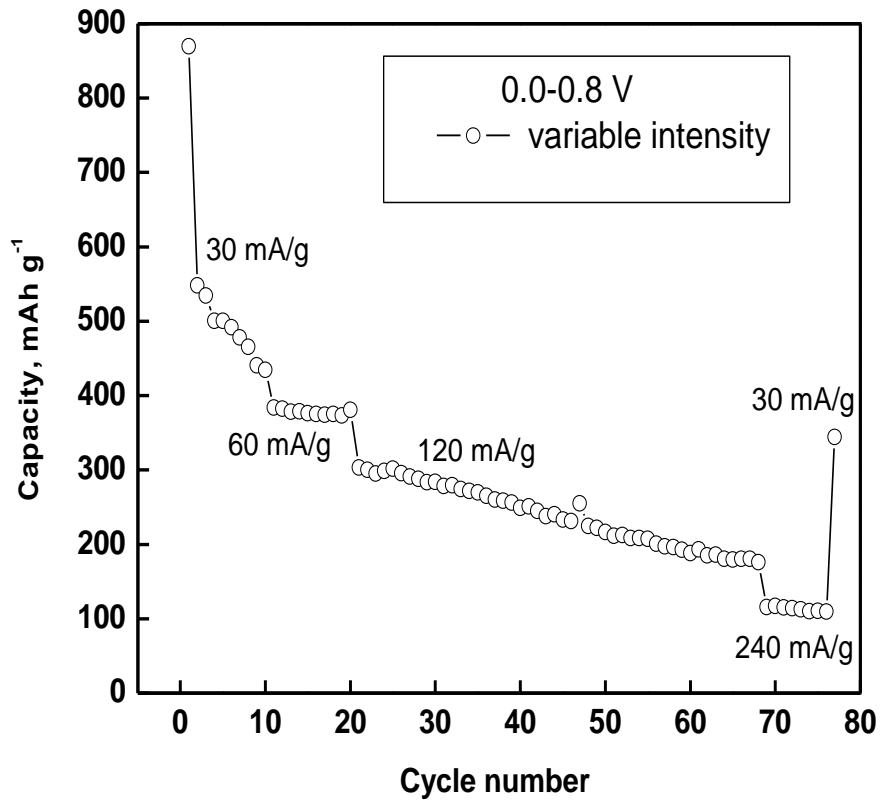
Figure 4.13. Specific capacities as a function of cycle number for nano-FeSn$_2$ electrodes in Li cells at several current intensities and potential limits.

For 2.0 and 0.8 V as upper potential limits, the observed capacity retention is poor independently of the current (Fig. 4.13). It seems that the volume changes due to Li-Sn alloying and de-alloying processes make that the particles lose their electrical contacts. The capacity decreases when the current is increased from 30 to 240 mA/g. An enhanced cycle life for the cells cycled between 0 and 0.55 V was observed by other authors [3].

4.1-4. Reaction mechanism

To study the reaction mechanism, the electrochemical cells were interrupted at selected states of discharge-charge, and XRD (Fig. 4.14) and spectroscopic measurements were carried out *ex-situ*.

After partial discharge to 495 mAh/g the XRD pattern (Fig. 4.14d) still exhibits the reflections of the $FeSn_2$ phase, and the reaction products remain XRD-undetectable. Mao et al observed residual $FeSn_2$ after whole discharge, and this phase disappeared after holding the cell at 0 V for 1 day [3]. After partial discharge to 600 mAh/g and recharge up to 2.0 V (Fig. 4.14g), low-intensity reflections corresponding to unreacted $FeSn_2$ are observed, and a narrow reflection corresponding to $Li_{13}Sn_5$ (ICDD file nº 29-0838) is also observed. After complete discharge to 0.0 V (Fig. 4.14e), the original $FeSn_2$ is not detected, while the low-intensity reflections observed at ca. 24 and 39º/2θ are ambiguously ascribable to both $Li_{22}Sn_5$ [17] and Li_7Sn_2 [18]. Metallic iron is not detected.
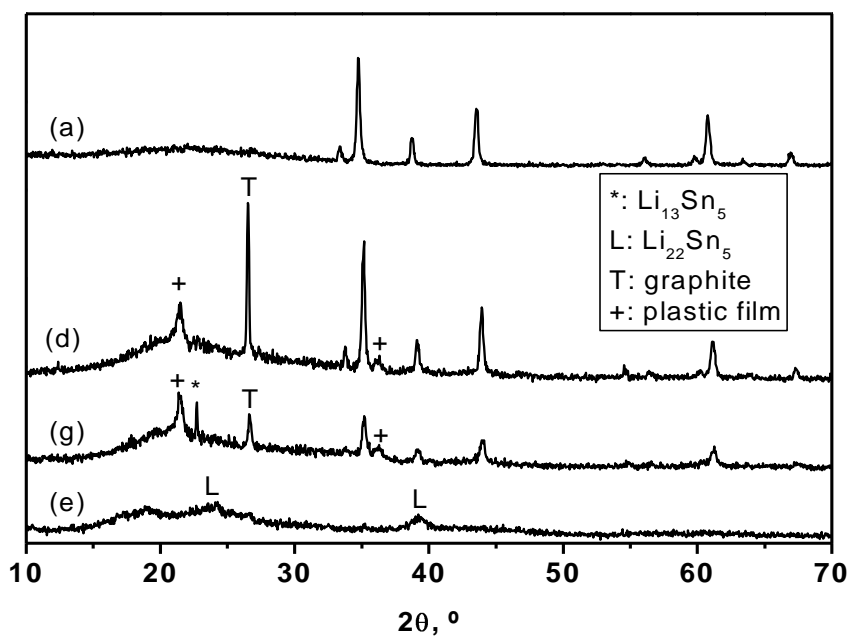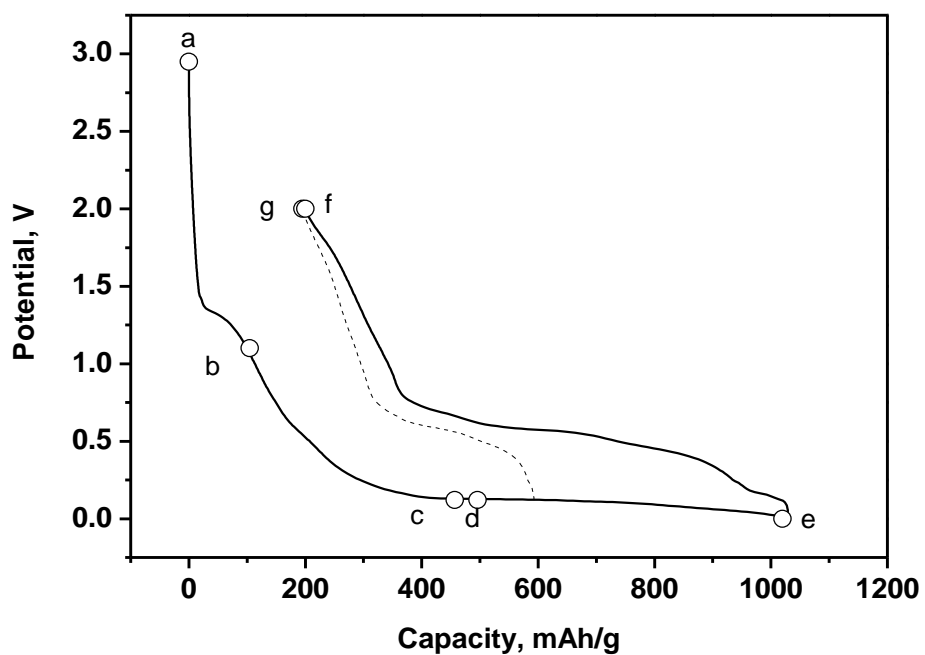
Figure 4.14. Top: The selected points for *ex-situ* measurements are indicated (a-g). Bottom: XRD patterns for pristine $FeSn_2$ (a), and recuperated electrodes at selected states of discharge (d, e) and recharge (g).

These features imply the segregation of iron (XRD-undetected small grains) from the original $FeSn_2$ phase and formation of Li_xSn phases. For that reason, *ex-situ* Mössbauer spectroscopy was used complimentary to XRD experiments.

Irrespective of the low absorption, the [119]Sn Mössbauer spectrum of the discharged electrode (0.0 V, Fig. 4.4 top-b, Table 4.1) becomes narrower than the starting $FeSn_2$ spectrum, and is centred at a value (δ= 1.9(1) mm/s) that is close to the values corresponding to $Li_{22}Sn_5$ (δ= 1.837(3) mm/s) or Li_7Sn_2 (average shift 1.960 mm/s).

The [57]Fe Mössbauer spectrum (Fig. 4.4 bottom-b, Table 4.1) shows that the isomer shift decreases significantly after lithium insertion, which is indicative of the conversion from $FeSn_2$ to metallic iron. However, the shift never reaches 0.0 mm/s, the value corresponding to α-Fe. Also the magnetic ordering of α-Fe is not seen at room temperature, probably indicating the superparamagnetic nature of the iron product, most probably in the form of nanodomains. In addition, it has been shown that small amount of tin can be incorporated into α-Fe leading to the formation of $\alpha\text{-}Fe_{1-x}Sn_x$ with x≤0.08 [19]. The possible contribution of tin containing iron superparamagnetic particles into [57]Fe Mössbauer spectrum can also be taken into account. The EPR data described below shed new light on these phenomena.

The EPR spectrum of $FeSn_2$ is changed immediately after lower depth of discharge (Fig. 4.15b). In the temperature range of 100 – 300 K, the EPR spectrum displays a single line with Lorentzian shape. The Lorentzian signal is broadened on cooling together with a shift of the effective resonance absorption towards a lower magnetic field (Fig. 4.15). For $FeSn_2$ with a higher depth of discharge, the Lorentzian line shape is preserved. The effective g-factor and the EPR line width depend on the registration temperature in a same manner as in the case of $FeSn_2$ with lower depth of discharge (Fig. 4.15 c,d). This means that EPR signal has the same origin for samples with different discharge depth. The observed EPR parameters are typical for superparamagnetic resonance (SPR). For randomly oriented mono-domain magnetic particles, a phenomenological description of the relationship between the line width and the shift of the effective resonance absorption has been proposed by Nagata and Ishimira [20]:

$$(B_r - B_{r(T=293)}) \sim \Delta H_{pp}^{3}$$

where $(B_r - B_{r(HT)})$ corresponds to the resonance field shift in respect of the resonance at high temperature and ΔH_{pp} is the line width. Figure 4.15 gives this relationship for $FeSn_2$ partially discharged (b,c,d) and totally discharged (e). As one can see, the relationship is obeyed for the three electrodes. This relation evidences the presence of a single domain superparamagnetic phase, which corroborates [57]Fe Mössbauer studies of discharged $FeSn_2$ electrodes.
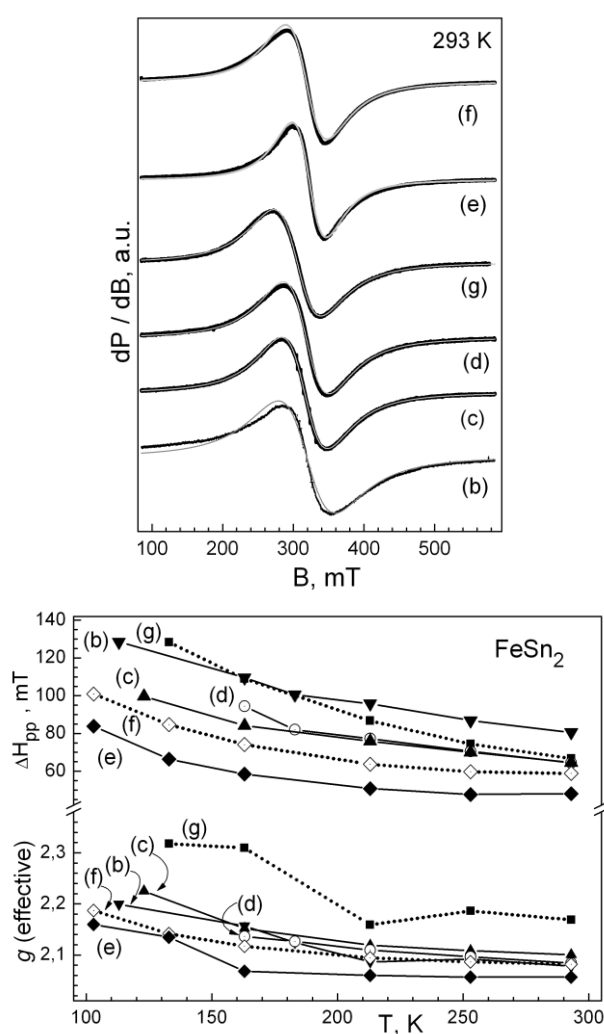
Figure 4.15. Top: EPR spectra of $FeSn_2$ electrodes at selected states of discharge (b,c,d,e) and recharge (g,f). Bottom: Effective *g*-factor and EPR line width, ΔH_{pp}, of $FeSn_2$ electrodes. For the notation meaning, see Fig. 4.14-top.
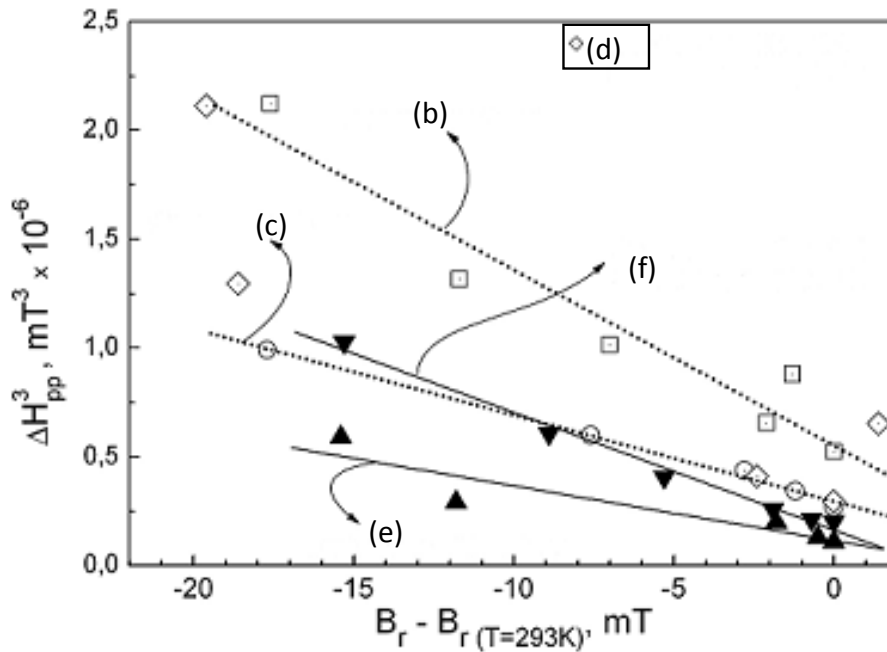
Figure 4.16. Relationship between the resonance field shift (relative to a higher-temperature value, $(B_r - B_{r(T)293})$) and line width, ΔH^3_{pp}.

The EPR parameters that change with the depth of discharge are the line width and the signal intensity (Fig. 4.18). There is a smooth decrease in the line width with the discharge depth. The signal intensity increases dramatically, passing through a maximum at a discharge depth of 460 mAh/g (Fig. 4.17). It should be mentioned that for superparamagnetic resonance the signal intensity follows the particle magnetization which on its turn is determined by the particle shape and dimension [20, 21]. This means that the variation in the signal intensity can be related with the temperature dependence of magnetization of superparamagnetic particles [22]. For samples with a lower depth of discharge, the signal intensity is reversibly proportional to the registration temperature in accordance with Curie law (Fig. 4.18). The slope of the "I-1/T" dependence is controlled by the spontaneous magnetization and the volume of the particles. This behaviour is characteristic of a superparamagnetic assembly of ferromagnetic nanoparticles with narrow size distribution. When the depth of discharge

increases, the temperature dependence of the signal intensity becomes more complex. This indicates an appearance of superparamagnetic particles with different magnetizations and volumes.
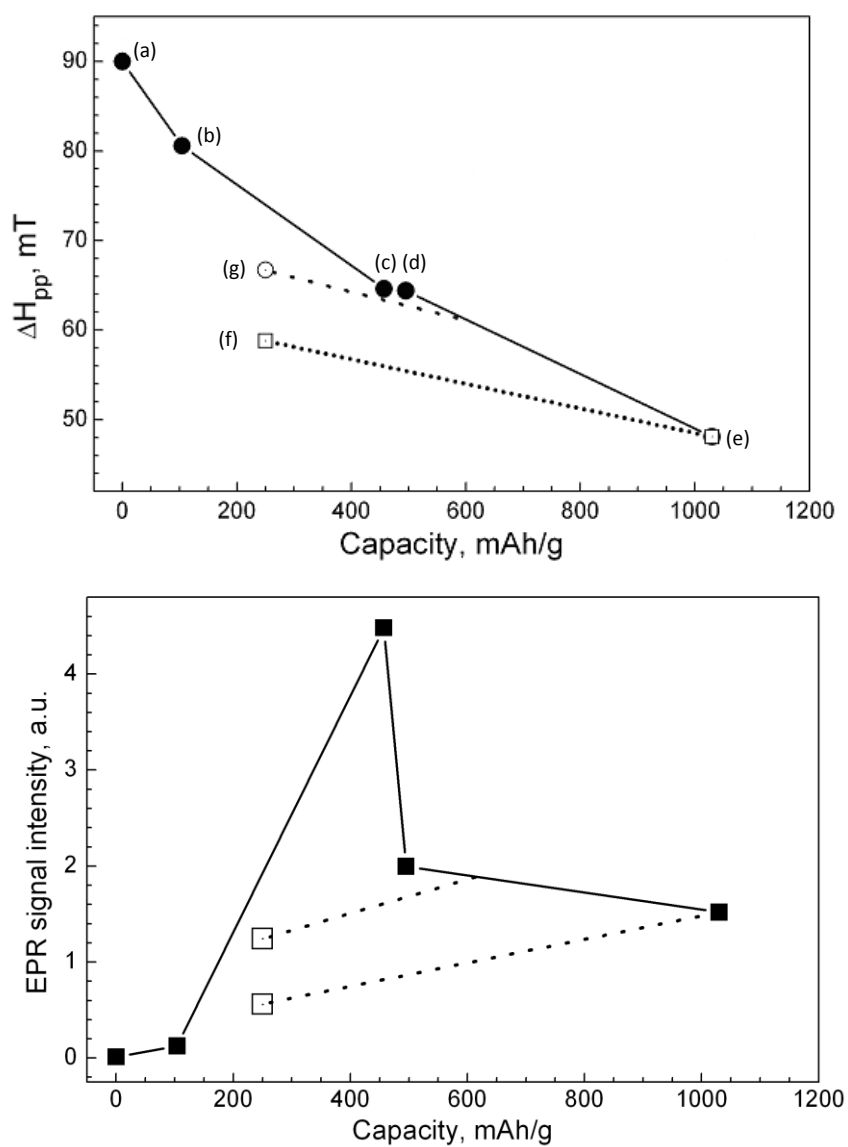
Figure 4.17. EPR line width (ΔH_{pp}) and signal intensity *versus* depth of discharge of nano-FeSn$_2$. The open symbol corresponds to recharged samples. For the meaning of the symbols (a)-(g), see Fig. 4.14.

When $FeSn_2$ is recharged to 2 V, the EPR spectrum of pristine $FeSn_2$ is not recovered (Fig. 4.15f). The EPR spectrum consists of a narrow Lorentzian line with EPR parameters close to that of discharged $FeSn_2$. This indicates that signal from superparamagnetic particles contributes also to the EPR spectrum of recharged $FeSn_2$. It is noticeable that the signal intensity is lower as compared to discharged samples (Fig. 4.17). In addition, the EPR line width and signal intensity of recharged $FeSn_2$ depend on the depth of the first discharge. When $FeSn_2$ is discharged to 600 mAh/g followed by a charge to 2.0 V (g), the EPR line width and signal intensity are higher in comparison of that of $FeSn_2$ discharged to 1030 mAh/g and consecutively charged to 2.0 V (f). Contrary to deeply discharged electrodes, the temperature dependence of the signal intensity falls on a straight line (Fig. 4.18). This indicates a change in magnetization and volume of superparamagnetic particles. To describe the picture quantitatively, EPR standards for superparamagnetic Fe and Sn-doped Fe are needed. The lack of suitable EPR standards prevents the accurate theoretical calculations of EPR spectra.
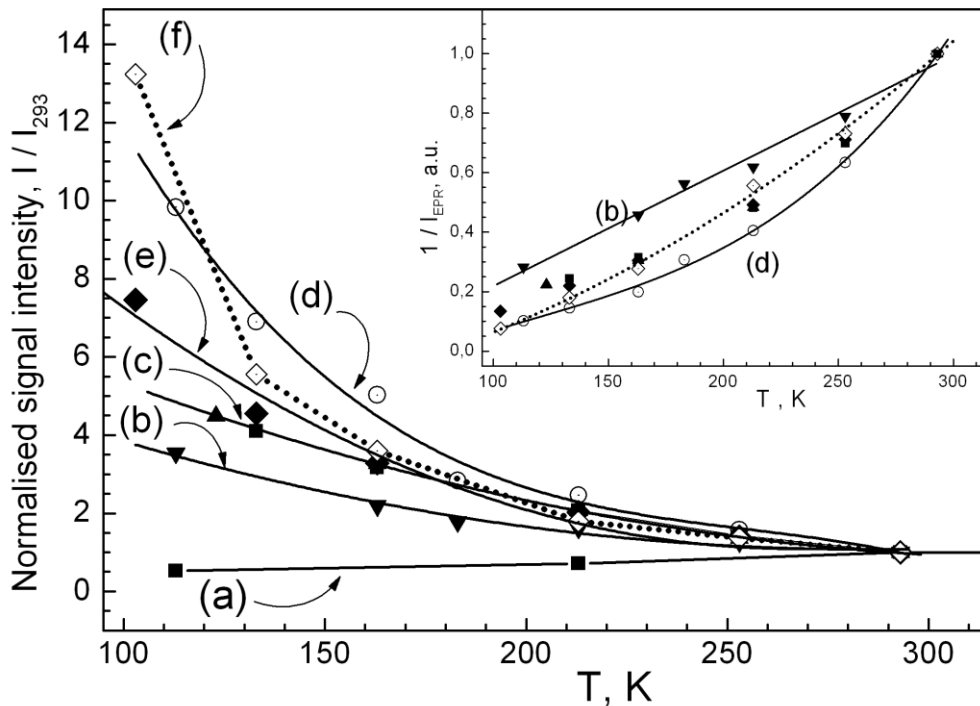
Figure 4.18. Temperature dependence of the signal intensity of pristine $FeSn_2$ and $FeSn_2$ electrodes at selected states of discharge (b,c,d,e) and recharge (g,f).

To assign the superparamagnetic resonance signal, the ^{57}Fe Mössbauer data on the decomposition of FeSn$_2$ during the electrochemical reaction are taken into account. Thus, we can attribute the EPR signal to iron particles in a superparamagnetic state. In addition, metal iron is able to accommodate small amounts of tin with preservation of its crystal structure [19]. Both α-Fe and Sn doped α-Fe are in ferromagnetic states. The average magnetic moment per Fe atom slightly increases from 2.22 to 2.3 μ_B after increase in Sn content from 0 to 5 at % Sn, and remains nearly constant between 5 and 25 at. % Sn [23]. This means that tin-containing iron particles in a superparamagnetic state can also give rise to the superparamagnetic resonance signal of the charged and discharged electrodes. From an EPR point of view, the differentiation between superparamagnetic iron and superparamagnetic tin-containing iron particles is a difficult task. Irrespective of the composition of the superparamagnetic particles, the relationship between the line width and the particle size has been established experimentally: the line width decreases with decreasing the particle size [24]. This dependence is valid only in the case when inter-particle magnetic interactions are absent. Hence, the important finding of EPR is the formation of superparamagnetic particles containing iron (or tin-iron) during the electrochemical reaction.

The changes in the EPR line width and the signal intensity with the discharge depth can be related with the variation of both the composition and the dimensions of the superparamagnetic particles. It is noticeable that nanoparticles with close size distribution start to form at the beginning of the discharge, where the solid-electrolyte interface is developed and most of FeSn$_2$ remains unreacted (Figs. 4.12, 4.14). This means that, at lower depth of discharge, the formation of superparamagnetic particles proceeds mainly on the particle surface. The signal intensity increases with the discharge depth, reaching a maximum at 457 mAh/g. For deeply discharged electrodes where Li$_x$Sn phases are formed, a "loss' of signal intensity is observed and size distribution becomes broader. This fact can be understood if we take into account that the amount of the tin impurities will affect the EPR response from the iron superparamagnetic particles. In addition, the EPR spectroscopy is sensitive towards the dimensions of the superparamagnetic particles [25]. This means that in the course of the electrochemical reaction a re-distribution of the superparamagnetic particles takes place leading to a particle growth and a loss in the EPR intensity. It is noticeable that the

121

formation of an electrochemically inactive "skin" of Fe on the surface of FeSn particles during the charge process has been established by ^{57}Fe and ^{119}Sn Mossbauer spectroscopy [26].

After the reverse process of recharge, the electrochemical reaction proceeds with participation of Li$_x$Sn phases. In the same sequence, the iron superparamagnetic particles are preserved. However, the small variation in the EPR line width and signal intensity implies for some changes in the amount of the incorporated tin in the iron nanoparticles (Fig. 4.17). It is noticeable that the changes in the particle composition are limited, which is evidenced by the similar temperature evolution of the EPR line width of fully discharged and fully charged electrodes (Fig. 4.15). In addition, the iron superparamagnetic particles remain sensitive whether the electrodes are fully or partially discharged. Henceforth, the EPR results agree with the existence of "spectators" iron particles which are not detected by XRD.

The proposed mechanism of interaction of nanocrystalline FeSn$_2$ with Li differs from that established for FeSn and CoSn$_2$-based electrodes [25, 27-28]. It has been found that during the discharge both FeSn and CoSn$_2$ are directly transformed into lithium-rich Li$_y$Sn phases and metallic Fe or Co nanoparticles, while, on charge, the 'liberated' Sn atoms can react again with Fe or Co to form ferromagnetic grains of Sn–Fe alloys [25] and modified CoSn$_2$ nanocompound (Li$_y$Co$_z$Sn$_2$ matrix), respectively [24]. For nanocrystalline FeSn$_2$-based electrodes studied by us, the electrochemically formed superparamagnetic iron particles are preserved even after the recharge process. Their role is to prevent the particle aggregation, thus improving the electrochemical performance of FeSn$_2$–based electrodes. The different mechanism reveals the effect of the nanodispersion when these materials are used as electrodes in lithium ion batteries.

4.2. FeSn$_2$-CoSn$_2$ solid solutions

4.2-1. Structure and morphology

The XRD patterns of the obtained Fe$_{1-x}$Co$_x$Sn$_2$ samples are shown in Fig. 4.19 Crystalline impurities are not observed. For x ≤ 0.5, the patterns are close to the XRD ICDD file n° 25-415 corresponding to FeSn$_2$ and can be indexed with tetragonal axis and in the space group I4/mcm (number 140). The compositions were obtained by EDAX analysis.
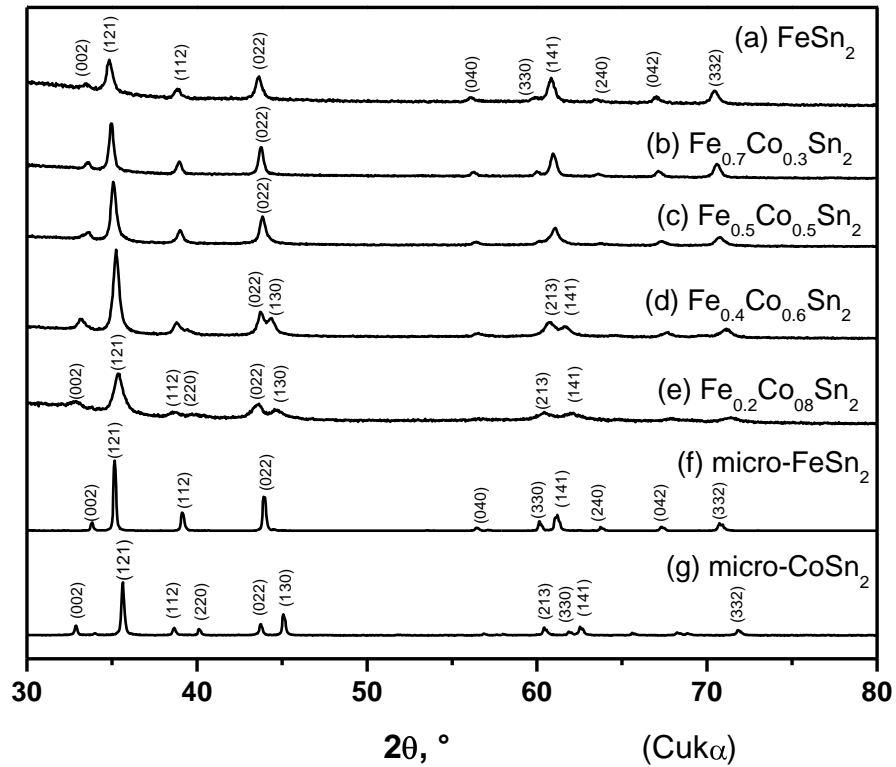
Figure 4.19. XRD patterns of nanometric Fe$_{1-x}$Co$_x$Sn$_2$ with x=0.0, 0.3, 0.5, 0.6 and 0.8. For the sake of comparison, the patterns for micrometric FeSn$_2$ and CoSn$_2$ are also shown in (f) and (g) respectively. The Miller indexes of the relevant reflections are indicated.

Pure nanocrystalline $CoSn_2$ could not be prepared under the selected experimental conditions. When x=1 was used as the starting composition, the resulting compound was $CoSn_3$. However, nano-$CoSn_2$ was obtained by a combination of the polyol method and ultrasonication (Fig. 4.20). Due to the broadening of the Bragg peaks observed for the nanometric particles (Fig. 4.19) and for comparison, the XRD patterns of micrometric $CoSn_2$ and $FeSn_2$ prepared at 490 °C are shown in Fig. 4.19f and g. Irrespective of the isomorphic character, the XRD patterns of $CoSn_2$ and $FeSn_2$ show certain differences, as a consequence of their different unit cell parameters. According to the ICDD file n° 25-256, two Bragg peaks are observed between 43 and 46°2θ for pure $CoSn_2$ which correspond to the reflections (022) and (130), while only one peak is resolved in this range for $FeSn_2$ (XRD file n°25-415). In addition, the (220) reflection is observed for $CoSn_2$ at 40.1° 2θ, but it is not detected for $FeSn_2$, and this is also in good agreement with XRD files numbers 25-415 and 25-256.
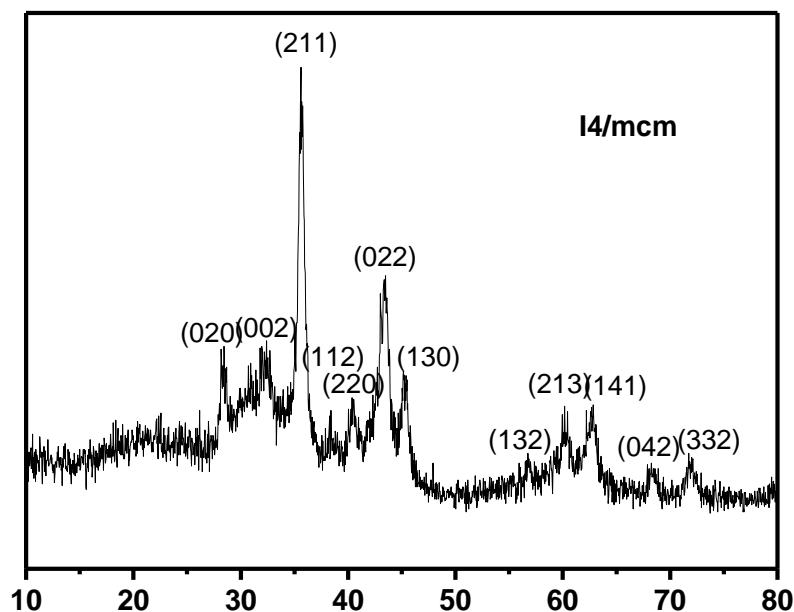
Figure 4.20. XRD pattern of nano-$CoSn_2$ obtained by a combination of the polyol and sonochemical methods. The miller indices are indicated.

The obtained nanometric $Fe_{1-x}Co_xSn_2$ samples show XRD patterns intermediate between $CoSn_2$ and $FeSn_2$. The refinement by using the peaks positions leads to the lattice cell parameters that are shown in Fig. 4.21. For the sake of comparison the data from ICDD files are also included in Fig. 4.21. For $FeSn_2$ (ICDD file n° 25-415), a=6.539 and c=5.325 Å. For $CoSn_2$ (ICDD file n°25-256), a=6.363 and c=5.456 Å. Hence, the influence of the stoichiometry (x-value) on the lattice cell parameters is complicated by the feature that $a(FeSn_2)>a(CoSn_2)$ but $c(FeSn_2)<c(CoSn_2)$. The atomic radius of Co (125 pm) is slightly smaller than the corresponding of Fe (126 pm) [29] and a small linear decrease of the unit cell volume is expected according to the Vegard's law. Such behaviour is experimentally observed when cobalt content increases in nano-$Fe_{1-x}Co_xSn_2$ solid solutions (Fig. 4.21B). The lattice parameter a decreases on increasing cobalt content while the observed evolution of the c lattice cell parameter is more complex. Below x = 0.5 the c parameter slightly decreases with cobalt content and from x > 0.5 to x = 0.8 increases. The deviations of the Vegard's law are usual [30].
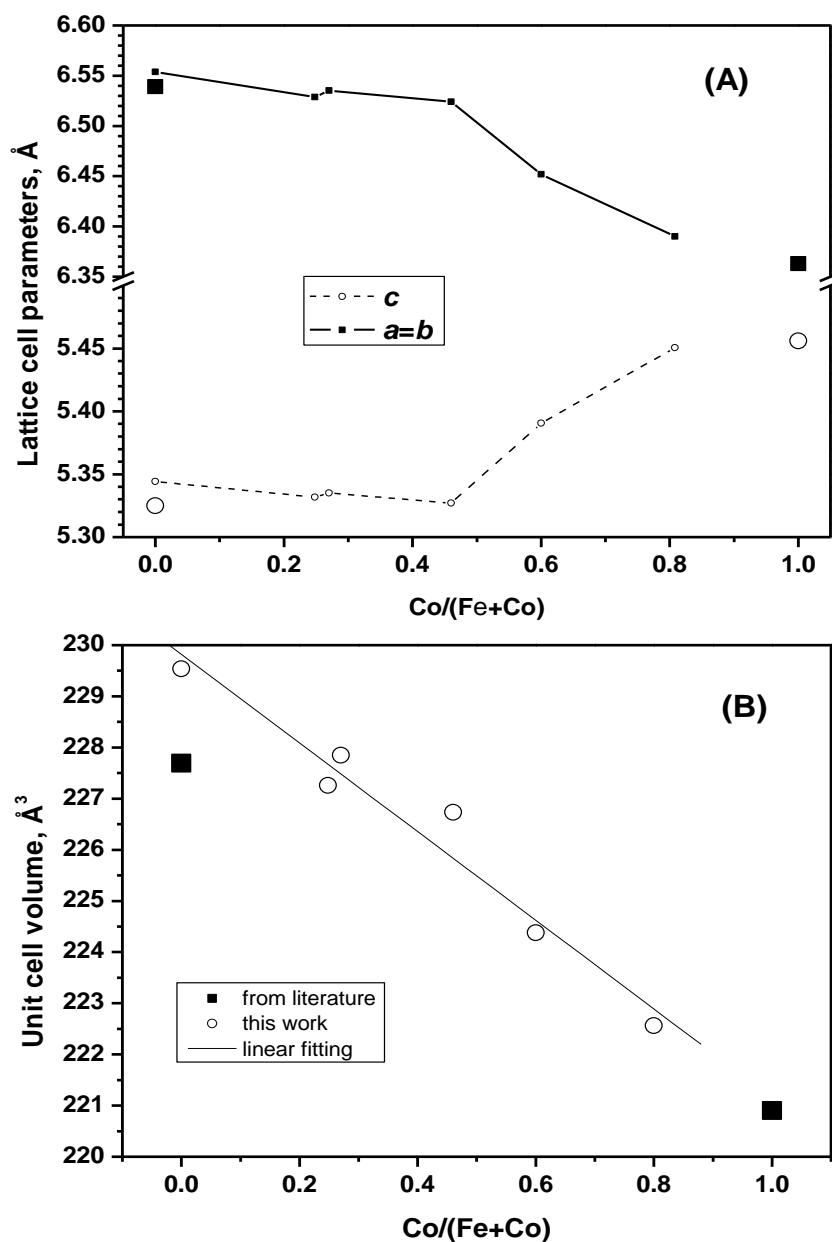
Figure 4.21. (A) Evolution of the tetragonal lattice cell parameters as a function of cobalt content in nanocrystalline $Fe_{1-x}Co_xSn_2$. The parameters taken from the literature for pure $FeSn_2$ (XRD file nº 25-415) and $CoSn_2$ (XRD file nº25-256) are also shown like bigger points. (B) Volume of the unit cell and linear fitting of the obtained experimental data. The volume cell values taken from the literature are represented by the symbol ■.The lattice cell parameters were calculated using the CellRef program.

The unit cell parameters and volumes obtained by Rietveld refinement (Fullprof program) are shown in Fig. 4.22. Nano-$CoSn_2$ obtained by ultrasonication is also included in this figure. The contraction of the unit cell volume that is observed when the cobalt content increases in the $FeSn_2$-$CoSn_2$ solid solutions is in line with a stronger chemical bond in the Co-rich compounds. Thus, it is known that cobalt has greater ability to alloy with tin than iron [31]. On the other hand, the heating at 490°C of a mixture of Fe, Co and Sn powders yielded to the formation of a mixture of phases such as Sn, $FeSn_2$ and $CoSn_2$. All these results evidence that the polyol method and the combination of the polyol and the sonochemical methods are very adequate to obtain nanocrystalline $Fe_{1-x}Co_xSn_2$ particles at the laboratory scale.
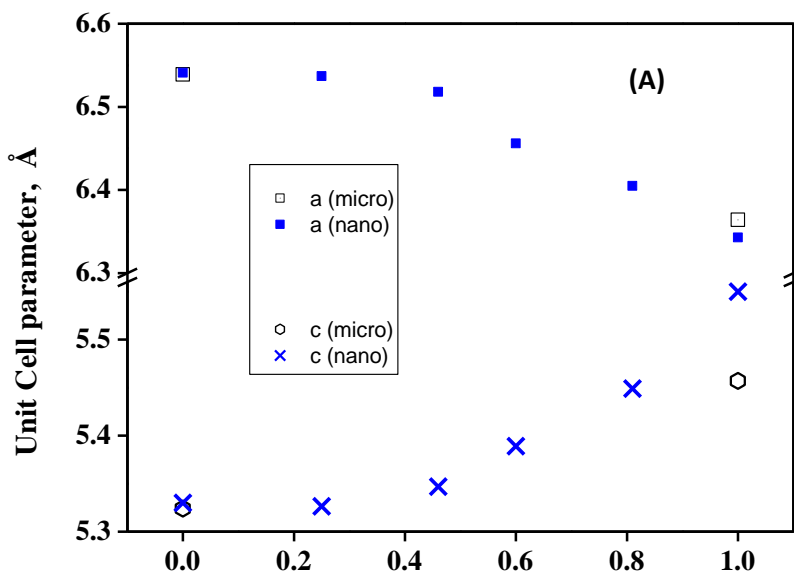
Figure 4.22. Continued in next page.
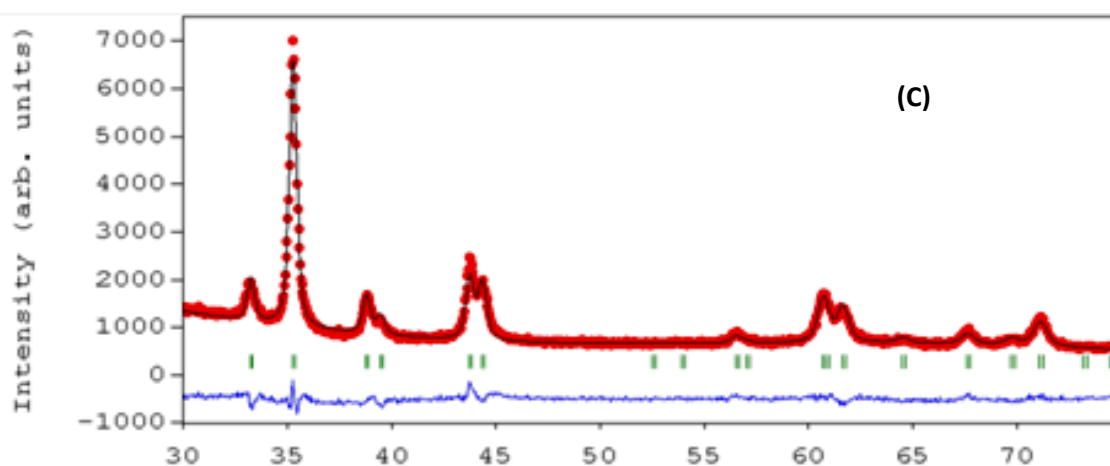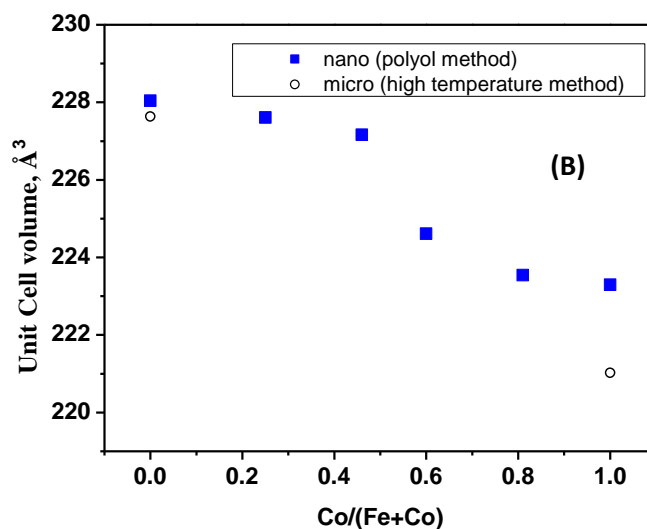
Figure 4.22. (A) Unit cell parameters (*a, c*) and (B) unit cell volumes obtained by Rietveld refinements of the XRD patterns for $Fe_{1-x}Co_xSn_2$ solid solutions obtained by the polyol method (named "nano"). For the sake of comparison, the results corresponding to $CoSn_2$ and $FeSn_2$ obtained at high temperature (490°C) are also shown (named "micro"). (C) Selected Rietveld refinement for $Fe_{0.5}Co_{0.5}Sn_2$.

Selected TEM images of $Fe_{1-x}Co_xSn_2$ are shown in Fig. 4.23. The particle size is in the order of 20 nm. Lattice fringes are observed. The observed nanocrystals have morphologies of cubes, rounded-cubes, U-shaped and nanorod dimers. A poorly crystalline shell surrounds the intermetallic particles that may be due to a XRD-undetected SnO_x layer. All these observations are consistent with the previous studies on nanocrystalline $FeSn_2$, where a mechanism based on the Kirkendall effects was proposed for the formation of the nanoparticles [32]. The cubic particles of β-Sn are formed first and serve as seeds for the growth of intermetallic particles. Iron and cobalt formed under reducing conditions diffuse into the tin particles. The different diffusion rates of the Sn, Co and Fe atoms can cause the occurrence of voids in the intermetallic particles and formation of nanorods, particularly in the case of β-Sn seeds larger than 30 nm. The smaller cube shaped β-Sn (<15 nm) seeds transform to dense intermetallic particles (not hollow) preserving their cubic form [32].
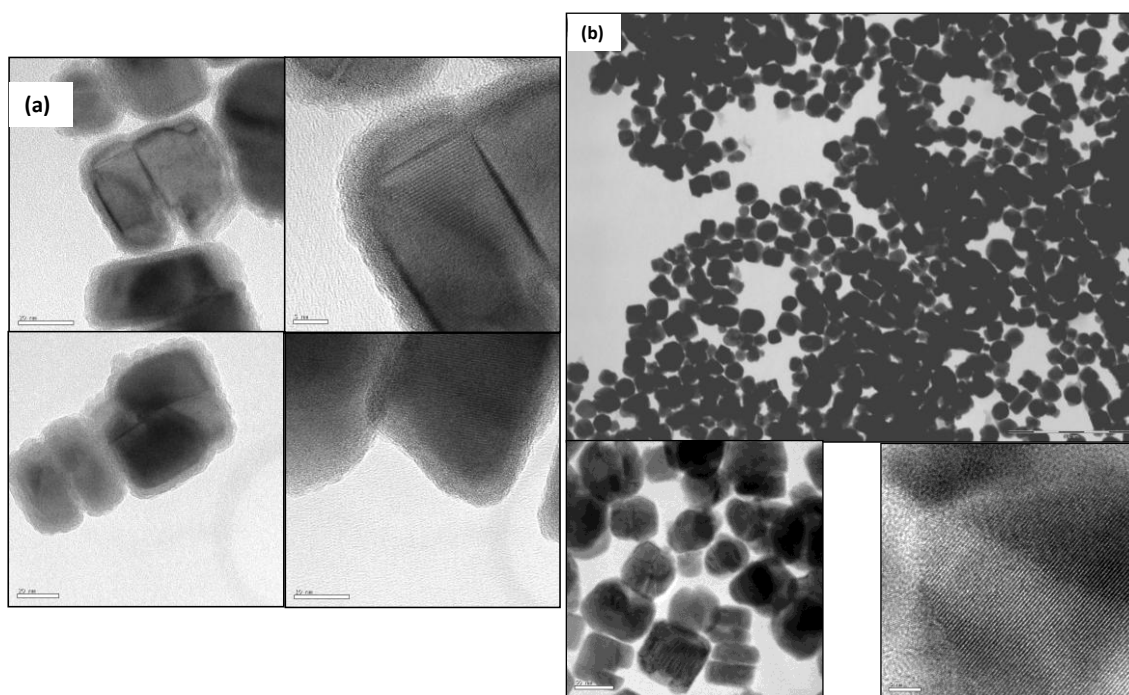
Figure 4.22. Selected TEM images for (a) $Fe_{.0.8}Co_{0.2}Sn_2$ and (b) $Fe_{0.5}Co_{0.5}Sn_2$.

In the case of nano-CoSn$_2$ obtained by a combination of the polyol and ultrasonication method, the nanoparticles exhibit more irregular morphologies [33] (Fig. 4.24).
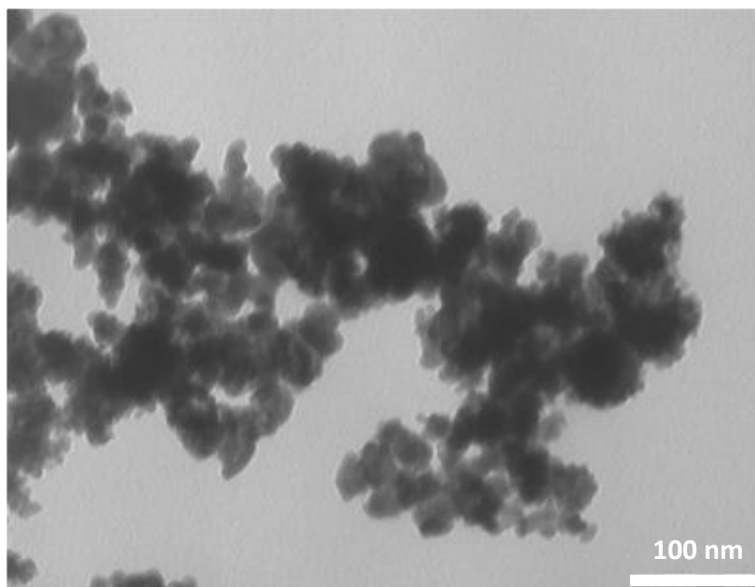
Figure 4.24. TEM micrograph of CoSn$_2$ obtained by a combination of the polyol and the sonochemical methods.

The nanometric character and the composition of the nano-Fe$_{1-x}$Co$_x$Sn$_2$ samples influence the ^{119}Sn and ^{57}Fe Mössbauer spectra. Thus, the hyperfine magnetic fields are not present, in contrast to microscrystalline FeSn$_2$ [6], indicating the superparamagnetic character of the studied samples. Irrespective of the low intensity of signals for samples with low iron-content, the room temperature ^{57}Fe Mössbauer spectra (Fig. 4 .25) of all the nanosized Fe$_{1-x}$Co$_x$Sn$_2$ samples are rather similar and can be ascribed to a superparamagnetic singlet, as was previously described for nano-FeSn$_2$ [34, 35]. In contrast, microcrystalline FeSn$_2$ shows a sextuplet signal at room temperature due to long range magnetism [2, 3]. In FeSn$_2$, each iron atom is in a high symmetry site and is surrounded by eight tin atoms at the corners of a square antiprism. Trumpy et al. found that in the iron-tin system, the electron densities are reduced at all the nuclei with

respect to the pure metals, and the isomer shifts were linearly related to the number of Fe-Sn bonds in such a way that bonding reduces the electron densities at both nuclei [6]. The distances between the atoms in the alloys also contribute to the change of the isomer shift. The ^{57}Fe isomer shift tends to decrease when the iron content decreases and the cobalt content increases (Fig. 4.26). This result indicates that the electron density between Fe and Sn increases when the amount of cobalt increases suggesting that the Fe-Sn bond becomes stronger, in good agreement with the observed decrease of the lattice cell parameters. The sample with x= 0.8 shows certain deviation from the general tendency, but it is within the experimental error due to the lower iron content and poorer crystallinity of this sample. The low crystallinity can decrease the Lamb-Mössbauer factor and can result in some uncertain behaviour. Otherwise, the increase of the c-lattice cell parameter from x =0.5 to x =0.8 may be related to the relative increase of the ^{57}Fe isomer shift.
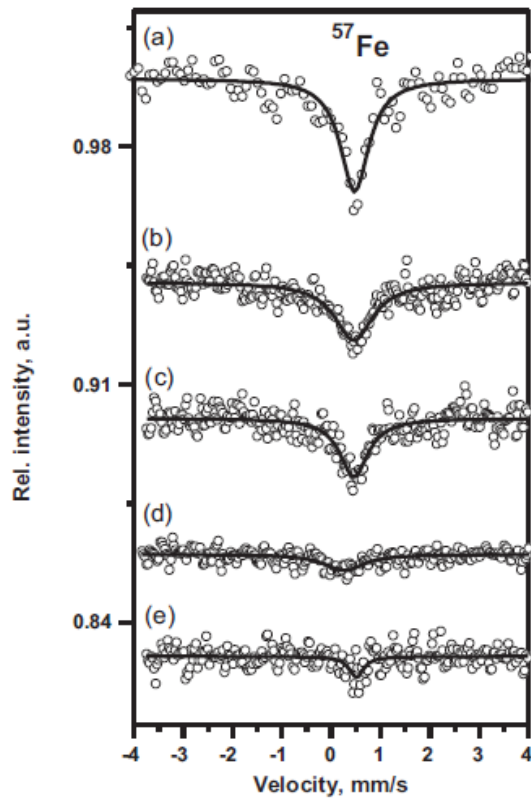
Figure 4.25. Room temperature ^{57}Fe Mössbauer spectra for nanocrystalline $Fe_{1-x}Co_xSn_2$ with x equals to 0.0 (a), 0.25 (b), 0.3 (c), 0.5 (d), 0.8 (e).
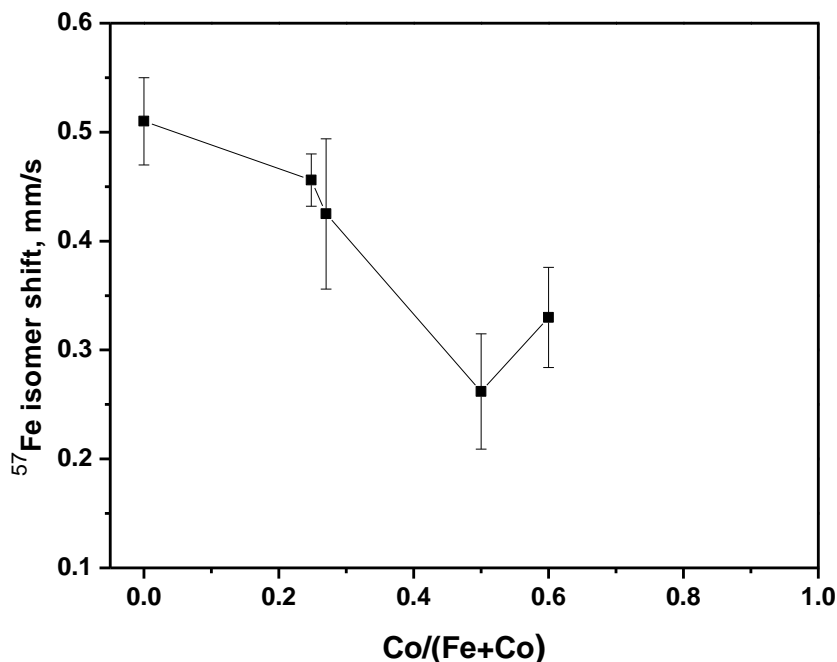
Figure 4.26. ^{57}Fe isomer shift as a function of cobalt content for $CoSn_2$-$FeSn_2$ solid solutions

4.2-2. Thermal analysis

It has been shown above that the nanoparticles of $FeSn_2$ show a higher tendency to be oxidized in air atmosphere in comparison with larger particles [32]. In order to study the reactivity of $CoSn_2$, the DTA curves of micro-$CoSn_2$ and nano-$CoSn_2$ have been recorded (Fig. 4.27).

Micro-$CoSn_2$ is thermally decomposed in the first heating under Ar-flow or in static air atmosphere (Fig. 4.27-top), being in good agreement with the phase diagram ($CoSn_2 = CoSn + L$). However, nano-$CoSn_2$ (Fig. 4.27-bottom) is oxidized in both static air atmosphere and Ar-flow (as due to traces of O_2). While the exothermal oxidation of nano-$CoSn_2$ under Ar-flow starts at around 300°C, the oxidation of nano-$FeSn_2$ starts at around 200°C [32]. The formation of SnO_2 after DTA experiments was corroborated by XRD. In fact, the pristine nanometric particles of pristine $Fe_{1-x}Co_xSn_2$ samples usually are covered by a thin layer of amorphous tin oxide as was confirmed by HRTEM and

^{119}Sn Mössbuer spectroscopy results. As a conclusion, nano-MSn_2 compounds have greater surface reactivity (oxidation) than micro-MSn_2 as expected for the large external surface of the particles, and nano-$FeSn_2$ has greater surface reactivity than nano-$CoSn_2$ as expected for the stronger Co-Sn chemical bond. This surface layer can influence the electrochemical behaviour.
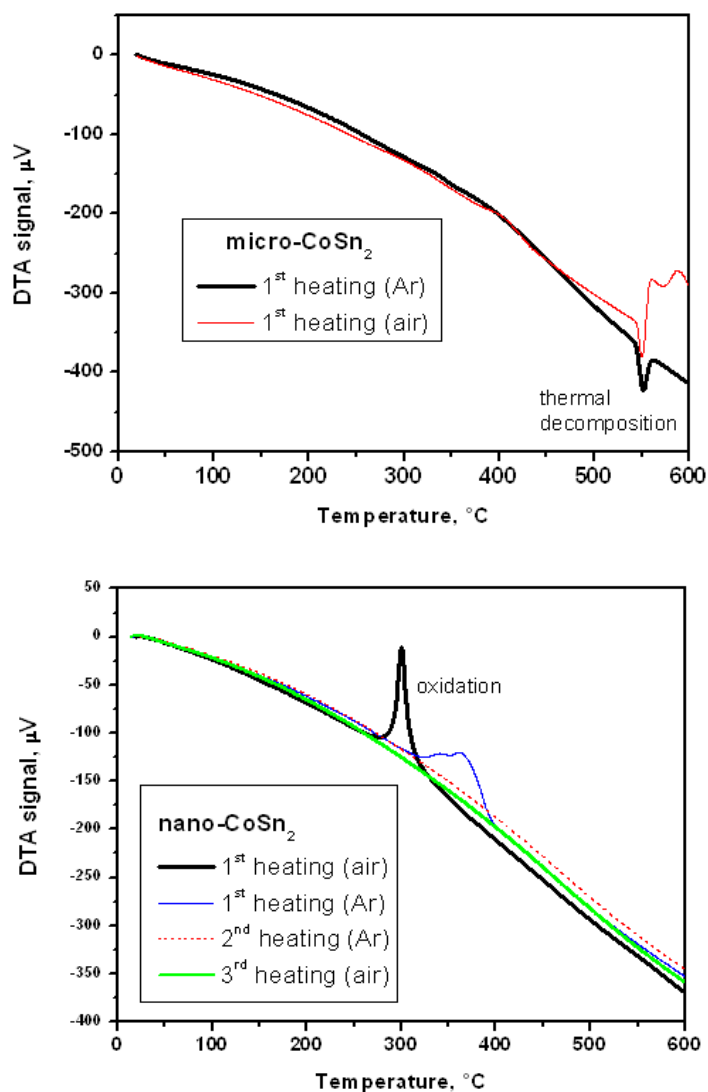
Figure 4.27. DTA curves for $CoSn_2$ obtained at 490°C ($CoSn_2$) and following the combination of the polyol and sonochemical method (nano-$CoSn_2$)

4.2-3. Electrochemistry

The electrochemical behaviour of nano-$Fe_{1-x}Co_xSn_2$ was studied in lithium test cells. For the sake of comparison, the capacity retention of microcrystalline $CoSn_2$ and $FeSn_2$ materials are shown in Fig. 4.28, and very poor capacity retention is observed in both cases.
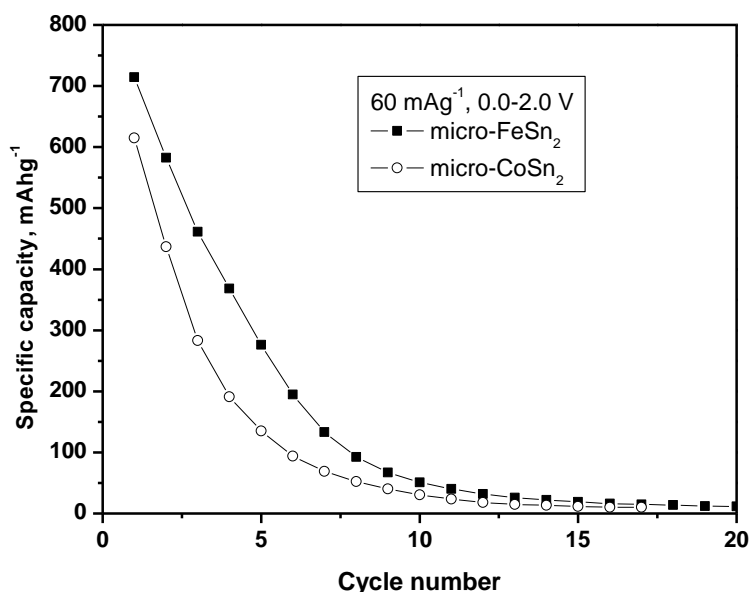
Figure 4.28. Specific capacity as a function of cycle number for microcrystalline $FeSn_2$ and $CoSn_2$ in lithium test cells.

It has been reported that isostructural $CoSn_2$ and $FeSn_2$ have tunnels between the Sn atoms in their structure, where Li can penetrate to initiate the reaction and form Li_xSn alloys, but the facility of lithium intercalation is dependent on particle size [36]. Due to the insertion and extraction of lithium, the large particles of alloys can suffer abrupt volume changes, swelling and break-up, yielding to the occurrence of electrically disconnected particles and battery failure. Irrespective of the fact that capacity retention of all the samples are significantly influenced by the experimental condition, the best

134

electrochemical behaviour of the nano- $Fe_{1-x}Co_xSn_2$ samples (Fig. 4.29) is much better than the corresponding micro-$CoSn_2$ and micro-$FeSn_2$ (Fig. 4.28). The best electrochemical behaviour is observed for x =0.5, with maximum capacities values above 500 mAh g^{-1} after 30 cycles. More probably, the simultaneous presence of two transition metals and the nanometric character improves the metallic glass-forming ability, avoids the crystal growth and improves the cycling stability. Several current intensities and potential windows have been tested. At 60 mAg^{-1} of mass-normalized current intensity, the capacity retention is improved when the upper potential limit is decreased from 2.0 to 1.5 V. The initial capacity is higher at 30 mAg^{-1} than at 60 mAg^{-1} (in the 0.0-2.0 potential window), but the capacity fades more rapidly at 30 mAg^{-1}. In conclusion, capacity retention improves when the upper potential limit is decreased from 2.0 to 1.0 and the current intensity is increased from 30 to 80 mAg^{-1}. Most probably, the higher current intensities decrease the extension of irreversible processes and lead to better cycling stability. The electrochemical behaviour of nano-$Fe_{1-x}Co_xSn_2$ could be further improved by using a carbonaceous matrix and by optimization of the binding agent
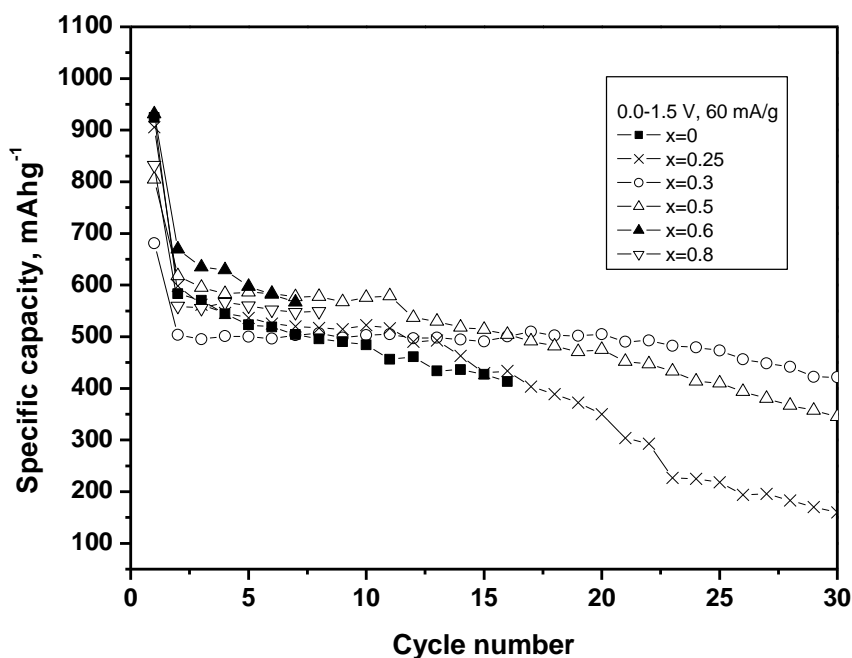
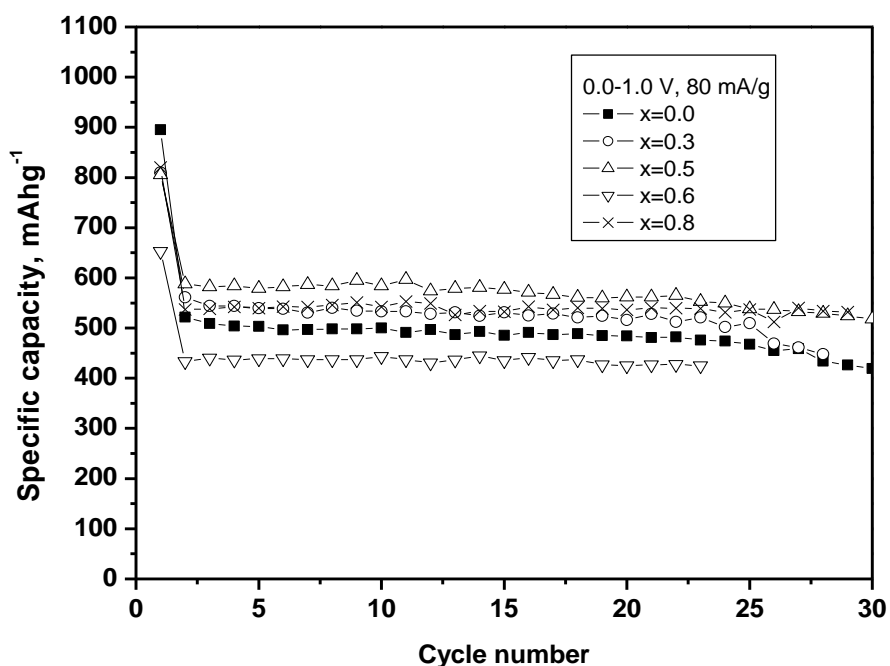**Figure 4.29.** Continued in next page.
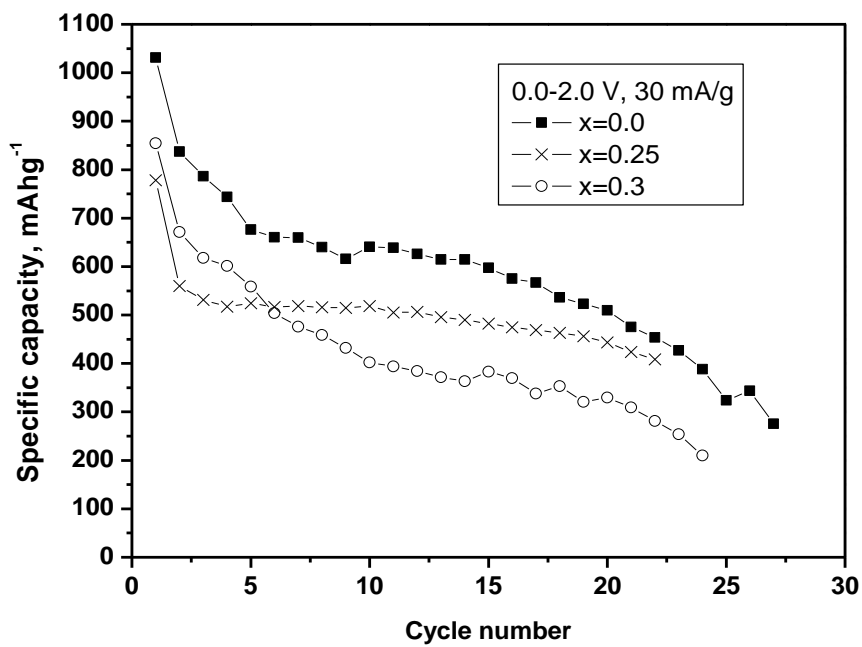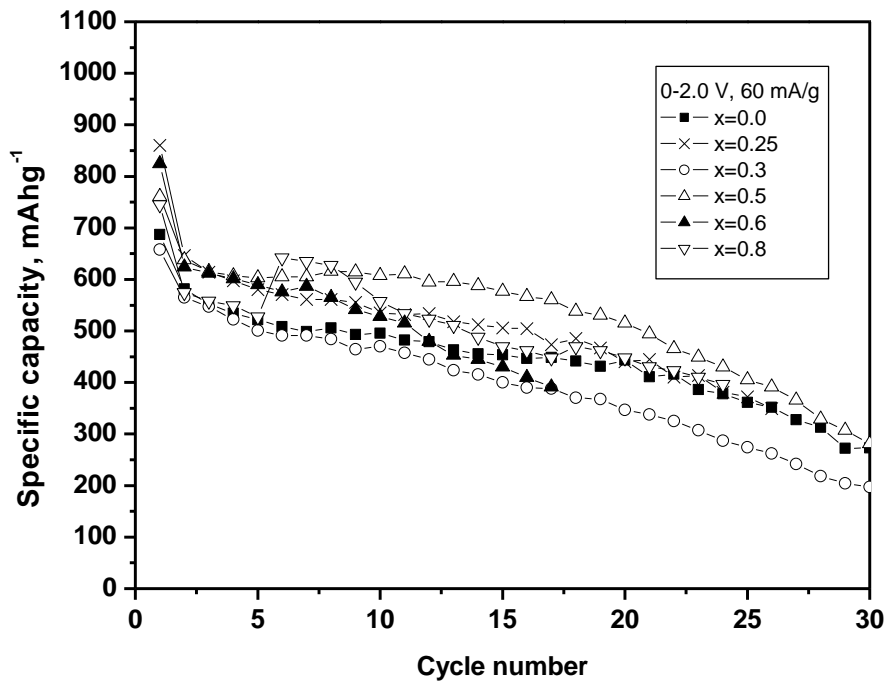
Figure 4.29. Continued in next page

Figure 4.29. Specific capacity as a function of cycle number for $Fe_{1-x}Co_xSn_2$ in lithium test cells under several experimental conditions.

The potential-capacity curves corresponding to the first and second discharge-charge cycle of representative nanometric samples are shown in Fig. 4.30. All the nano-$Fe_{1-x}Co_xSn_2$ samples have rather similar discharge-charge profile. These nanometric samples and the micrometric $CoSn_2$ [28, 36] and $FeSn_2$ [11] samples do not differ greatly in the potential-capacity profiles. However, the surface reactions would be more extensive for very small particles. The reaction between lithium and amorphous oxide layer through conversion reaction and formation of a solid electrolyte interphase (SEI) [35] can contribute to the irreversible capacity of the first cycle and to decrease the coulombic efficiency. The irreversible formation of Li_2O and SEI would be more extended for the very small particles. Thus, the efficiency for the first cycle of nano-$Fe_{0.5}Co_{0.5}Sn_2$ in Fig. 4.30 is 76%, and the efficiency observed for micro-$FeSn_2$ and

micro-CoSn$_2$ is 82% and 79%, respectively. Zhang and Xia previously reported a coulomb efficiency of 85% for micro-crystalline CoSn$_2$ [36]. The higher reactivity of the surface (SEI formation) for nano-FeSn$_2$ in comparison with micro-FeSn$_2$ has been recently reported elsewhere [37]. On the other hand, the formation of a Li$_2$O matrix after the reaction between surface oxide and lithium may contribute to buffer the volume change during the process of lithium insertion-extraction in the metallic particles, and to improve the capacity retention upon cycling of the nanoparticles. In addition, the destruction of the Li$_2$O matrix at the upper potential limit around 2 V may lead to strong fade upon cycling (Fig. 4.29). The main problem of the initial irreversible capacity would be the consumption of lithium from the positive electrode in a lithium ion battery.
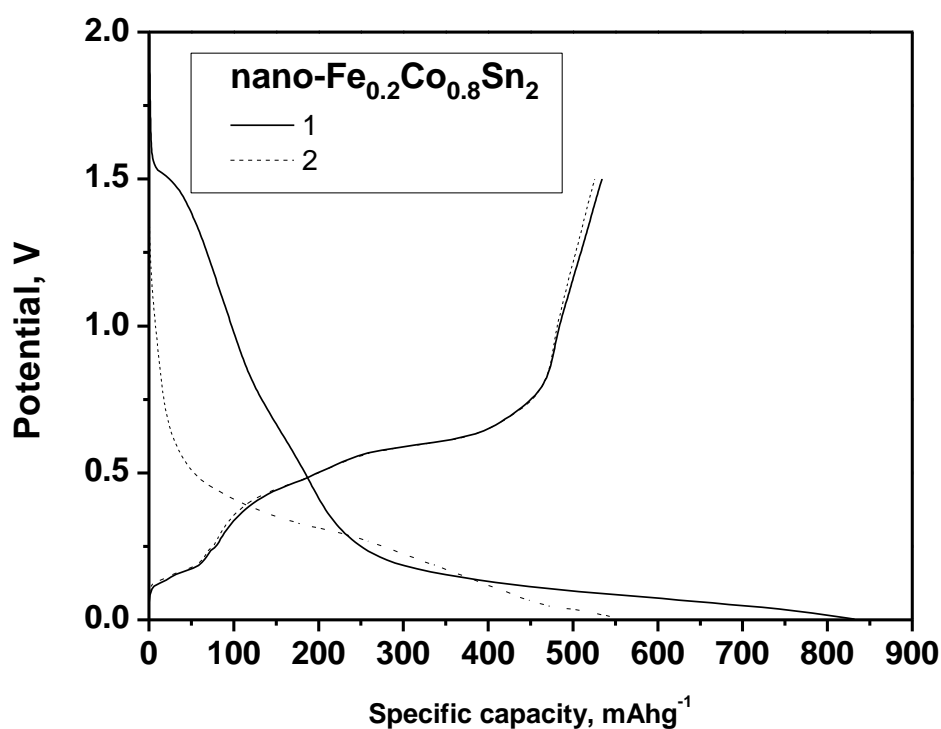
Figure 4.30. Continued in next page.
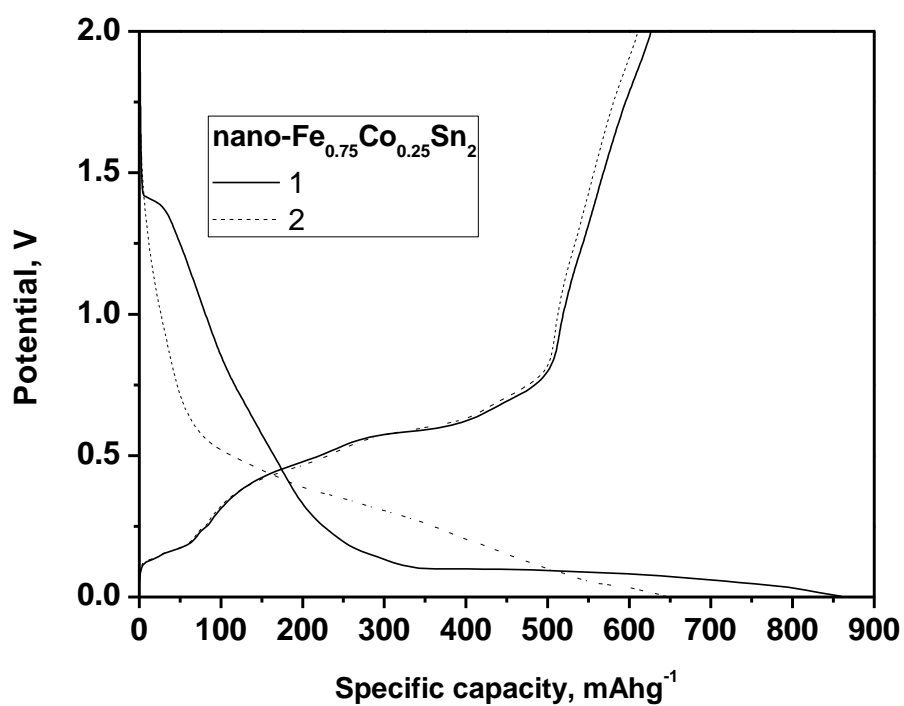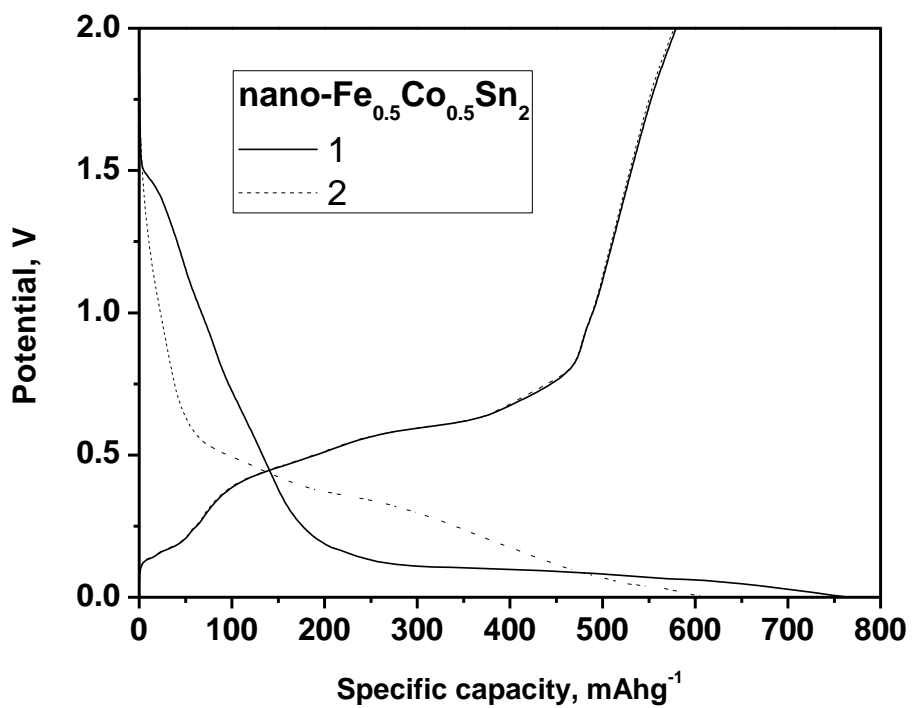
Figure 4.30. Potential-capacity plots of selected samples.

The derivative plots (dQ/dV vs. potential) for x=0.3 and x=0.5 are shown in Fig. 4.31 and can be used to explore the electrochemical reactions. An irreversible peak at around 1.4 V is observed in the first discharge process that can be ascribed to formation of passivating surface film or solid electrolyte interface (SEI). The main reaction of the first discharge is observed as a very intense peak located below 0.2 V. After the first cycle, the derivative curves remain almost without change, suggesting the good stability of the electrode active material. The occurrence of Li_xSn alloys is observed as a peak at ca. 0.38 V in the successive discharges and several peaks at 0.45, 0.6 and 0.75 V in the charge processes. The $Fe_{1-x}Co_xSn_2$ samples with iron in their composition, as well as $FeSn_2$ [37], exhibit peaks in the first charge (0.6 V) and second discharge (0.4 V) that are ascribed to formation of Li_xSn phases. In contrast, the cobalt-tin phases CoSn [38], $CoSn_2$ [27, 28] and $CoSn_3$ [8] do not show these narrow peaks. Hence, the iron-cobalt sample forms Li-Co-Sn alloys or form very small grains of Li-Sn alloys that interact with Co atoms. However, the iron-containing samples have greater tendency to form crystalline grains of Li_xSn phases. It is noteworthy that cobalt and tin have strong tendency to form amorphous alloys [39, 40]. It seems that the simultaneous presence of two transition metals (x=0.5), one of them (Co) with greater ability to alloy with Sn and another (Fe) with lower ability to alloy with Sn, favours a better electrode stability.
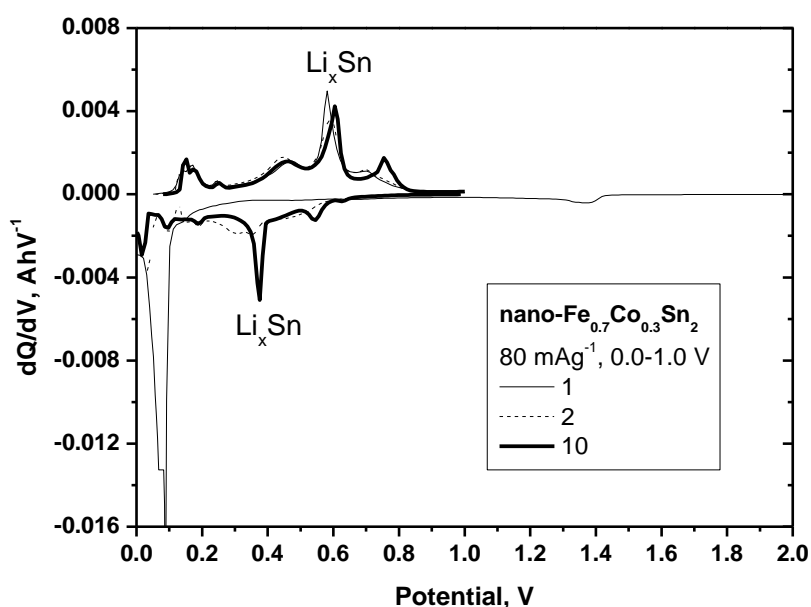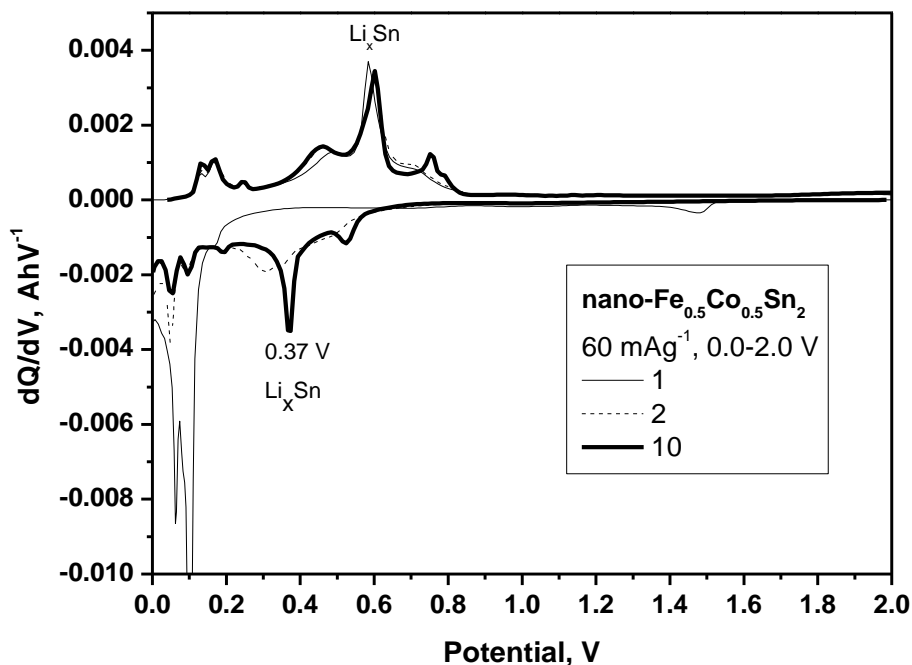

Figure 4.31. Continued in next page.

Figure 4.31. Selected derivative curves for cycles number 1, 2 and 10.

4.2-4. Reaction Mechanism

The electrodes of nano- $FeSn_2$, nano-$CoSn_2$ and nano- $Fe_{1-x}Co_xSn_2$ discharged to 0.0 V vs Li/Li^+ were used for ex-situ studies. The XRD pattern obtained after the electrochemical reaction between nano-$FeSn_2$ and Li shows a broadened reflection corresponding to $Li_{22}Sn_5$ while the reflections of pristine $FeSn_2$ are not observed (Fig. 4.32Ac). The occurrence of superparamagnetic Fe nano-particles was inferred above from Mössbauer and EPR data [11]. Henceforth, the initial structure of $FeSn_2$ is destroyed throughout reaction with Li, iron is extruded and Li and Sn form nanocrystalline intermetallics. When the relative cobalt content increases, and the iron content decreases, the relative intensity of the $Li_{22}Sn_5$ reflection decreases. Thus, the

occurrence of $Li_{22}Sn_5$ is not observed for nano-$CoSn_2$ discharged to 0.0 V, while reflections of $CoSn_2$ are still observed (Fig. 4.32A). Due to the strong Co-Sn interactions and the observed XRD pattern, the partial reconstruction of the $CoSn_2$ phase after the first discharge is not ruled out. For $Fe_{0.5}Co_{0.5}Sn_2$ an intermediate behaviour is observed, and reflections corresponding to $Li_{22}Sn_5$ and MSn_2 are observed in the discharged electrode material (Fig. 4.32Bb). These results are in good agreement with the stronger Co-Sn interactions and higher tendency to form Co-Sn amorphous alloys in comparison with Fe-Sn. After the first discharge-charge cycle of $CoSn_2$ (Fig. 4.32B) and $Fe_{0.5}Co_{0.5}Sn_2$ (Fig. 4.32C), a low-intensity and broadened reflection at ca. $36°2\theta$ corresponding to $CoSn_2$ is observed. A low-intensity and narrower reflection at ca. $35.1°2\theta$ probably corresponding to unreacted nanocrystalline $FeSn_2$ is observed after the first discharge-chare cycle of $FeSn_2$ (Fig. 4.32D), although a partial reconstruction of the $FeSn_2$ structure is not completely ruled out [33].
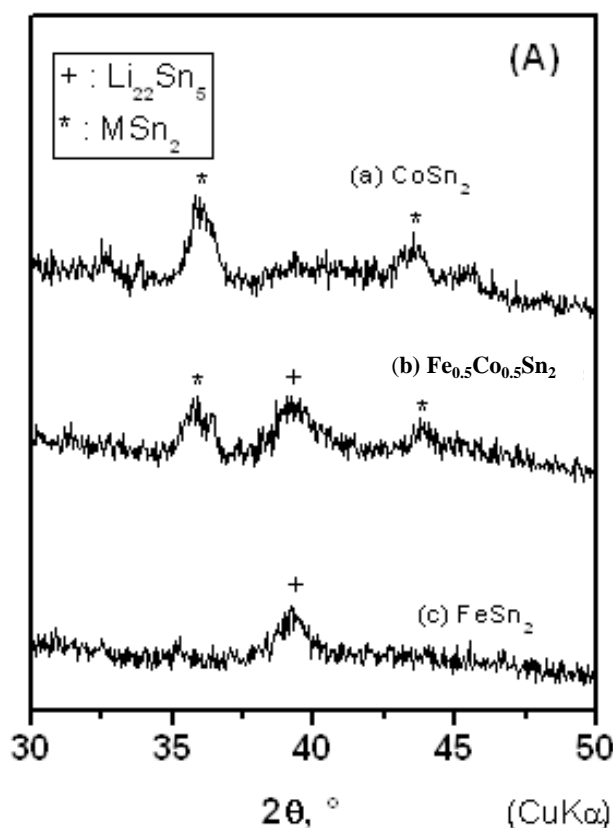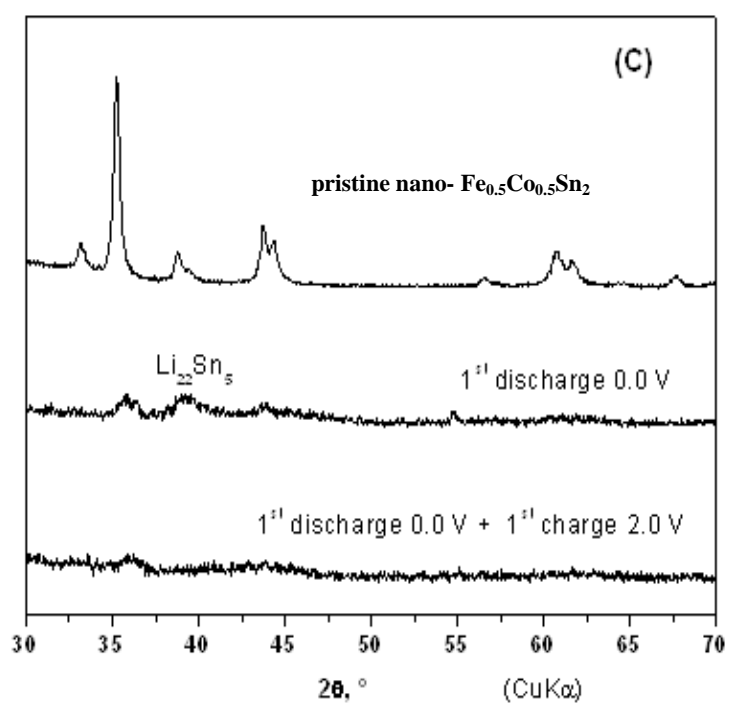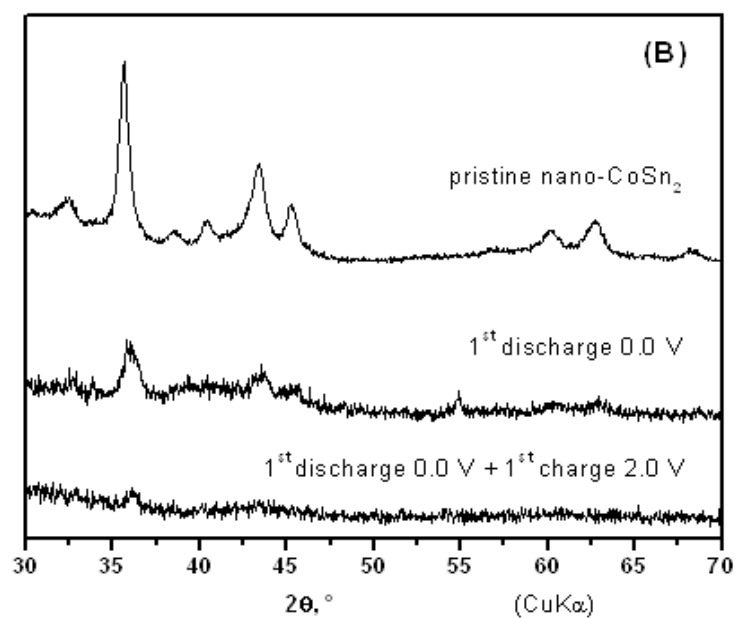

Figure 4.32. Continued in next page.
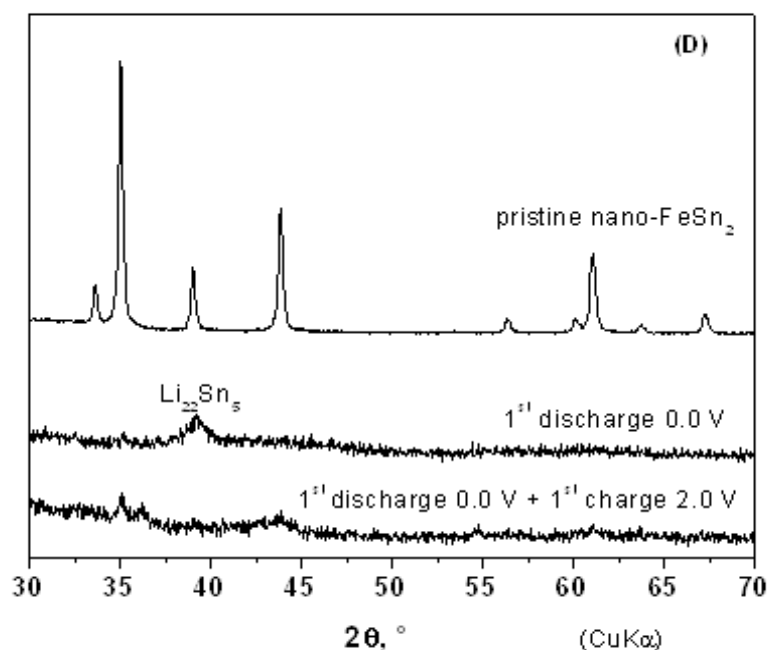
Figure 4.32. Continued in next page.

Figure 4.32. Ex-situ XRD patterns. (A) A detailed view after the first discharge (0.0 V vs. Li$^+$/Li) of CoSn$_2$, Fe$_{0.4}$Co$_{0.6}$Sn$_2$ and FeSn$_2$. Pristine material discharged electrode and charged electrode for (B) CoSn$_2$, (C) Fe$_{0.5}$Co$_{0.5}$Sn$_2$ and (D) FeSn$_2$. All these three samples were obtained by combination of the polyol and the sonochemical method.

In the derivative product of the second discharge (Fig. 4.33), the Li-alloying peak is shifted to lower potential (from ca. 0.9 V to ca. 0.2 V). This result supports the stronger Co-Sn interactions in comparison with Fe-Sn interactions in the lithiated electrode. Micro crystalline materials show narrower peaks in both charge and discharge processes. The occurrence of amorphous alloys with general formula Li$_x$Sn-Co is favoured by the small particle size, large external particle surface and easy Co-Sn alloying. According to these results and previous studies [41], for the intermediate compositions in the FeSn$_2$-CoSn$_2$ system, the simultaneous occurrence of Li$_x$Sn-Co, Fe and Li$_x$Sn at 0.0 V vs. Li$^+$/Li is hypothesized.

Thus, the following equations are proposed for the electrochemical reactions between nanocrystalline Fe$_{1-x}$Co$_x$Sn$_2$ and Li:

$$FeSn_2 \xrightarrow{Li} 2Li_xSn + Fe \qquad \text{(mainly irreversible)}$$

$$Li_xSn + Fe = xLi + Sn + Fe \qquad \text{(reversible)}$$

$$CoSn_2 \xrightarrow{Li} 2Li_xSn\text{-}Co \qquad \text{(mainly irreversible)}$$

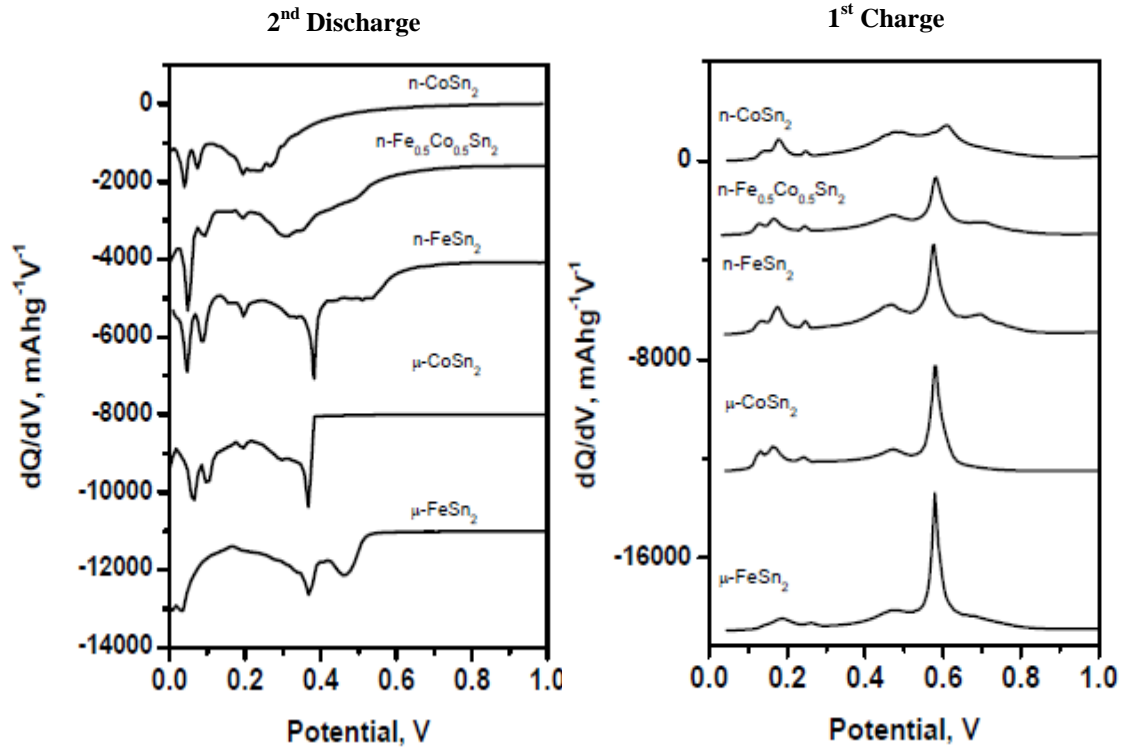$$Li_xSn\text{-}Co = xLi + Co\text{-}Sn \qquad \text{(reversible)}$$
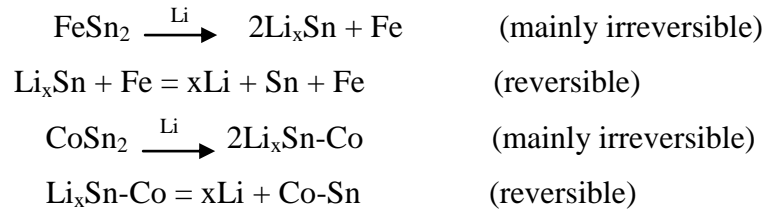

Figure 4.33. Differential capacity plots for the first charge (right) and second discharge (left) vs. lithium of different tin intermetallic compounds [42].

In general, as compared with bulk materials, tin-based intermetallics with very small particle size can exhibit giant improvements in their electrochemical properties versus lithium. Small particles are capable of buffering the lattice volume changes due to the lithium insertion-extraction from the electrode. In addition, the nanometric particles have low diffusion path lengths and exhibit better rate performance [42].

145

4.3. Nano-FeSn$_2$/ Polyacrylonitrile (PAN) composite.

In order to try to improve the electrochemical behaviour of MSn$_2$ phases, FeSn$_2$-PAN composite material was prepared.

4.3-1. Structure and morphology

The sample obtained by using the combination of polyol and sonochemical methods (method A) shows an XRD pattern (Fig. 4.34a) corresponding to nanocrystalline FeSn$_2$. Impurities are not observed. The crystallite size obtained by applying the Scherrer equation is Lc= 29 nm. The sample obtained by adding PAN, according to method B, exhibits reflections corresponding to FeSn$_2$ (main phase with Lc= 25 nm) and β-Sn (minor phase) is also observed (Fig. 4.34b).
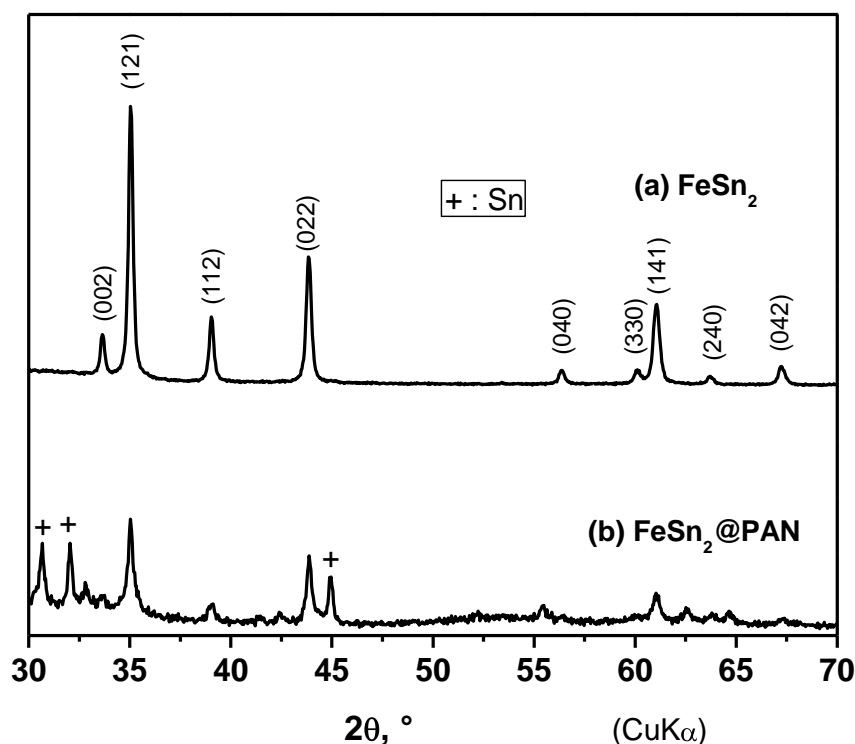

Figure 4.34. XRD patterns for (a) FeSn$_2$ and (b) FeSn$_2$@PAN.

The relative amount of Sn to $FeSn_2$ obtained by using the method of controlled additions and the intensity of the Bragg reflections is 15.4% wt [31] (Fig. 4.35). This sample will henceforth be referred to as $FeSn_2$@PAN. In the case that no ultrasound irradiation was applied (method C) the main XRD reflections were due to Sn, while only traces of $FeSn_2$ were found, as it was reported by Nacimiento et. al [31]. According to the carbon-nitrogen analysis results, $FeSn_2$@PAN contains 16.1% wt. of PAN, and the sample Sn-PAN contains 20.4% wt. of PAN.
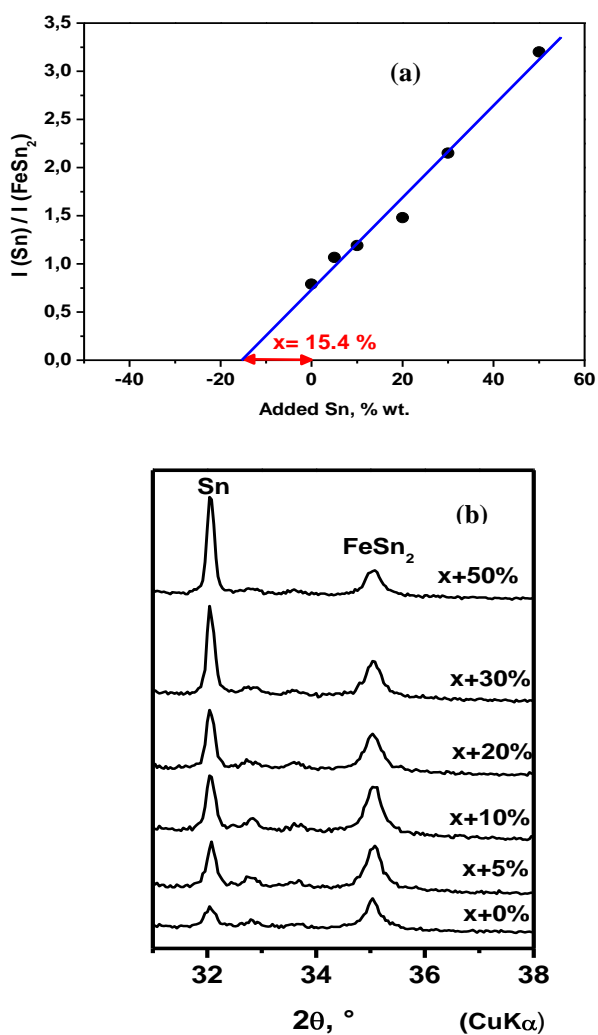

Figure 4.35. Calculation of the relative amount of Sn to $FeSn_2$ obtained by controlled addition method. (a) Ratio between the Bragg reflections vs. amount of Sn. (b) XRD patterns.

The TEM micrograph of FeSn$_2$@PAN shows that the PAN-phase surrounds the metallic nanoparticles (Fig.4.36). The FTIR spectrum of FeSn$_2$@PAN confirms the presence of PAN.
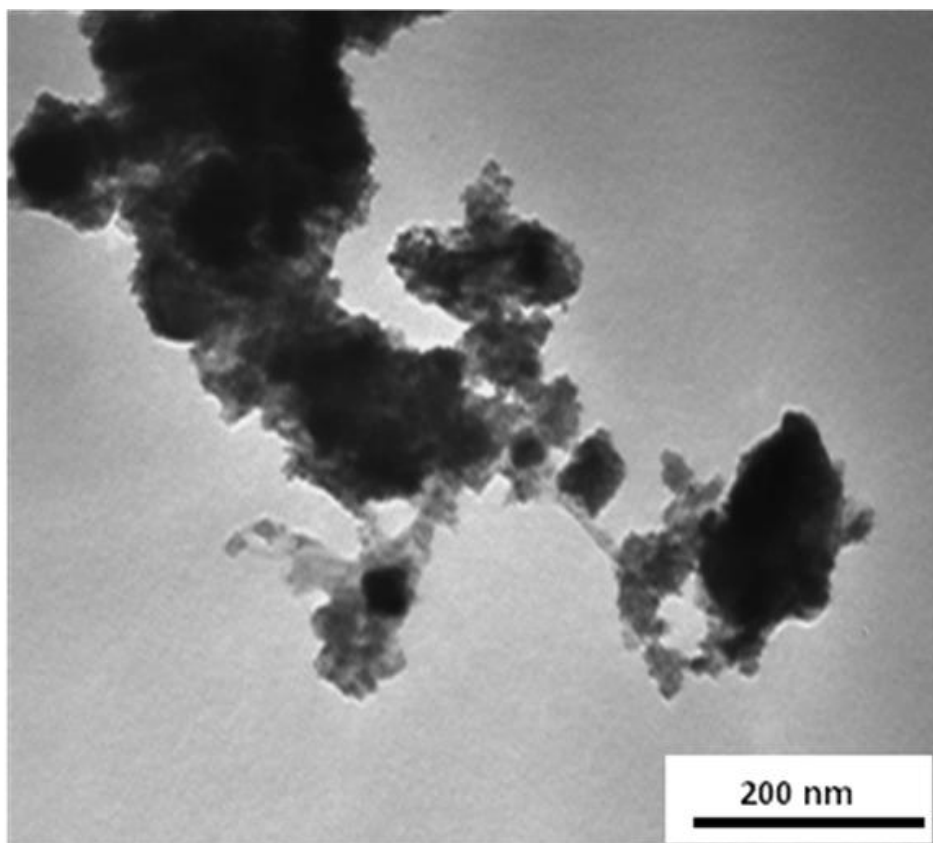

Figure 4.36. TEM micrograph of FeSn$_2$@PAN.

4.3-2. Electrochemistry and mechanism

The specific capacity as a function of cycle number for several electrode materials is shown in Fig. 4.37, where the masses of iron, tin and PAN are taken together into account to give the capacity values.
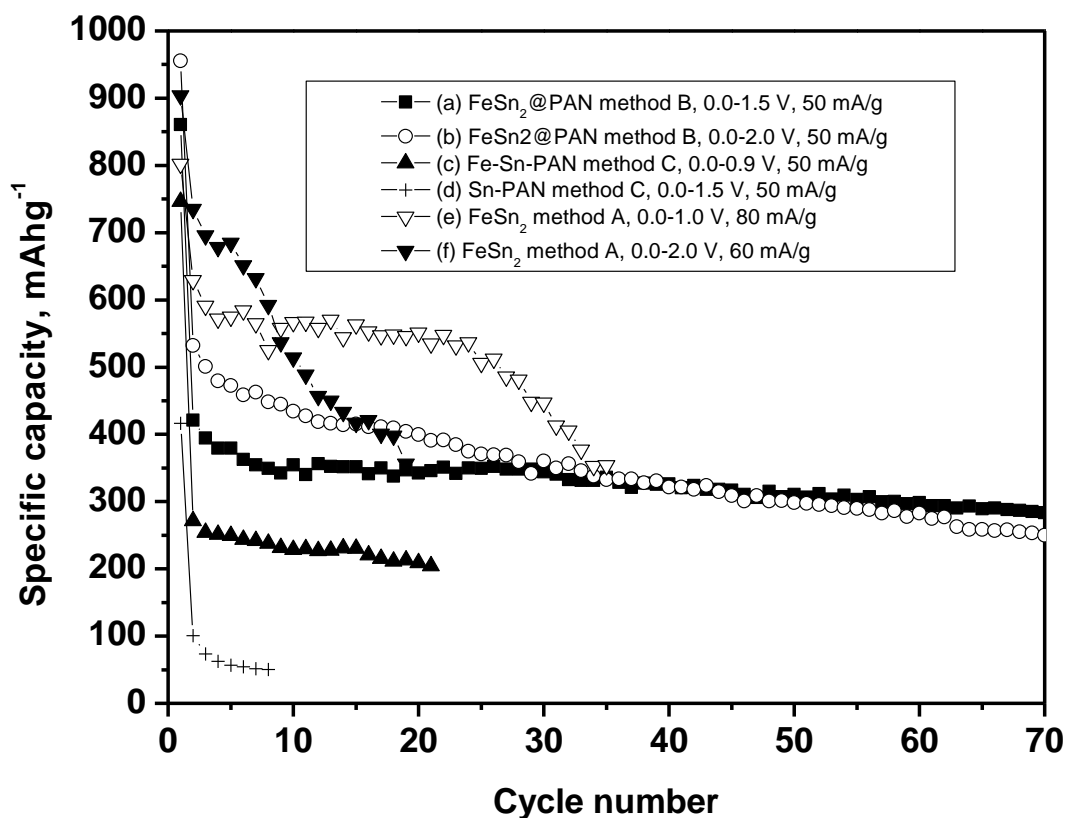
Figure 4.37. Specific capacity as a function of cycle number for FeSn$_2$ and FeSn$_2$@PAN.

The imposed cycling conditions have a marked influence on the resulting behaviour. Previous studies on FeSn$_2$-C showed poor cycling behaviour for an upper potential limit of 0.8 V, and a reasonable cycle life for an upper potential limit of 0.55 V with capacities of ca. 200 mAh/g [3]. Pure and nanometric FeSn$_2$ (method A) shows capacity values in the range between 590 and 530 mAhg^{-1} during ca. 24 cycles, and then the capacity rapidly decreases with 20% of capacity loss from cycle 20 to 30 (Fig.4.37b). Irrespective of the PAN content, the Sn-PAN (transition-metal free) sample exhibits the poorest electrochemical performance. These features are in good agreement with previous results that evidenced the positive effect of the iron atoms [43]. However, it seems that the presence of iron atoms and an initial small particle size are not

sufficient to achieve good cycling behaviour. The diffusion of Li^+ ions through the PAN and the electrochemical inactivity of PAN may contribute to the initial lower reversible capacity of $FeSn_2$@PAN in comparison with PAN-free $FeSn_2$. The sample $FeSn_2$@PAN obtained using method B exhibits a much better cycling stability, with capacity values of ca. 300 mAh/g after 60 cycles (360 mAh/g as referred only to the mass of iron and tin atoms, or 418 mAh/g refereed to the mass of tin). The improved cycling behaviour has to be related with the presence of PAN. Since the capacity drop from cycle number 10 to 60 is equals to 12.8%, more efforts should be still made to optimize this electrode material.

The electrochemistry can be discussed in the light of the derivative curves (Fig. 4.38). The derivative plot corresponding to nanocrystalline $FeSn_2$ obtained by using the method A shows the growth of the peaks at 0.37 V in the discharge and at 0.6 V in the charge from the first to the tenth cycle. These results are indicative of the growth of crystalline Li_xSn grains and particle coalescence that can contribute to the observed capacity fade. Thus, it is expected that the large particles would suffer stronger volume changes and consequently loss of electrical contacts [43]. The resulting derivative after 30 cycles reveals the deterioration of the electrode. On the other hand, it is expected that the Fe particles formed after the first cycle mainly remain electrochemically inactive. Sample $FeSn_2$@PAN (method B of synthesis) shows low-intensity peaks due to formation of Li_xSn, but shows no evidence of an extended grain growth. After 30 cycles, the derivative plot does not show narrow peaks. Thus, the grain growth and the occurrence of large particles of crystalline Li_xSn phases can be discarded.

Two main effects may contribute to the improvement of the electrochemical behavior of $FeSn_2$ in the PAN-containing composite in comparison with PAN-free $FeSn_2$: (i) the small particle size of the metallic grains that do not growth extensively by the effect of the PAN matrix, and (ii) the protection of the particles metallic surface by the PAN against irreversible reaction with liquid electrolyte solution.
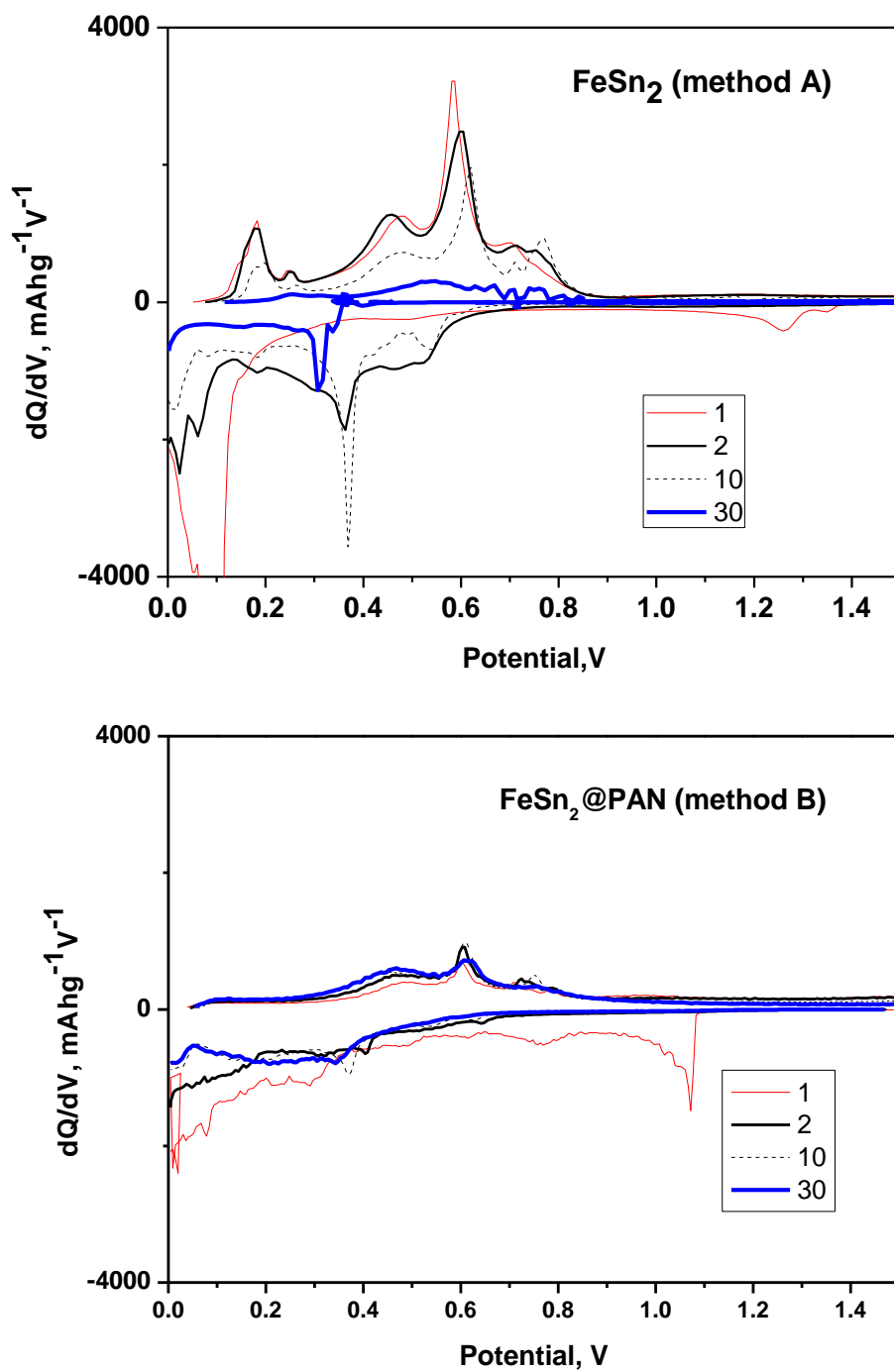
Figure 4.38. Differential capacity vs. potential for FeSn$_2$ and FeSn$_2$@PAN.

The ex-situ XRD pattern obtained after the first discharge of $FeSn_2$@PAN electrodes at 0.0 V shows a broadened and low-intensity peak at ca. 38-39°2θ, which is in good agreement with the occurrence of poorly crystallized Li_xSn phases (Fig. 4.39).
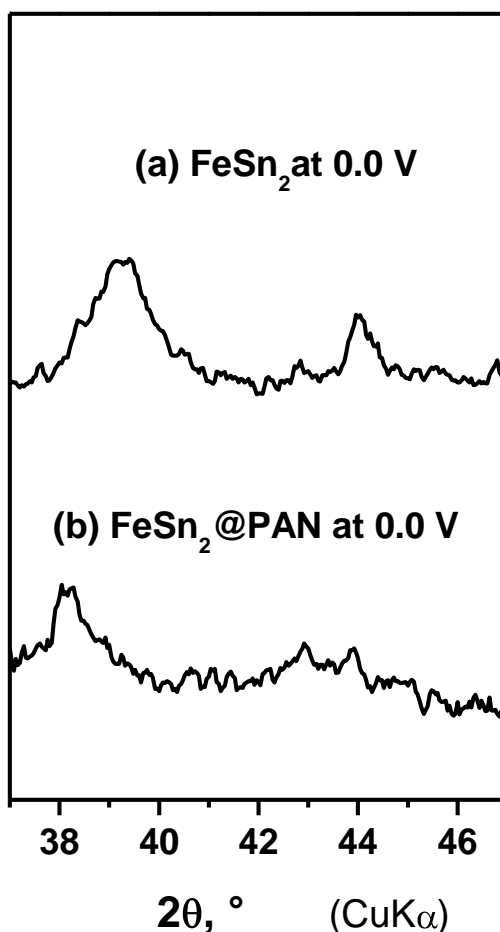

Figure 4.39. XRD patterns for electrodes after the first discharge to 0.0 V vs. Li^+/Li. (a) $FeSn_2$ and (b) $FeSn_2$@PAN

The location of the XRD peak is near the corresponding to $Li_{22}Sn_5$ (XRD file 18-0753) and Li_7Sn_2 (XRD file 29-0837). The exact stoichiometry of the Li_xSn phase has been the subject of certain discussions [3, 43]. For PAN-free $FeSn_2$, the peak at

$44°2\theta$ is ascribed to $FeSn_2$, while both Sn and Li_xSn phases may contribute to the highly broadened peak at $37.7-41°2\theta$. These results are in line with the electrical disconnection of the metallic particles in PAN-free $FeSn_2$, resulting in the occurrence of non-lithiated $FeSn_2$ and Sn grains.

The impedance spectra (Fig.4.40 a, b) are in good agreement with a modification of the interfacial properties and a gain of electrode stability as due to the presence of PAN. The strong degradation of PAN-free $FeSn_2$ is observed in the impedance spectra recorded at several cycle numbers, suggesting certain losses of particle electrical contact. In contrast, the EIS spectra of $FeSn_2@PAN$ show well-defined semicircles due to surface layer (SEI) and charge transfer [44, 45], while the increase of the semicircles sizes from cycle 1 to 10 can be related to the observed initial capacity loss (Fig. 4.37a) [44].

The interface properties of the MSn_2 electrodes are modified by the presence of PAN as is evidenced by the impedance spectra [44, 46]. After the first 18 electrochemical cycles, the impedance spectrum corresponding to $FeSn_2@PAN$ (Fig. 4.40 c, d) shows two well defined depressed semicircles and a Warburg line (W).

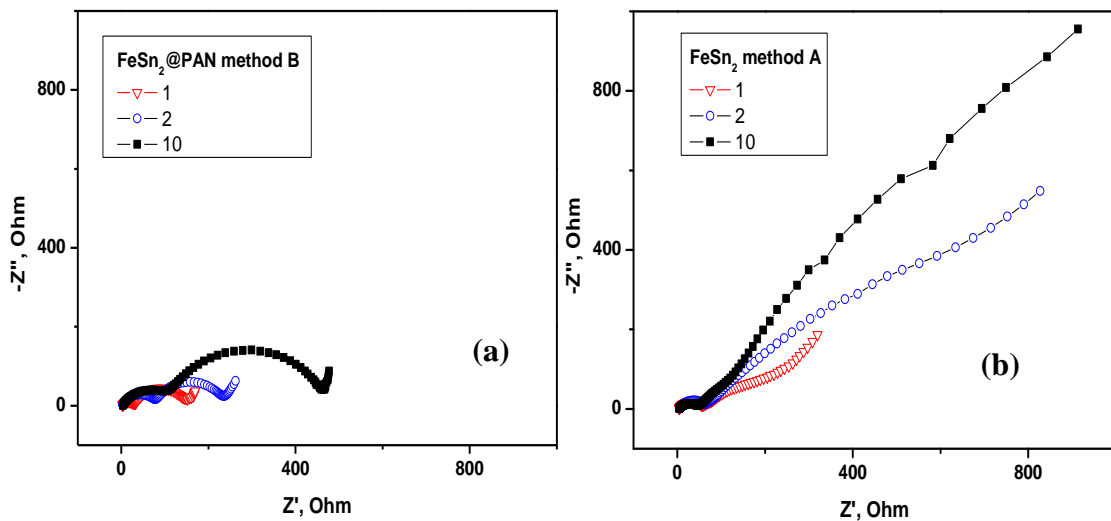**Figure 4.40.** Continued in next page.

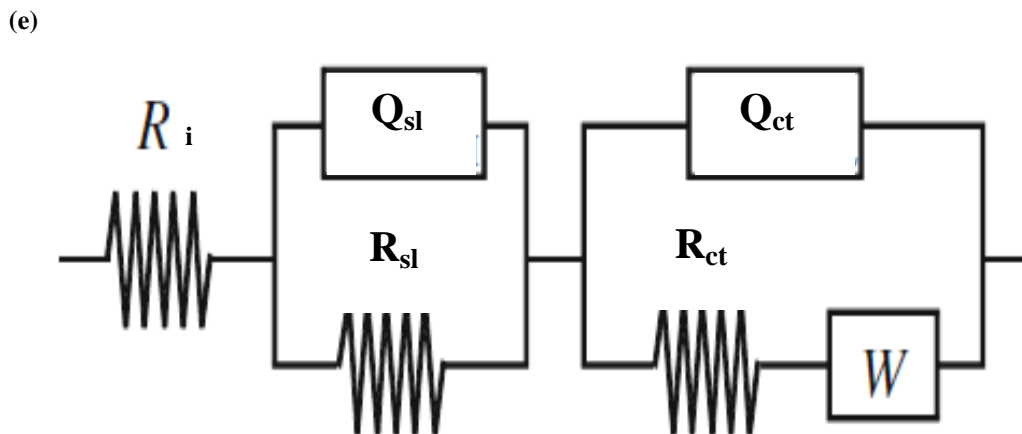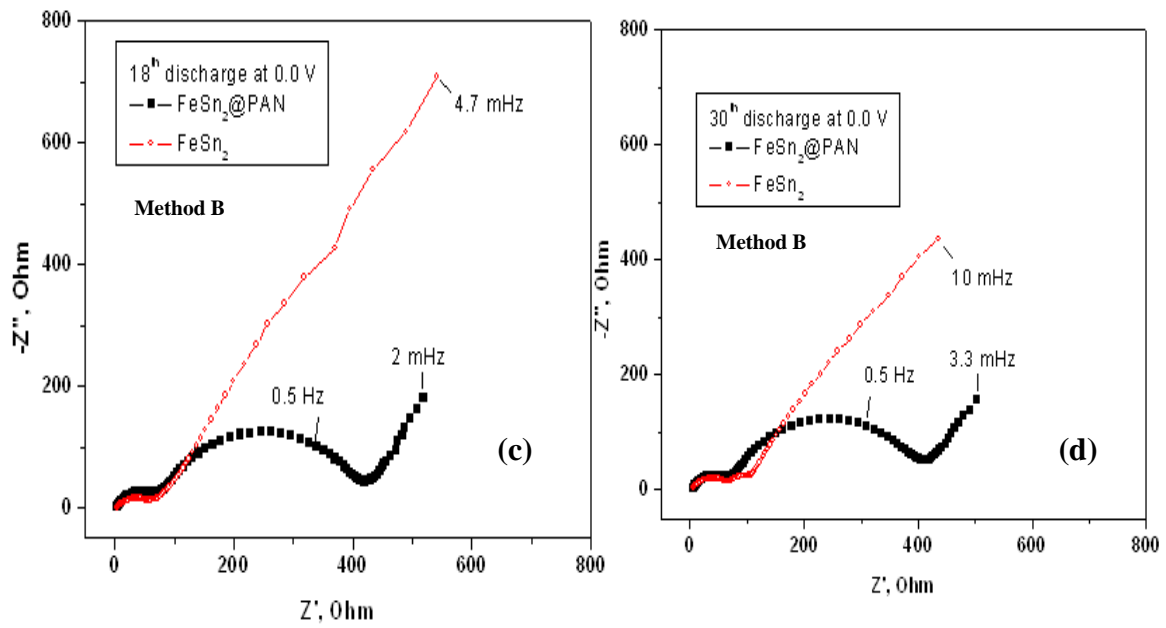**Figure 4.40.** Impedance spectra of electrodes after the 1st, 2nd and 10th discharge to 0.0 V. (a,b), 18th and 30th discharge (c,d), and (e) equivalent circuit used for the fitting of the spectra.

In an equivalent circuit model, the depressed semicircles have contribution from pure resistors (R) and constant phase elements (Q). The semicircle at higher frequencies is usually ascribed to the surface layer or solid electrolyte interface (SEI), while the semicircle at lower frequencies is ascribed to the charge transfer process. The Warburg line is ascribed to lithium diffusion in the electrode material. The impedance spectrum of PAN-free $FeSn_2$ shows a small depressed semicircle at high frequencies (SEI) and a line, suggesting that the electrical contact in many particles is not well formed. From the cycle number 18 to 30, the impedance spectra of $FeSn_2$@PAN remain nearly unmodified, evidencing the stability of the electrode material. Since the sizes of the two semicircles remain nearly constants, it is deduced that the small size of the particles and the organic matrix (PAN) can be used to achieve a stable interface between the metallic particle and the electrolyte (or PAN matrix) and a stable interparticle contact. The simulation and fitting of the impedance spectra of $FeSn_2$@PAN by using an equivalent circuit $R_i(R_{sl}Q_{sl})([R_{ct}W]Q_{ct})]$ (Fig. 4.40e) let to quantify the values of the surface layer resistance (R_{sl}) and charge transfer resistance (R_{ct}). The R_{sl} values are 81.3 and 74.5 Ohm for the cycle number 18 to 30, respectively. The R_{ct} values are 309.9 and 307.9 Ohm for the cycle number 18 and 30, respectively. The pure resistance of the cells, obtained at the highest frequency and reading the value of Z' axis at Z''=0, slightly changes from R_i=3.1 to R_i=3.7 Ohm from the cycle number 18 to 30. The main contribution to this resistance (R_i) would be the lithium ion conductivity in the liquid electrolyte and the PAN. Looking at the impedance values, it results that the presence of PAN is not a problem for the electrode conductivity. After 30 cycles, the impedance spectrum of PAN-free $FeSn_2$ is changed. A small semicircle at intermediate frequencies is emerged that tentatively may be ascribed to charge transfer. The sizes of the semicircles at high frequencies (surface layer) observed after 30 cycles are nearly the same for both $FeSn_2$ and $FeSn_2$@PAN.

A schematic model of the $FeSn_2$@PAN electrode is shown in Fig. 4.41. It is expected that the PAN molecules in the presence of the liquid electrolyte solution of the battery (1 M $LiPF_6$ in ethylene carbonate:diethyl carbonate mixtures) form a Li^+-conductor membrane with high mechanical and dimensional stability [47, 48]. The PAN molecules form a semi-insulating matrix that encapsulates the metallic particles, allow the migration of the Li^+ ions and buffer the volume changes during the electrochemical charge-discharge cycling. The direct contact between the metallic nanoparticles and the

155

liquid electrolyte solution would be prevented by the PAN molecules. The metallic particles may establish direct electrical contacts with the copper foil that acts as current collector. In addition, the very thin layer of PAN that surrounds the metallic nanoparticles can exhibit certain electrical conductivity through an electron hoping mechanism [49, 50]. The small particle size of the amorphous Co-Sn alloy and the organic matrix can contribute to buffer the volume changes and stabilize the electrolyte-metallic particle interface, thus resulting in an excellent cycling behaviour.
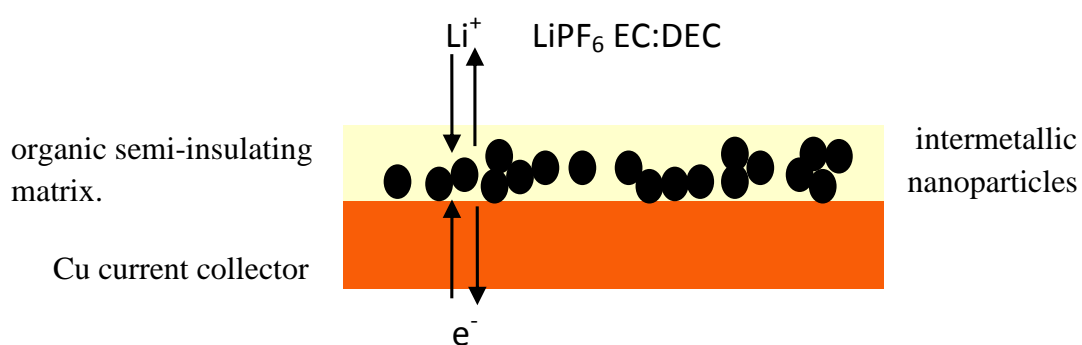

Figure 4.41. Proposed model for the $FeSn_2$@PAN electrode for lithium ion batteries. The hybrid organic-inorganic character of the material and the electron and ionic conductivity are represented.

REFERENCES

1. R. Alcántara, P. Lavela, G. Ortiz, I. Rodríguez, J.L. Tirado, Hyp. Interact., 187 (2003) 13.

2. B. Wodniecka, P. Wodniecki, A. Kulinska, A.Z. Hrynkiewicz, J. Alloys Compd., 321 (2001) 1.

3. O. Mao, R.D. Dunlap, J.R. Dahn, J. Electrochem. Soc., 146 (1999) 405.

4. P.P. Ferguson, P. Liao, R.A. Dunlap, J.R. Dahn, J. Electrochem. Soc., 156 (2009) A13.

5. G. Le Caer, B. Malaman, G. Venturini, D. Fruchart, B. Roques, J. Phys. F: Met. Phys., 15 (1985) 1813.

6. G. Trumpy, E. Both, C. Djega-Mariadassou, Phys. Rev. B, 2 (1970) 3477.

7. E.P. Yelsukov, G.N. Konygin, E.V. Voronina, A.V. Korolyov, A.I. Ulyanov, S.K. Godovikov, A.V. Zagainov, J. Magn. Magn. Mater., 214 (2000) 258.

8. R. Alcántara, U. Nwokeke, I. Rodríguez, J.L. Tirado, Electrochem. Solid-State Lett., 11 (2008) A209.

9. J.S. Thorne, P.P. Ferguson, R.D. Dunlap, J.R. Dahn, J. Alloys Compd., 472 (2009) 390.

10. X.G. Li, A. Chiba, S. Takahashi, K. Ohsaki, J. Magn. Magn. Mater., 173 (1997) 101.

11. U.G. Nwokeke, R. Alcántara, J.L. Tirado, R. Stoyanova, M. Yoncheva, E. Zhecheva, Chem. Mater., 22 (2010) 2268.

12. M. Winter, J.O. Besenhard, Electrochim. Acta, 45 (1999) 31.

13. L.Y. Beaulieu, K.W. Eberman, R.L. Turner, L.J. Krause, J.R. Dahn, Electrochem. Solid-State Lett., 4 (2001) A137.

14. N. Li, C.R. Martin, B. Scrosati, J. Power Sources, 97-98 (2002) 249.

15. J.L. Tirado, Mater. Sci. Eng. R, 40 (2003) 103.

16. A.S. Arico, P. Bruce, B. Scrosati, J.-M. Tarascon, W. van Schalkwijk, Nat. Mater., 4 (2005) 366.

17. R.A. Dunlap, R.A. Small, D.D. McNeil, M.N. Obrovac, J.R. Dahn, J. Alloys Compd., 289 (1999) 135.

18. S. Naille, R. Dedryvere, D. Zitoun, P.E. Lippens, J. Power Sources, 189 (2009) 806.

19. R. Berger, J.-C. Bissey, J. Kliava, J. Phys. Condens. Mater., 12 (2000) 9347.

20. H. Giefers, M. Nicol, J. Alloys Compd., 422 (2006) 132.

21. K. Nagata, A. Ishihara, J. Magn. Magn. Mater., 1571 (1992) 104.

22. M. Respaud, J.M. Broto, H. Rakoto, A.R. Fert, L. Thomas, B. Barbara, M. Verelst, E. Snoeck, P. Lecante, A. Mosset, J. Osuna, T. Ould Ely, C. Amiens, B. Chaudret, Phys. Rev. B, 57 (1998) 2925.

23. E.P. Yelsukov, E.V. Voronina, G.N. Konygin, G.N. Barinov, A.V. Korolyov, S.K. Godovikov, G.A. Dorofeev, A.V. Zagainov, J. Magn. Magn. Mater., 166 (1997) 334.

24. J. Salado, M. Insausti, I. Gil de Muro, L. Lezama, T. Rojo, J. Non-Cryst. Solids, 354 (2008) 5207.

25. O. Mao, R.A. Dunlap, J.R. Dahn, Solid State Ionics, 118 (1999) 99.

26. O. Mao, R.A. Dunlap, J.R. Dahn, J. Electrochem. Soc., 145 (1998)

27. C.M. Ioniqua-Bousquet, P.E. Lippens, L. Aldon, J. Olivier-Fourcade, J-C. Jumas, Chem. Mater., 18 (2006) 6442

28. R. Alcántara, G. Ortiz, I. Rodríguez, J.L. Tirado, J. Power Sources, 146 (1999) 414.

29. N.N. Greenwood, A. Earnshaw. "Chemistry of the Elements", Butterwarth-Heinemann (1998).

30. K.T. Jacob, S. Raj, L. Rannesh, Int. J. Mater. Res., (2007) 776.

31. F. Nacimiento, R. Alcántara, J.L. Tirado, J. Power Sources, 196 (2011) 2893.

32. N.H. Chou, R.E. Schaak, J. Am. Chem. Soc., 129 (2007) 7339.

33. U.G. Nwokeke, F. Nacimiento, J.R. González, R. Alcántara, J.L. Tirado, C. Perez-Vicente, 5th International Meeting on Developments in Materials, Processes and Applications of Emerging Technologies, Alvor (Portugal) June (2011).

34. C.U. Chisholm, E. El-Sharif, S. Kuzmann, Z. Stichleutner, A. Homonnay, Vertes, Mater. Chem. Phys., 120 (2010) 558.

35. R.A. Dunlap, O. Mao, J.R. Dahn, Phys. Rev. B 59 (1999) 3494.

36. J.J. Zhang, Y.Y. Xia, J. Electrochem. Soc., 153 (2006) A1466.

37. U.G. Nwokeke, R. Alcántara, J.L. Tirado, R. Stoyanova, E. Zhecheva, J. Power Sources, 196 (2011) 6768.

38. R. Alcántara, I. Rodríguez, J.L. Tirado, Chem Phys Chem., 9 (2008) 1171.

39. N. Tamura, M. Fujimoto, M. Kamino, S. Fujitani, Electrochim. Acta, 49 (2004) 1949.

40. P. Guilmin, P. Guyot, G. Marchal, Phys. Lett., 109 (1985) 174.

41. U.G. Nwokeke, A.V. Chadwick, R. Alcántara, M. Alfredsson, J.L. Tirado, J. Alloys Compds. 509 (2011) 3074-3079.

42. Title: Recent advances in nanocrystalline intermetallic tin compounds for the negative electrode of lithium-ion batteries. Authour(s): R. Alcántara, U.G. Nwokeke, F. Nacimiento, P. Lavela, J.L. Tirado, Editor(s): N.K Dhar, P.S. Wijewarnasuriya, A.K. Dutta, Conference: Conference on Energy Harvesting and Storage- Materials, Devices and Applications II, Location: Orlando, FL. Date: APR 25-28, 2011. Sponsor(s): SPIE. Source: ENERGY HARVESTING AND STORAGE: MATERIALS, DEVICES, AND APPLICATIONS II. Book Series: Proceedings of SPIE. Volume: 8035. Article Number: 803506. DOI: 10.1117/12.882863. Published: 2011.

43. M. Chamas, P.E. Lippens, J.C. Jumas, K. Boukerma, R. Dedryvere, D. Gombeau, J. Hassoun, S. Panero, B. Scrosati, J. Power Sources, 196 (2011) 7011.

44. F. Nacimiento, R. Alcántara and J.L. Tirado, J. Electrochem. Soc., 157, A666 (2010).

45. M. Chamas, P.E. Lippens, J.C. Jumas, J. Hassoun, S. Panero, B. Scrosati, Electrochim. Acta, 56 (2011) 6732.

46. U.G. Nwokeke, F. Nacimiento, R. Alcántara, J.L. Tirado, Electrochem. Solid-State Lett., 14 (2011) A148.

47. Y. Huai, J. Gao, Z. Deng, J. Suo, Ionics, 16 (2010) 603-611.

48. K.S. Perera, M.A.K.L. Dissanayake, S. Skaarup, K. West, J. Solid State Electrochem., 12 (2008) 873.

49. G. Lecayon, Y. Bouizem, C. Le Gressus, C. Reynaud, C. Boiziau, C. Juret, Chem. Phys. Lett., 91 (1982) 506.

50. U.G. Nwokeke, F. Nacimiento, J.R. González, R. Alcántara, J.L. Tirado, C. Perez-Vicente, JNanoR., 17 (2012) 53.

5. CONCLUSION

FeSn$_2$

- The "one-pot" method based on the polyol-solvent synthesis is suitable to produce pure nanocrystalline FeSn$_2$ at temperatures below 200°C.

- The nanoparticles of FeSn$_2$ are more reactive than the microparticles.

- The magnetic ordering in FeSn$_2$ is affected by particle size, according to Mössbauer and EPR results.

- The electrochemical behaviour of nano-FeSn$_2$ obtained by the polyol method is much better than that of the microparticles obtained at 490°C.

- EPR and Mössbauer data confirm the presence of superparamagnetic iron (and/or tin-doped iron) nanoparticles which are generated during discharge of the electrode. The composition and the dimensions of the superparamagnetic particles are sensitive whether the electrodes are fully or partially discharged and are preserved even after the reverse charge process. These particles avoid particle aggregation and thus improve the electrochemical performance.

- The reaction mechanism involves the formation of Li$_x$Sn intermetallics and metallic Fe for microparticles while superparamagnetic nanoparticles of Fe are formed for nano-FeSn$_2$.

FeSn$_2$-CoSn$_2$ solid solutions

- Solid solutions Fe$_{1-x}$Co$_x$Sn$_2$ of have been prepared for the first time.

- For pure CoSn$_x$, the tendency to preserve the Co-Sn interactions inhibits the formation of crystalline Li$_x$Sn products, thus preventing the tin particle aggregation and favouring cycling stability.

- Nanocrystalline Fe$_{1-x}$Co$_x$Sn$_2$ active materials deliver reversible capacities above 500 mAhg^{-1} during 30 cycles that depend on the composition and cycling conditions. The intermediate solid solution Fe$_{0.5}$Co$_{0.5}$Sn$_2$ exhibits better electrochemical performance than the limit CoSn$_2$ and FeSn$_2$.

Intermetallics/Polyacrylonitrile (PAN) composite.

- The combination of the polyol and sonochemical methods helps to prepare PAN-encapsulated tin-intermetallics electrode materials.

- PAN molecules contribute to the stabilization of the metallic nanoparticles, suppress the aggregation of the metallic particles, protect the particles surface and accommodate the volume changes during the electrochemical cycling.

6. PUBLICATIONS